APPLICATIONS OF ELECTROSPUN NANOFIBERS IN FILTRATION PROCESSES

A Thesis Submitted to
the Graduate School of Engineering and Sciences of
İzmir Institute of Technology
In Partial Fulfillment of the Requirements for the Degree of

DOCTOR OF PHILOSOPHY

in Chemistry

by
Nesrin HORZUM POLAT

September 2013
İZMİR

We approve the thesis of **Nesrin HORZUM POLAT**

Examining Committee Members:

_____
Prof. Dr. Latif ELÇİ
Department of Chemistry, Pamukkale University

_____
Prof. Dr. Ayşe Merih SARIIŞIK
Department of Textile Sciences, Dokuz Eylül University

_____
Assoc. Prof. Mustafa M. DEMİR
Department of Chemistry, İzmir Institute of Technology

_____
Assist. Prof. Hadi M. ZAREİE
Department of Materials Science and Engineering,
İzmir Institute of Technology

_____
Assist. Prof. Mustafa EMRULLAHOĞLU
Department of Chemistry, İzmir Institute of Technology

12 September 2013

_____
Assoc. Prof. Mustafa M. DEMİR
Supervisor, Department of Chemistry
İzmir Institute of Technology

_____   _____
Prof. Dr. Ahmet E. EROĞLU   **Prof. Dr. R. Tuğrul SENGER**
Head of the Department of Chemistry   Dean of the Graduate School of
                                         Engineering and Sciences

ACKNOWLEDGEMENTS

ABSTRACT

APPLICATIONS OF ELECTROSPUN NANOFIBERS IN FILTRATION PROCESSES

Electrospinning is a simple and versatile method to fabricate ultrathin fibrous mats from a wide variety of organic and/or inorganic materials. Since it allows fabricating fiber diameter and surface/internal structures by solution and instrumental parameters, electrospun fibers provide much enhanced functionalities, which can not be obtained by bulk materials. This thesis examines the filtration, sensing and catalytical applications associated with the remarkable features of electrospun nanofibers. The systems studied are reported herein;

(i) The first part of this dissertation deals with the filtration applications of electrospun nanofibrous membranes.

- *Nano-sized chitosan fibers* were utilized for sorption of Fe(III), Cu(II), Ag(I), and Cd(II) ions from aqueous solutions.

- The surface of chitosan fibers were further functionalized by monodisperse *nano zero-valent iron (nZVI) particles* for the removal of inorganic arsenic species.

- Sorption of radioactive U(VI) ions from aqueous systems via column sorption under continuous flow was performed using *amidoximated polyacrylonitrile fibers.*

(ii) The second part of this dissertation presents sensing applications of ceramic fibers.

- Humidity sensing properties of electrospun *ZnO fiber* mats were investigated by quartz crystal microbalance (QCM) method and electrical measurements.

- Electrospinning technique was used as coating process for deposition of *CeO$_2$/ZnO and ZnO based nanofibers* on the electrode of QCM. The fiber-coated QCM sensors were used for the detection of volatile organic compounds (VOCs).

(iii) The last part of this dissertation describes an approach to fabricate *hierarchically structured composite nanofibers*. The nanostructured materials prepared by the simultaneous electrospinning of CeO$_2$ and LiCoO$_2$ precursors and SiO$_2$ nanoparticles were used for the photocatalytic degradation of Rhodamine B.

ÖZET

ELEKTROEĞİRME NANOLİFLERİN FİLTRASYON İŞLEMLERİNDE UYGULAMALARI

Elektroeğirme, geniş bir yelpazede organik ve/veya inorganik malzemelerden ultra ince lifsi yapılar üretmek için basit ve çok yönlü bir yöntemdir. Çözelti ve enstrümental parametreler ayarlanılarak lif çapı ve yüzey/iç yapıları kontrol edilebildiğinden dolayı, elektroeğirme nanolifler, kütlesel büyüklükteki aynı malzemelerle elde edilemeyen gelişmiş özellikler sergilerler. Bu tez, elektroeğirme nanoliflerin olağanüstü özellkleriyle ilişkili filtrasyon, algılama ve katalitik uygulamalarını incelemektedir. Çalışılan sistemler burada rapor edilmiştir;

(i) Bu tezin ilk kısmı, elektroeğirme nanolifsi membranların filtrasyon uygulamaları ile ilgilidir.

- Nanometre boyutunda *kitosan lifler*, Fe(III), Cu(II), Ag(I) ve Cd(II) iyonlarının sulu çözeltilerden sorpsiyonu için kullanılmıştır.

- Kitosan liflerin yüzeyi homojen dağılımlı *sıfır değerlikli demir nanotanecikler* ile işlevselleştirilerek inorganik arsenik türlerinin uzaklaştırılmasında kullanılmıştır.

- Sürekli akış altında radyoaktif uranil iyonlarının kolon sorpsiyonu, amidoksimlenmiş *poliakrilonitril lifler* kullanılarak gerçekleştirilmiştir.

(ii) Bu tezin ikinci kısmı, seramik liflerin algılama uygulamalarını sunmaktadır.

- Elektroeğrilmiş *ZnO liflerin* nem sensörü özellikleri, kuartz kristal mikrobalans (KKM) metodu kullanılarak ve elektriksel ölçümler yapılarak araştırılmıştır

- Elektroeğirme tekniği *CeO₂/ZnO ve ZnO bazlı nanoliflerin* KKM elektrodu yüzeyine depolanması için kaplama işlemi olarak kullanılmıştır. Lif-kaplı KKM sensörü uçucu organik bileşiklerin (UOB) algılanmasında kullanılmıştır.

(iii) Bu tezin son kısmı katalitik uygulamalar için *hiyerarşik yapılı kompozit nanoliflerin* üretimi için bir yaklaşım anlatmaktadır. CeO_2, $LiCoO_2$ öncülleri ile SiO_2 nanotaneciklerinin birlikte elektroeğrilmesi ile hazırlanan bu nanoyapılı malzemeler, Rodamin B'nin fotokatalitik bozunmasında kullanılmıştır.

Dedicated to my parents…

TABLE OF CONTENTS

LIST OF FIGURES

LIST OF TABLES

LIST OF ABBREVIATIONS

AFD	average fiber diameter
ATR	attenuated total reflection
BET	Brunauer-Emmett-Teller
BPO	benzoyl peroxide
DD	degree of deacetylation
DMF	N,N-dimethylformamide
EDX	energy dispersive X-ray
EPA	environmental protection agency
FTIR	fourier transform infrared spectrometer/spectrometry
HFIP	1,1,1,3,3,3-hexafluoroisopropanol
HSAB	hard-soft acid base principle
HVAC	heating, ventilating and air conditioning
IC	ion chromatography
ICP-MS	inductively coupled plasma-mass spectrometer/spectrometry
MCL	maximum contamination levels
NF	nanofiltration
NMR	nuclear magnetic resonance
nZVI	nano zero-valent iron
NNI	national nanotechnology initiative
PAA	polyacrylic acid
PAMAM	poly(amidoamine)
PAN	polyacrylonitrile
PEI	polyethyleneimine
PEO	poly(ethyleneoxide)
PL	photoluminescence
PPX	poly(p-xylene)
PVA	polyvinyl alcohol
QCM	quartz crystal microbalance
RH	relative humidity
SAW	surface acoustic wave
SEM	scanning electron microscope/microscopy

SMO	semiconductor metal oxide
SPE	solid phase extraction
STEM	scanning transmission electron microscope/microscopy
TFA	trifluoroacetic acid
TNT	trinitrotoluene
TGA	thermogravimetric analysis
TUFT	tubes by fiber templates
VLS	vapor−liquid−solid
VOCs	volatile organic compounds
VS	vapor−solid
WHO	world health organization
XANES	X-ray absorption near-edge spectroscopy
XAS	X-ray absorption spectroscopy
XPS	X-ray photoelectron spectroscopy
XRD	X-ray diffraction

CHAPTER 1

INTRODUCTION

Nanoscience and nanotechnology represents the application of extremely small devices in what is science, engineering, and technology performed on a nanoscale - considered to be a scale between 1 and 100 nanometers. Nanotechnology may be performed in all areas of science including chemistry, biology, physics, materials science, and engineering in what is not just a new field of science, but a new way of looking and studying.

A famous speech entitled "*There's Plenty of Room at the Bottom*" by physicist Richard Feynman introduced the ideas and concepts behind nanoscience and nanotechnology at an American Physical Society meeting at the California Institute of Technology on December 29, 1959 (Feynmann 1959). In his talk, Feynman described a process in which scientists would be in a position to manipulate and control individual atoms and molecules. Some 15 years after this groundbreaking speech, Professor Norio Taniguchi used the term nanotechnology in his explorations of ultraprecision machining (Taniguchi 1974). When K. Eric Drexler popularized the word 'nanotechnology' in the 1980's, he was referring specifically to constructing microscoping machines on a molecular scale; motors, robot arms, and even whole computers just a few nanometers wide, far smaller even than a cell (Drexler 1986). The science of nanotechnology in its modern form gained prominence in 1981, spurred on by the emergence of the scanning tunneling microscope that could observe individual atoms. As the concept of nanotechnology gained wider acceptance, the meaning of the word shifted to encompass the simpler kinds of nanometerscale technology. The U.S. National Nanotechnology Initiative (NNI) was established in 2001 to fund such nanotechnology: their definition includes anything smaller than 100 nanometers with novel properties.

1.1. Motivation

Long before people started to make nanomaterials, they were found in the natural environment. Nanomaterials have a wide array of natural sources which can be

found throughout the natural environment. The nanosphere is host to a number of enzymes and viruses. While it may be considered improper to copy the ideas of others, scientists find that they can use the work of Mother Nature as a template. The natural presence of nanomaterials provides an inspiring way of bridging nanoscience into the classroom. Discovering that common natural materials which we use in our everyday lives such as paper and clay, or materials such as feathers and spider silk or materials, have properties that depend not only on their chemistry but also on their nanostructure is especially inspiring.

The process of electrospinning, which was inspired by nature, was established to mechanically produce nanofibers from different functional materials. The electrospinning technology is being applied by the Donaldson Company, Inc. and the Freudenberg Nonwovens Group to manufacture high-quality filtering media. One subject of research is the advancement of this technology to produce more novel functional nanofibers (Greiner and Wendorff 2007, Li and Xia 2004, Reneker and Chun 1996). However, it is not just from the point of view of life sciences that the study of fiber fabrication is of interest – it is also from of interest from the point of view of industrial applications as well. A number of unique features and properties may be found in electrospun nanofibers including 1D morphology, extraordinary length, high surface area and a hierarchically porous structure (Li and Xia 2004). One further important feature is that they can be easily prepared as membranes (supported or free-standing, and nonwoven or woven) and which can be conveniently handled and manipulated during an application. Nanofiber mats are especially well suited for many membrane-based applications, including filtration and separation, sensors, and as substrates/supports for catalysts.

The controlling the surface chemistry of nanofibers, has become an active research field in the last two decades, because of the increasing interest in fabricating materials with the superior properties, crucial in many applications (Agarwal et al. 2010, Venugopal and Ramakrishna 2005, Wang, Wan, et al. 2009). The functionality of the nanofibrous scaffold can be controlled through suitable surface modification schemes for different applications (Gibson et al. 2001). Chu et al. demonstrated that electrospun nanofibrous scaffolds can be used as a highly efficient microfiltration media to remove bacteria, viruses, dyes (Ma, Burger, et al. 2012, Wang, Liu, et al. 2012). The removal of heavy metal ions from wastewater using electrospun nanofiber membranes is primarily based on the interactions between the functional sites on the nanofiber

surface and the heavy metal ions. The interactions involved can be physical (e.g. affinity or electrostatic interactions) or chemical (e.g. chelating or coordination complex formation) (Rivas and Maureira 2008). Therefore, the nature of functionality on the nanofiber surface is the primary factor that determines the capability of toxic metal removal. On the other hand, the nanofibrous scaffold itself is an effective microfiltration medium. This dual functionality (efficient microfiltration capability with excellent surface functionality) forms the essence in achieving a good design for separation membranes that can effectively remove toxic metals in contaminated water sources as well as performing the typical microfiltration role (Ma et al. 2013).

Although many polymeric materials have been electrospun into nanofibers, the capability of electrospinning has been successfully extended to fabricate more than 100 different types of ceramic nanofibers through a combination of the sol-gel method (Dai et al. 2011). Additionally, the excellent semiconducting property of some materials (eg. ZnO, CeO$_2$, etc.) render them good candidates as sensors for undesirable volatile organic compounds. Tremendous progress has been achieved in the development of ultrasensitive sensors in response to the imperative needs for more timely and reliable detections in environmental monitoring, food inspection and medical diagnostics (Ding et al. 2010, Huang et al. 2003, Wang et al. 2002). As well as the relatively large specific surface area and high porosity of electrospun ceramic nanomaterials, deposition of homogeneous nanostructured coating on the surface of the substrate such as electrode, QCM, etc. can be obtained through electrospinning to improve the sensor sensitivity.

When it comes removing organic molecules in an aqueous solution and in air flow, Electrospun ceramic nanofibers also provide an attractive class of solid support for catalysts (Zhan et al. 2007, Kanjwal et al. 2010, Kanjwal et al. 2011). The supporting material has been proven to have a significant impact on the performance of a heterogeneous catalyst, in a mechanism known as synergistic effect. A sound support should be a stable, a good electron-conductor and offer a significant surface area. Nevertheless, it should be emhasised that the as-spun inorganic/polymer mats are very flexible and easy to remove and handle over large areas, while the porous ceramic mats are fragile and tend to break into small pieces. Such a lack of mechanical strength undoubtedly restricts their board applications. Therefore, new ceramic nanofibers are still in great demand in overcoming this issue and in electrospinning. A new concept for the preparation of nanofibrous metal oxides based on the simultaneous electrospinning of metal oxide precursors and silica nanoparticles was presented by Horzum et al.

(Horzum et al. 2012). In the study, the obtained continuous silica fibers were found to act as a structural framework for metal oxide nanoparticles and exhibited improved mechanical integrity compared to the neat metal oxide fibers.

1.2.   Structure and Scope of the Thesis

Each chapter of this thesis, with the logical exception of the general introduction (*Chapter 1*) and the conclusive chapter (*Chapter 8)*, is organized in the same manner: a theoretical section, which reviews important theoretical concepts and the fundamentals of the experimental methods, followed by the experimental details; and a discussion of the results and the main conclusions are provided at the end of the chapter.

The first part of the work (*Chapter 2*) deals with the fabrication and characterization of the chitosan nanofibrous scaffold used as a sorbent for the removal of undesirable metal ions through sorption from contaminated water. While these membranes are already considered as superior microfiltration media, given their higher permeation flux and lower pressure drop performance than conventional microfiltration membranes, they also have a high surface area-to-volume ratio. The sorption efficiency of chitosan nanofiber was compared to that of powder and checked with a mixture of Cu (II), Fe (III), Ag (I) and Cd (II) ions by both batch and column methods. The Electrospun nanofibers also provide a surface which can be further modified to remove toxic metal ions with enhanced capability. In *Chapter 3*, chitosan fibers were decorated with nanoscale zero-valent iron (nZVI) particles for sequestration of inorganic arsenic species. The obtained chitosan fibers-supported nZVI particles overcome disadvantages such as agglomeration of the magnetic nZVI nanoparticles, and pH limitation of chitosan, particularly in acidic environment by combining the integrated high surface area of both nanoparticles and electrospun fibers,. After characterization of the chitosan-nZVI samples before and after the removal of As(III) and As(V), the estimation of the sorption mechanisms is discussed. nZVI particles were deposited on electrospun mat by mixing the metal precursor with the fiber, then followed by reducing metal cations in a reducing media. In *Chapter 4*, the nitrile groups on the polyacrylonitrile (PAN) fibers' surface were modified to amidoxime groups by solution process. The sorption efficiency of amidoxime-modified fiber were determined for the removal of radioactive

and chemically toxic U(VI) ions from aqueous systems via column sorption under continuous flow.

Studies were performed of the fabrication of electrospun metal oxide fibers and their sensing applications. ZnO nanofibers were applied as a humidity sensor. (*Chapter 5*) Next, ZnO and CeO_2/ZnO nanofibers were exampled in an effort to sense volatile organic compounds (VOCs). (*Chapter* 6). The determination of the sensing ability of the nanofibers was determined with the help of QCM technique. The synthetic pathway for the coating of the QCM electrode and formulations used are represented.

A new concept for the preparation of nanofibrous metal oxides based on the simultaneous electrospinning of metal precursors and silica nanoparticles is set out in *Chapter 7*. Metal oxide/silica nanofibers hierarchically structured by colloid electrospinning were exemplified for the cases of CeO_2 and $LiCoO_2$ as models and the catalytic activity of the composite nanofibers were also described.

The main theme of this study is to extend the work to the filtration applications of electrospun nanofibrous mats with different chemical nature and investigate the influence of their structure on the morphology and sorption efficiency of the resulting materials.

1.3.   State of the Art: Electrospinning

The process of electrostatic fiber spinning, or "electrospinning," involves electrostatic forces in the ejection a charged fluid jet from a nozzle to construct a fiber. On the whole, the fiber is laid down on a collector to form a nonwoven mat, an example of which is shown in Figure 1.1. In an example from the rapidly growing domain of electrospinning, tissues can be made of fibers that are too thin to be observed under the most senstive optical microscope, polymer webs can be placed on plants which are more intricate than spider's webs, and filters can be covered by a "whiff of nothing" (as it was once referred to by J. C. Binzer) that increases their effectiveness immensely, or wound dressings can be made of gossamer fibers carrying a medical agent, enabling faster healing.
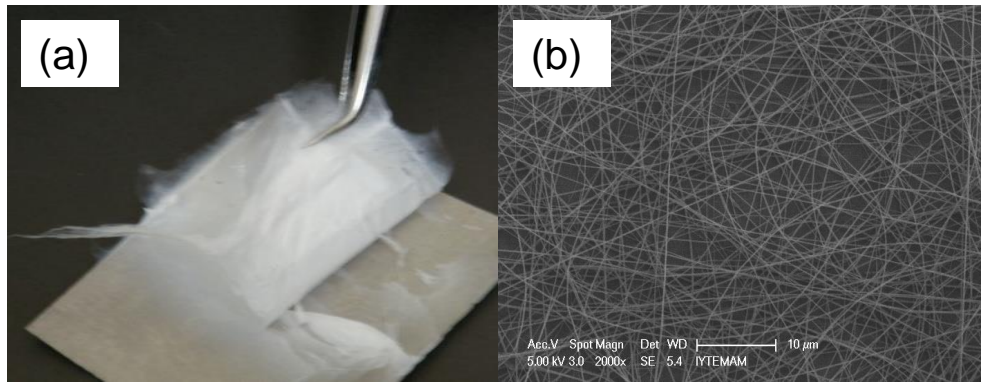
Figure 1.1. (a) Photographic image of electrospun chitosan nonwoven mat, (b) SEM
micrograph of the chitosan nanofibers

The technology of electrospinning has its basis in early studies. The first record of the electrostatic attraction of a liquid was observed in 1600 by William Gilbert (Tucker et al. 2012). In 1745, Bose described aeresols generated by the application of high electric potentials to drops of fluids (Bose 1745). Christian Friedrich Schönbein produced highly nitrated cellulose in 1846. In 1882, Lord Rayleigh investigated the question of how many charges are needed to overcome the surface tension of a drop (Rayleigh 1882). In 1887 Charles Vernon Boys described the process in a paper on nano-fiber manufacture. John Francis Cooley filed the first electrospinning patent in 1900. Later, the first devices to spray liquids through the application of an electrical charge were patented by Cooley and Morton, in 1902 and 1903 (Cooley 1902, 1903, Morton 1902). In 1914, Zeleny presented one of the earliest studies of the electrified jetting phenomenon (Zeleny 1917). In 1929, Hagiwaba et al. described the fabrication of artificial silk through the use of electrical charge (Hagiwaba et al. 1929).

The crucial patent, in which the electrospinning of plastics was described for the first time, appeared in 1934 with Anton Formhals from Mainz as the author (and can be traced back to a German patent filing in 1929) (Formhals 1934). Despite these early discoveries, the procedure was not utilized commercially. In 1938, N.D. Rozenblum and I.V. Petryanov-Sokolov generated electrospun fibers, which they developed into filter materials. Between 1964 and 1969 Sir Geoffrey Ingram Taylor produced the beginnings of a theoretical underpinning of electrospinning by mathematically modelling the shape of the (Taylor) cone formed by the fluid droplet under the effect of an electric field (Taylor 1969, Taylor 1966). However, the practice of electrospinning technology remained largely dormant until the 1970s. Simm et al. patented the production of fibers with diameters of less than 1 mm in the 1970s (Simm et al. 1972). However, this work, which was followed by other patents, also remained unnoticed. Similarly, in

electrospinning research, only a few publications appeared in the 1970s and 1980s, notably by Baumgartner (Baumgarten 1971) and by Larrondo and St. John Manley (Larrondo and Manley 1981). In Baumgartner's experiment, a glass capillary was filled with an acrylic polymer solution. A charged wire was inserted into the capillary. There was no flow rate control; once a critical voltage was applied, a fluid jet ejected out from the capillary tip. The effect of humidity on the electrospinning process was studied. High humidity caused the fluid jet to dry improperly. Larrondo and Manley demonstrated the feasibility of electrospinning polymer melt instead of a solution. A melt extruder was used to deliver a polyethylene to a charged capillary. The electrospun fibers were about 10 microns in diameter.

In the 1990s, a great interest in electrospinning research was generated when Reneker and co-workers reintroduced this technique as a facile way to make submicron fibers (Srinivasan and Reneker 1995, Reneker and Chun 1996, Fang and Reneker 1997, Doshi and Reneker 1995, Kim and Reneker 1999). Since then, it has been shown that almost any material that can be spun from melt or solution by conventional methods can likely be electrospun into fibers.

Researchers also experimented with novel electrospinning devices. A miniaturized version of the electrospinning device was made using microfabrication technique (Kameoka et al. 2003). The micro-elecrospinning device acts like a scanning tip, depositing the fiber in a well-aligned way. In another device, a series of large capillaries is placed in line to electrospinning multiple fibers at the same time to increase productivity (Fang et al. 2006). Additionally, some electrospinning devices do not have the capillary tube at all; they are nozzle-less. Charges are injected directly into the fluid using needle-shaped electrodes (Yarin and Zussman 2004a). A commercial electrospinning is available for scale-up production as well (NanoSpider^{TM} developed by Elmarco).

1.3.1. Description of the General Equipment

Electrospinning is a simple and easily controlled process in the production of fibers with dimensions down to a nanometer scale. First of all, polymers will be surveyed as fiber forming materials. Later, materials such as metals, ceramics, and glasses will be considered as fiber precursors. In a typical electrospinning experiment in

a laboratory, a polymer solution or melt is pumped through a thin nozzle with an inner diameter on the order of 100 mm (Figure 1.2). The nozzle simultaneously serves as an electrode, to which a high electric field of 100–500 kV m^{-1} is applied, and the distance to the counter electrode is 10–25 cm in laboratory systems. The currents that flow during electrospinning range from a few hundred nanoamperes to microamperes. The substrate on which the electrospun fibers are collected is typically brought into contact with the counter electrode. Electrospinning can be carried out both "from bottom to top" or horizontally and "from top to bottom" or vertically.

Figure 1.2. The electrospinning set up in our laboratory

The voltage that is then applied leads to a cone-shaped deformation of the drop of polymer solution, in the direction of the counter electrode (Figure 1.3). In electrospinning, the cone angle is about 30°. If higher voltages are applied, a jet is formed from the deformed drop, which moves towards the counter electrode and becomes narrower in the process (Yarin et al. 2001, Cloupeau and Prunetfoch 1989). On the way to the counter electrode, the solvent evaporates (or the melt solidifies), and solid fibers with diameters ranging from micrometers to nanometers.

It becomes clear, on closer inspection, that the electrospinning process is in fact highly complex. For instance, the jet only follows a direct path towards the counter electrode for a certain distance, before significantly changing its appearance. The jet is moved laterally and forms a series of coils, the envelope of which has the form of a cone opening towards the counter electrode (Figure 1.4) (Yarin et al. 2001, Reneker et al. 2000).

Figure 1.3. A droplet of aqueous poly(ethylene oxide) (PEO) solution dyed with fluorescein at the needle tip: A) in the absence of electric field, B) in the presence of electrical field, with a jet perpendicular to the counter electrode, C) with a jet diagonal to the counter electrode (Source: Greiner and Wendorff 2007)
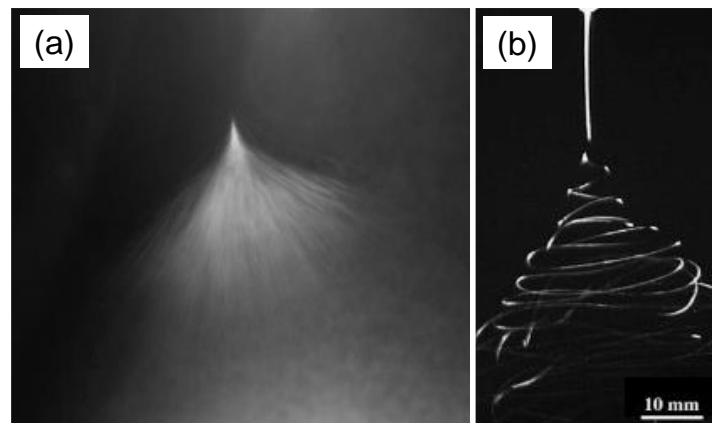
Figure 1.4. (a) Photographic image of a jet of PEO solution under electrical field, (b) High-speed photograph showing the jet instabilities (Source: Yarin et al. 2001)

Beads, rather than fibers, may occasionally be formed during electrospinning; fibers with beads arranged in a manner akin to pearls on a string can also be formed. In some cases, the fibers are not round, but take the form of flat ribbons, while in other cases, the distribution of fiber diameters is broad (Figure 1.5). The shapes and dimensions of the fibers formed depend on a large set of parameters, for example, the properties of the polymer itself (such as molecular weight, molecular-weight distribution, glass-transition temperature, and solubility), as well the properties of the polymer solution (such as viscosity, viscoelasticity, concentration, surface tension, and electrical conductivity).
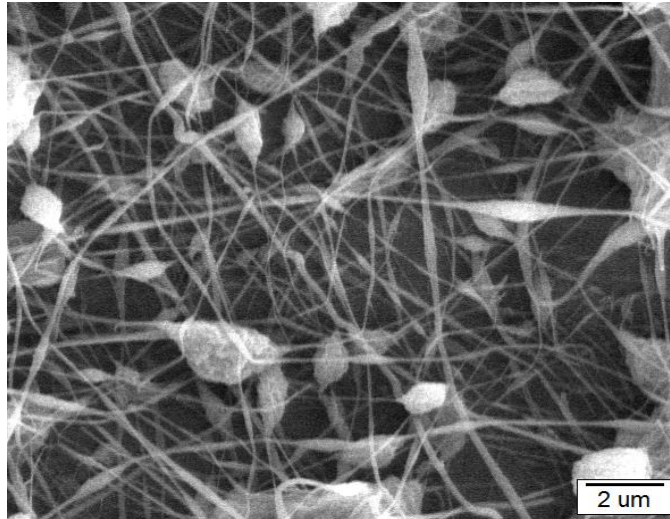
Figure 1.5. SEM micrograph of the irregularly shaped electrospun poly(methyl methacrylate) (PMMA) fibers from DMF solution

The vapor pressure of the solvent and the relative humidity of the surroundings can also have a significant impact. Furthermore, the properties of the substrate, the feed rate of the solution, and the field strength and geometry of the electrodes (and therefore, the form of the electric field) play a major role in fiber formation.

1.3.2. The Fundamental Aspect

The process of electrospinning can be characterized by three major regions: the cone region, the steady jet region, and the instability region. In the initial stage of electrospinning, a pendent drop of a fluid is charged at the tip of the nozzle. Charges then repel each other on the surface of the pendent drop, working against the surface tension and deforming the droplet into a conical shape, just before jetting occurs. The conical shape is referred to as the Taylor Cone, named after G. I. Taylor who studied this electrified fluid phenomenon (Taylor 1969, Taylor 1966). A fluid jet is then ejected from the apex of the cone at a critical electrical stress, with the jet having a diameter of about 100 micrometers at the apex. In the steady jet region (shown red in Figure 1.6), the jet can travel in a straight path for a distance of between 1 and 20 centimeters. For a fluid that is a solution, real-time spectroscopic data shows that there is only negligible loss of solvent due to evaporation in this portion of the jet.
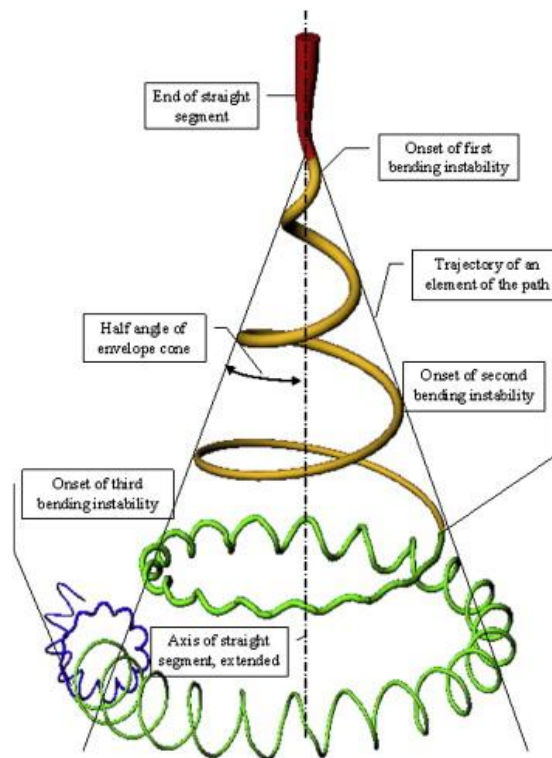
Figure 1.6. The schematic representation of the instantaneous position of the path of a electrospinning jet that contained three successive electrical bending instabilities (Source: Reneker and Yarin 2008)

The jet deviates from its straight path in the instability region, and undergoes an instability referred to as bending or whipping instability (Hohman et al. 2001b, a, Reneker et al. 2000, Yarin et al. 2001).This region may also be examined as three segments. The jet path continued and transformed to a smaller three-dimensional coil, with an axis that followed the curved path extrapolated from the first coil. The second spiral eventually transformed to an even smaller spiral and so forth until the jet solidified, by evaporation of the solvent. After the onset of the electrically driven bending instability in electrospinning, every segment of the resulting coil moved outward and downward in a complicated, but not random way.

1.3.3. Potential Applications

The technique of electrospinning is remarkably simple and powerful when it comes to generating fibers which are ultra-thin from a wide array of different materials. This technique and resultant structures are attractive for a number of applications thanks

to the simplicity of the fabrication scheme, the diversity of materials which are suitable for use with electrospinning, as well as the unique and interesting features associated with electrospun nanofibers. The potential application areas of electrospun nanofibers are shown in Figure 1.7. Some of the applications which we focused on throughout thesis are as follows.
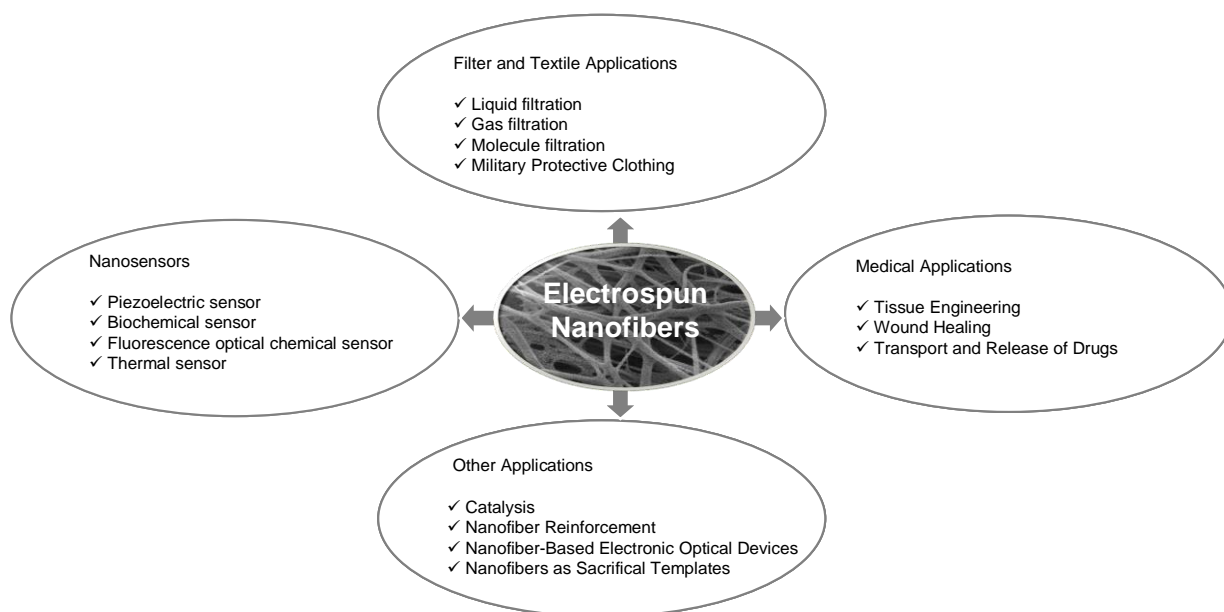
Figure 1.7. Potential applications of electrospun nanofibers

1.3.3.1. Filter Membranes

In the non-woven fiber industry, one of the fastest growing segments is in filtration applications. Traditionally, wet-laid, melt-blown and spun-bonded non-woven articles, containing micron-size fibers, are most popular for these applications because of the low cost, easy ability to be processed and strong filtration efficiency (Smorada 1996, Mayer and Warren 1998). Their applications in filtration can be divided into two major areas: air filtration and liquid filtration. In air filtration, non-woven articles have been used as coalescing filter media (Hajra et al. 2003), dust collector (Graham et al. 2004), and protective clothing with coatings of selective agents (Schreuder-Gibson et al. 2002). Non-woven articles have been used mostly as substrates to support porous membranes for ultrafiltration (UF, that can exclude particle size larger than 100 nm) or nanofiltration (NF, that can exclude particle size larger than a few nanometers) in liquid filtration (Zeman and A.L. 1996).

A unique feature of electrospinning is its ability to affect the diameter of the fiber (from tens of nanometers up to a few micrometers) by altering processing variable(s) including solution concentration, applied voltage, fluid flow rate and surface tension (Theron et al. 2004, Fridrikh et al. 2003). Adjusting the fiber diameter provides an opportunity to fine-tune the porosity of the membrane, which also depends on the thickness of the membrane. The pores in a non-woven structure (i.e. the empty space) are closely interconnected and would be particularly appropriate for fluid filtration under hydraulic pressure; the pores cannot be entirely blocked by particles which have penetrated the membrane. In liquid filtration, porous polymeric membranes manufactured by conventional methods have their intrinsic limitations, e.g. low-flux and high-fouling performance, due to the geometrical structure of pores and the corresponding pore size distribution, for example, produced by the phase immersion method (Wrasidlo and Mysels 1984) and undesirable macro-void formation across the whole membrane thickness (Paulsen et al. 1994). We could conclude that nanofibrous membranes produced by electrospinning are able to overcome of these limitations.

1.3.3.2. Nanofiber-Based Sensors

Tremendous progresses have been made in the development of ultrasensitive sensors in responding to the imperative needs for more timely and reliable detections in environmental monitoring, food inspection and medical diagnostics. Developments of electrospun nanomaterials, such as nanofibers and nanowebs, have offered opportunities to construct more efficient interfaces with electronic components whose size is comparable to that of molecules. The tiny size of the components may bring benefits to people, with some special size effects, such as quantization and single-molecule sensitivity. The relatively expansive specific surface area and considerable porosity of electrospun nanomaterials have attracted significant interest, because these properties closely meet requirements for ultrasensitive sensors (Ding et al. 2010).

The fabrication of polymeric nanowire chemical sensors was demonstrated by Liu et. al. They investigated the effect of orientation and diamaters of polyaniline nanowires on the sensing ability to Ammonia gas. Both response time and sensitivity of the nanostructures could be improved compared to film-based polyaniline sensors (Liu et al. 2004). The fluorescence-based porphyrin-doped nanocomposite fiber sensor for

the rapid detection of trace trinitrotoluene (TNT) vapor was fabricated by Tao and co-workers. It was found that constricting the diameter and introducing a pore structure into nanofibers could considerably enhance the sensitivity of the resulting materials (Tao et al. 2007). The performed experiments clearly indicated that the electrospun nanofibrous membranes and their assemblies may hold broad promise as active components for the sensing technology.

1.3.3.3. Catalysts

Both polymeric and ceramic Electrospun nanofibers provide another attractive class of solid support for conventional catalysts and enzymes by virtue of their compactness and relatively significant surface area. In this vein, Demir et al. investigated the catalytic activity of palladium-incorporated nanofibers in the selective hydrogenation of dehydrolinalool. The study found that the catalytical activity of such fibers was 4.5 times higher than the traditional Pd catalyst supported on alumina powders (Demir et al. 2004).

The removal and recycling of the catalysts after the reaction is a crucial stake in the catalysis process. One intriguing solution to this is the undertaking of immobilization of homogeneous or heterogeneous catalysts in nanofibers. The homogeneous catalyst, which is comprised of core–shell nanofibers combined with proline and scandium triflate $Sc(OTf)_3$ ($TfO=CF_3SO_3$) catalysts was fabricated by the tubes by fiber templates (TUFT) process. Complete conversion of the fiber systems can be achieved in the same or shorter reaction times, in contrast to the conventional catalysis in homogeneous solutions. The fibers can be used several times without loss of activity (Stasiak et al. 2007). Lindner et. al. reported reusable dendritic catalysts 'bottled' in poly "bottled" in poly(p-xylylene) (PPX) nanotubes through conjugation of poly(amidoamine) (PAMAM). The nanotubes displayed activity as a recyclable catalyst in a Knoevenagel reaction (Lindner et al. 2009). Additionally, nanofibers were employed as carriers for enzymes, where enzymes were either chemically attached to the electrospun fibers or directly dispersed in the nanofibers during the process of electrospinning (Jia et al. 2002, Wang, Wan, et al. 2009). High catalyst activities were also reported in this study.

CHAPTER 2

SORPTION EFFICIENCY OF CHITOSAN NANOFIBERS TOWARDS METAL IONS AT LOW CONCENTRATIONS

2.1. Abstract

Nanometer-sized chitosan fibers showing narrow diameter distribution with a mean of 42 nm were produced by electrospinning and utilized for sorption of Fe(III), Cu(II), Ag(I), and Cd(II) ions from aqueous solutions. Filtration efficiency of the fibers was studied by both batch sorption and microcolumn methods, and the ion concentrations remained in the filtrates was determined by inductively coupled plasma-mass spectrometry (ICP-MS). High efficiency in sorption of the metal ions was obtained in both methods. In former method, sorption parameters including the effect of sorbent amount (0.10-0.50 mg), shaking time (15-120 min), initial metal ion concentration (10.0-1000.0 μg L^{-1}), and temperature (25 and 50 °C) were examined. The sorbent amount did not significantly alter the efficiency of sorption; however, shaking time, temperature, and metal ion concentration were found to have strong influence. By virtue of the mechanical integrity, the applicability of the chitosan mats in solid phase extraction under continuous flow looks promising.

2.2. Introduction

Ground water pollution originating from both natural and anthropogenic sources forms a detrimental problem to the environment. Metal ions are released into the environment from a variety of natural sources including mineral and metallic deposits in sedimentary rocks and soil. Manmade activities such as mining, plating, glass making, ceramics, and battery manufacturing also lead to a great increase in heavy metal contamination in water, causing an ongoing risk to the biosphere. Cadmium, for instance, is one of the most toxic metals for the biosystems that accumulates in the human body, especially in the kidneys. The intake of overdoses of cadmium has been

reported to cause renal diseases, prostate cancer, and bone lesions (Benguella and Benaissa 2002). Excessive intake of copper, as another example, causes damages to liver, kidneys, and intestinal system (Ngah et al. 2002). Moreover, iron in drinking water or water supplies bring about problems regarding the quality of water such as providing reddish color, metallic taste and odor (Cho 2005). When silver or its compounds come into contact with the skin, they may cause permanent discoloration known as argyria. Although Cu and Fe are essential elements for the living organisms, they become potentially toxic at higher concentrations; thus, their contents must be kept at certain threshold levels. The maximum contamination levels (MCL) in drinking water set by Environmental Protection Agency (EPA) are 0.005 mg L^{-1} for cadmium, 1.3 mg L^{-1} for copper, 0.3 mg L^{-1} for iron, and 0.05 mg L^{-1} for silver.

The removal of toxic metals from aqueous solution can be achieved using different methods including ion exchange (Lee et al. 2001, Ngah and Fatinathan 2010), reverse osmosis (Yang and Zall 1984), chemical precipitation (EPA 2000), and coagulation (Assaad et al. 2007). Among the applicable methods, sorption has been recognized as the most optimum one due to its high efficiency, ease of implementation, and low cost (Justi et al. 2005, Li and Bai 2005, Ng et al. 2002). Sorption of aqueous metals can be realized by employing sorbents that contain functional groups possessing metal binding ability such as amino (Li et al. 2008), carboxyl (Wong et al. 2003), phosphoric (Puziy et al. 2004), mercapto (Mondal and Das 2003), amidoxime (Nilchi et al. 2008, Saeed et al. 2008), and the like.

Chitosan is a nontoxic, biodegradable polymer derived from naturally occurring chitin, which is found in the exoskeleton of crustacean shells, such as crabs, insects, and shrimps. It is the largest biomass polysaccharide component along with starch. The main structure of chitin is the *β*-linked *N*-acetyl-D-glucosamine and upon *N*-deacetylation, it is transformed into chitosan by thermochemical alkaline treatment. Chitosan $(C_6H_{11}NO_4)_n$ has been widely reported as an effective sorbent of metal ions. It has a mass of 161 g per unit monomer, and has a concentration of amino group $(-NH_2)$ of 6.21 mmol g^{-1} if it is completely deacetylated (Wu et al. 2010). The extent of deacetylation controls the fraction of free amine groups and hydroxyl groups on chitosan (Ngah et al. 2002). In order to enhance the sorption capacity, physical and chemical methods (Miretzky and Cirelli 2009) have been used to modify this natural polysaccharide. Chitosan with different morphologies such as powder (Gamage and Shahidi 2007, Juang and Shiau 2000), bead (Lee et al. 2005, Li, Bai, et al. 2005, Ngah

and Fatinathan 2008, Twu et al. 2003), membrane, microsphere (Vieira and Beppu 2006a, Zhou et al. 2009), fiber (Desai et al. 2008, Desai et al. 2009, Haider and Park 2009, Vieira and Beppu 2006a, Zhou et al. 2009), and their cross linked forms (Chen, Liu, et al. 2008, Ngah et al. 2005, Vieira and Beppu 2006b) has been used to remove heavy metals from aqueous systems. Surface area of sorbents is known as the most important parameter in sorption studies. Larger surface area provides higher number of available active sites and results higher sorption activity. Therefore, attempts have been made to increase surface area of chitosan sorbent. For example, drying in supercritical CO_2 was used as a method to improve surface area of chitosan structures (Okamoto et al. 2003). Application of this process allows to generate porosity and enlarges surface area (close to $110 \ m^2 \ g^{-1}$) to be potentially used in catalysis (Valentin et al. 2003).

Among other diverse fields, water treatment is an important field that can benefit from the advances in nanoscale science and engineering. Nanotechnology based products that are capable to reduce the concentrations of toxic compounds to sub-ppb levels can enhance water quality standards and sanitations. Fibrous materials prepared by electrospinning process are increasingly attracting attention in this field due to the structural advantages conveyed by the nanosized diameter of the constituent fibers. The fiber diameter can be controlled by solution properties (viscosity, conductivity, and surface tension) and instrumental parameters (applied electrical field and flow rate) of the electrospinning process (Demir et al. 2004, Demir et al. 2002). The fibers exhibit high mechanical integrity which is a desired property for filtration process under continuous flow. Moreover, the nanosized diameters of fibers provide much enhanced functionalities which can not be obtained by bulk materials (Greiner and Wendorff 2007). Along with filtration (Haider and Park 2009, Sang et al. 2008), electrospun fibers can be used in potential and existing technologies such as biosensors (Frey et al. 2009), drug delivery (Jiang et al. 2004), wound dressing (Chen, Chang, et al. 2008), and protective clothing (Yarin and Zussman 2004b). Although the filtration efficiency of chitosan and chitosan derivatives has been known for many years, the studies that focus on the efficiency of electrospun chitosan fibers are scarce. Previously, electrospun chitosan fibers were applied for the removal of chromium ion (Desai et al. 2008). Chitosan was blended with poly (ethyleneoxide), (PEO) in solution to improve its processibility in electrospinning process. While PEO brings electrospinnability to the blend system, the binding ability of metal ions in filtration process was attributed to chitosan. The blending of the similar material components was also used for removal of

pathogenic microorganisms and $Cr_2O_7^{2-}$ ions demonstrated by the same group of authors (Desai et al. 2009). Another interesting study related to metal ion filtration by electrospun chitosan fibers was reported by Park et al (Haider and Park 2009). The authors used chitosan itself without using additional material component like polyethylene oxide or polyvinyl alcohol. The dissolution of chitosan was achieved by trifluoroacetic acid (TFA) and electrospun fibers were neutralized by K_2CO_3. The chitosan fiber mats exhibited good erosion stability and high metal binding capacity in aqueous solution. In the present study, chitosan nanofiber mats were prepared via electrospinning. The filtration performance of the fiber material was then tested for Fe(III), Cu(II), Ag(I), and Cd(II) ions in aqueous solution. Both of batch and microcolumn sorption methods were employed to characterize sorption over a range of experimental parameters.

2.3. Experimental Section

2.3.1. Materials and Methods

Medium molecular weight chitosan powder was used as received from Sigma-Aldrich. Reagent grade glacial acetic acid and sodium chloride were obtained from Riedel-de Haen. Viscosimetry was employed for determination of molecular weight of the chitosan powder using the Mark-Houwink equation; $[\eta] = KM_v^{\alpha}$, where K and α are the specific constants for a given polymer and vary for the used solvent system and temperature (Planas 2002). The constants, K and α of chitosan were determined as 1.81×10^{-3} cm^3 g^{-1} and 0.93, respectively, when 0.20 M NaCl/0.10 M acetic acid solvent system were used (Kasaai 2007, Taghizadeh and Davari 2006). A Petrotest capillary viscosimeter (Dahlewitz, Germany) was used to measure the viscosity of chitosan/acid solution at 25 ºC. The degree of deacetylation (*DD*) of chitosan was determined by titrimetric (Tolaimate et al. 2000) and elemental analysis (Kasaai et al. 2000) methods. The potentiometric method depends on the titration of chitosan with standardized NaOH (Merck) solution, used to deprotonate positively charged amine groups in chitosan. For this purpose, 250.0 mg portion of chitosan was dissolved in 10.0 mL of 0.30 M HCl (Merck) and after being diluted to 50.0 mL with ultra pure water, it was titrated with 0.100 M NaOH solution. The consumed volume of NaOH which corresponds to the

amount of amine groups in chitosan is obtained from the difference between two inflection points of acid-base titration. Equation 1 describes the formulation used in the calculation of *DD* by the titrimetric method. In this equation, 161 is the molecular weight of glucosamine unit of chitosan, 42 is the difference in the molecular weights of chitin and chitosan repeating units, *m* is the mass of the chitosan sample, *ΔV* is the volume and *M* is the molarity of NaOH solution. *DD* was also verified by elemental analysis which is the second method we employed. The elemental compositions of these samples were determined by a LECO-CHNS-932 elemental analyzer (Mönchengladbach, Germany). The results of elemental analysis were also used for calculation of *DD* of chitosan. Since deacetylation process removes two carbon atoms and one oxygen atom from chitin, chitosan differs in its C and O contents while N remains unchanged. Therefore, C/N ratios are used in the determination of *DD*. Equation 2 is used for determination of *DD* where, 5.145 is the ratio of C/N in completely N-deacetylated chitosan repeating unit and 1.671 is the difference between the C/N ratios of chitin and chitosan.

$$D.D. = 1 - \frac{\left(1 - 161 \times \dfrac{\Delta V \times M}{m}\right)}{\left(\dfrac{\Delta V \times M}{m} \times 42 + 1\right)} \qquad (2.1)$$

$$D.D. = \left(1 - \frac{C/N - 5.145}{1.671}\right) \times 100 \qquad (2.2)$$

2.3.2. Electrospinning of Chitosan

Chitosan solutions were prepared by dissolving chitosan powder (M_v= 1096 kDa and 70-75% degree of deacetylation) in 1,1,1,3,3,3-Hexafluoroisopropanol (HFIP) (Sigma-Aldrich). The solutions were stirred for 2 days to achieve homogeneous and clear solution. The chitosan solutions were placed in a 20.0 mL syringe fitted with a metallic needle of 0.2 mm of inner diameter. The syringe was fixed horizontally on the

microsyringe pump (LION WZ-50C6) and the electrode of the high voltage power supply (Gamma High Voltage Research Ormond Beach, FL, US) was attached to the metal needle tip.

Figure 2.1 shows the schematic diagram of electrospinning setup and a photographic image of the resulting fiber mat. The concentration of the chitosan was kept constant at 0.4 wt % of the solution. An electrical field of 1.1 kV cm^{-1} (the applied voltage: 8 kV and the tip-to-collector distance: 7 cm) was applied to the solution, and the deposition time was adjusted to obtain a dense film. The flow rate of the polymer solution was 0.8 mL h^{-1}, and the electrospinning was performed in a horizontal position at room temperature. A mat-like film was obtained on the grounded aluminum plate. The electrospun fiber mat was removed easily, washed with acetone, and dried under vacuum at 60 ºC overnight.
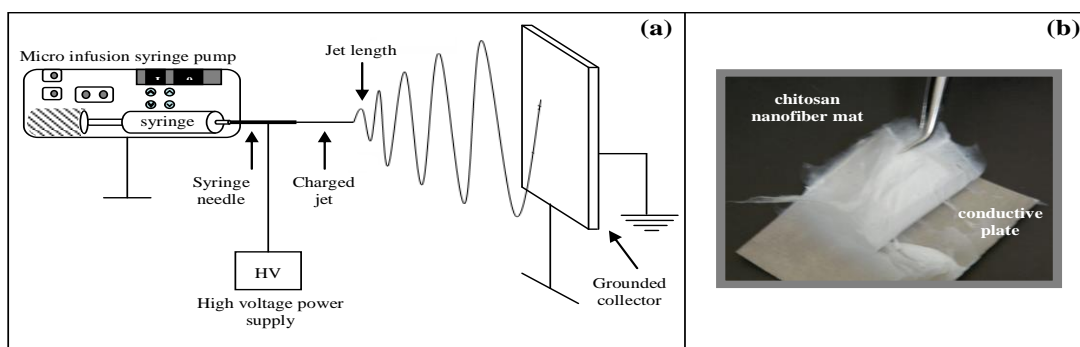
Figure 2.1. Schematic representation of (a) electrospinning setup, and (b) photographic image of the resulting fiber mat

2.3.3. Structural Characterization of Electrospun Mat

The morphology of electrospun chitosan mat was characterized by a scanning electron microscope (SEM, Philips XL-30S FEG) after coating the sample with gold. The average fiber diameter was determined by statistical treatment of the SEM images with the image processing software, ImageJ (Rasband 2010). The diameter distribution of the electrospun fibers were obtained by measuring at least 100 test fibers. The crystalline structure of the samples was analyzed using an X-ray diffractometer (Philips X'Pert Pro X-Ray Diffractometer). Fourier transform infrared spectroscopy (FTIR) measurements of the samples were performed with Perkin Elmer Spectrum 100 FTIR

Spectrometer (Shelton, USA) with Pike Miracle single reflection horizontal attenuated total reflection (ATR) accessory. The surface area of the fiber sample was measured with a Micromeritics Gemini V Brunauer-Emmett-Teller (BET) analyzer with N_2 gas.

2.3.4. Sorption Studies

The electrospun chitosan fiber mat was used as a sorbent for the removal of Fe(III), Cu(II), Ag(I), and Cd(II) ions from aqueous solution. Stock standard solutions (1000.0 mg L^{-1}) were prepared by dissolving $FeCl_3.6H_2O$ (Merck), $CuSO_4.5H_2O$ (Riedel-de Haen), $AgNO_3$ (Sigma-Aldrich), and $CdCl_2$ (Merck) in ultra-pure water (18.2 MΩ cm). The working standard concentrations of the ions were then obtained by serial dilution. The sorption experiments encompassed the effects of the sorbent amount, shaking time, initial ion concentration, and sorbent type on the extent of fixation of the aforementioned cations.

The chitosan fiber mats were immersed in 3.0 mL of 100.0 μg L^{-1} multielement solution (adjusted to pH of 6.0) and continuously shaken in a GFL 1083 water bath shaker (Burgwedel, Germany) equipped with microprocessor. Following each of the batch experiments, the liquid solution was separated from the fiber sorbent by centrifugation and the supernatant phase was analyzed for its iron, copper, silver or cadmium content using ICP-MS (Agilent 7500ce Series, Japan). The ICP-MS operating conditions are provided in Table 2.1.

In addition to batch sorption studies, microcolumn tests were also performed for the sake of comparison. These studies were employed using a home-made microcolumn system involving PTFE tubing with internal diameter of 1.5 mm and a height of 6.0 cm. The substrate chitosan fibers were folded and immersed into the flexible tube. Cylindrically shaped small sponge pieces were squeezed into both ends of the tube such that chitosan fibers were sandwiched and the back-pressure of the continuous flow was prevented. In each trial, a 3.0 mL aliquot was passed through the sorbent tube. Additional tubes connecting the microcolumn to peristaltic pump tubing were inserted at both ends of the columns. The flow rate of the solution was adjusted to 0.15 mL min^{-1}. This process was performed 13 times, consecutively. For the sake of control, parallel experiments were conducted by both batch and microcolumn tests, in which Fe(III), Cu(II), Ag(I), and Cd(II) ions free of chitosan fiber were used.

Table 2.1. ICP-MS Operation Parameters

Operation Parameters	Value
RF power	1550W
Make up gas flow rate	0.27 L min^{-1}
Argon carrier gas flow rate	0.85 L min^{-1}
Octopole collision gas flow rate	(He) 4.5 mL min^{-1}
Chamber temperature	2 ºC
Sample depth	7 mm
Nebulizer	Concentric
Nebulizer pump	0.1 rps
Tune setting (m/z)	7, 89, 205
Isotopes monitored (m/z)	^{56}Fe, ^{57}Fe, ^{63}Cu, ^{107}Ag, ^{111}Cd

Metal solutions at concentrations of 5.0, 10.0, 25.0, 50.0, 100.0, 200.0, 500.0, and 1000.0 μg L^{-1} were prepared by serial dilution of 10.0 mg L^{-1} stock solutions of Fe(III), Cu(II), Ag(I), and Cd(II) ions. All samples and standard solutions were acidified by adding proper amounts of concentrated HNO$_3$ to produce 1.0 % (v/v) HNO$_3$ in the final solution. The percentage sorption and the metal ion concentration on the fibers were calculated using the following equations:

$$Sorption \ \% = \frac{C_i - C_f}{C_i} \times 100 \tag{2.3}$$

$$q(\mu g / g) = \frac{(C_i - C_f)V}{M} \tag{2.4}$$

where C_i is the initial concentration, C_f is the final concentration of the ions in solution (µg L^{-1}), V is the solution volume (L) and M is the sorbent fiber amount (g) (Sang et al. 2008)

The selectivity of the nanofiber mat against a certain cation was also examined. The selectivity is expressed in terms of the distribution coefficient (*D)* (Rodrigues 1986), calculated using the equation below.

$$D = \frac{mg\, M^{n+}\, /\, g\, of\, polymer\, adsorbent}{mg\, M^{n+}\, mL\, of\, solution} \qquad (2.5)$$

Attention was paid to measure the concentration of any residual fluoride ion that would be potentially desorbed from the electrospun mat into solution. The concentration of fluoride ion was followed by Ion Chromatography (IC).

2.4. Results and Discussion

2.4.1. Electrospinning of Chitosan and Structural Characterization of Electrospun Mat

Both solution and instrumental parameters of electrospinning were varied for chitosan/HFIP system. The process was optimized as electrospinning of 0.4 wt % solution at an electric field of 1.1 kV cm^{-1} under a flow rate of 0.8 mL h^{-1}. Panel a and b of Figure 2.2 present SEM micrographs of powder and electrospun nanofibers of chitosan, respectively, at different magnifications. When the chitosan powder was electrospun, its morphology changed drastically from bulk into nonwoven fibrous material. Panel c shows diameter histogram and Gaussian distribution of the electrospun nanofibers. The fibers have uniform diameter with 42 ± 15 nm.

Electrospinning of chitosan from solution is problematic due to its limited solubility and the presence of high degree of intermolecular and intramolecular interactions. In particular, low surface tension solvents or solvent compositions have been frequently used for electrospinning of chitosan for example TFA and HFIP (Ohkawa et al. 2004, Sangsanoh and Supaphol 2006, Schiffman et al. 2009). However, the usage of volatile and corrosive nature of these solvents may raise some

environmental concern. Potential release of this molecule could be disadvantageous and limit the applicability of the fibrous chitosan sorbent in water treatment.

To figure out the content of HFIP in our particular system, the decantate was analyzed after sorption experiments using Ion Chromatography (IC). The results of measurements showed that the concentration of fluoride ion is around 0.022 mg L^{-1}. This concentration is two orders of magnitude lower than the threshold set by World Health Organization (1.5 mg L^{-1}) (WHO 2004). Consequently, this level of fluoride is not risky as expected at least for the sorbent amount employed.

Nitrogen adsorption/desorption measurements were conducted to determine the BET surface area of the fibers. The shapes of the isotherms for powder and electrospun fibers are provided in panel a of Figure 2.3 Increasing the relative pressure does not vary the quantity of N_2 adsorbed on chitosan powder, however, a linear increase in adsorbed N_2 is observed for electrospun fibers. At a given temperature the isotherms for the chitosan nanofibers and the powders have a different shape. This difference can be explained by the larger effective surface area in fibrous electrospun mat compared to the powder. The BET surface area is calculated from the isotherms to be about 0.92 m^2 g^{-1} for the powder and 22.4 m^2 g^{-1} for the electrospun fibers, *i.e.* more than twenty-fold increase of the surface area of chitosan were observed upon electrospinning. Increasing the surface area results in higher number of exposed binding sites for the metal ions.

X-Ray Diffraction pattern of chitosan powder is given in Figure 2.3b. Two prominent reflections at 10° and 20° are evident. These signals, which are in agreement with the literature (Schiffman et al. 2009), can be attributed to hydrated crystals of chitosan. The crystalline form of chitosan powder disappears upon electrospinning, indicating that the resulting fibers have amorphous texture. Since rapid solidification takes place during the process, the stretched molecular chains do not have enough time to align into three dimensional ordered crystal structures (Zhou et al. 2008). Figure 2.3c demonstrates the FTIR spectra of chitosan powder and electrospun chitosan nanofibers. Both spectra contain broad –OH stretching absorption bands between 3600 and 3300 cm^{-1}. The absorption band observed between 3000 and 2800 cm^{-1} is attributed to the aliphatic C–H stretching. In the carbonyl region of the both spectra, the absorption band centered at around 1400 cm^{-1} is a characteristic band of chitin. The presence of these signals indicates that *N*-acetyl amino groups of chitin are still present in the system, *i.e.* chitosan is not completely deacetylated. The percent of deacetylation was determined as 70-75 % as mentioned in the experimental part, indicating that 25-30 % of the repeating

glucose units remain in acetylated form. A characteristic group of free primary amino group (–NH₂) at C2 position of glucosamine is present in chitosan. The band related with the bending of this group is identified within the spectral range of 1200-1000 cm^{-1}.
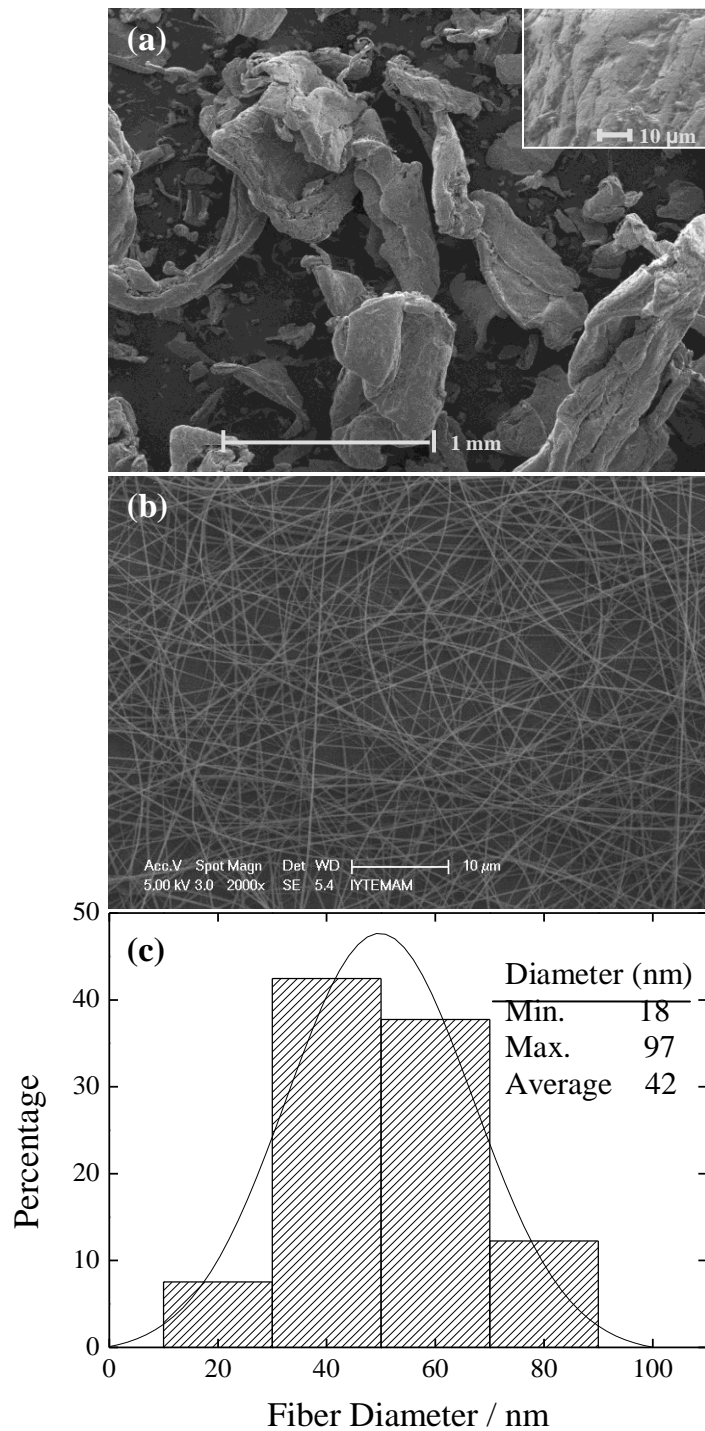
Figure 2.2. SEM micrographs of (a) chitosan powder, (b) electrospun mat, and (c) diameter histogram of the electrospun nanofibers
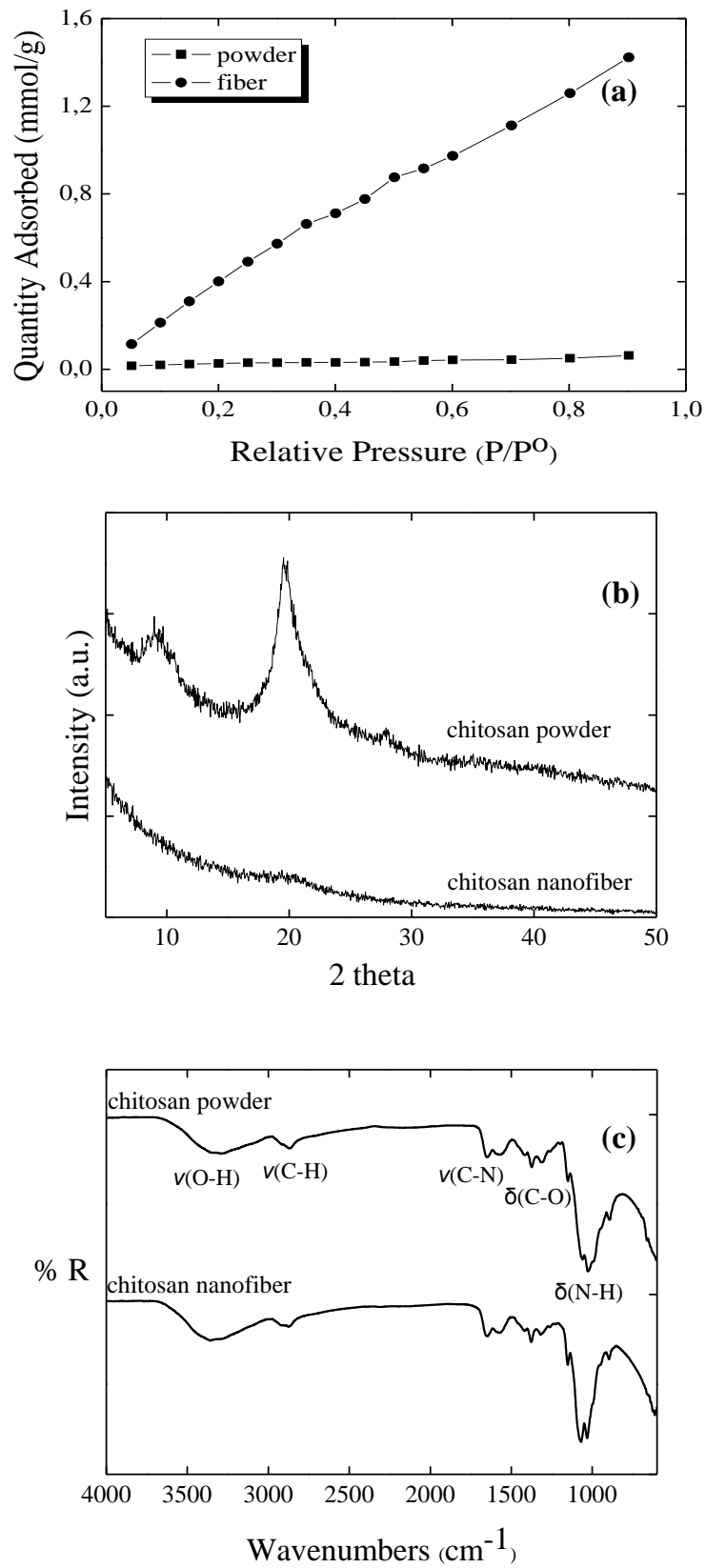
Figure 2.3. Structural characterization of the chitosan powder and electrospun chitosan fibers by means of (a) BET isotherm data, (b) X-ray diffraction patterns, (c) ATR-FTIR spectra

2.4.2. Sorption Studies

Figure 2.4a shows the sorption percentage of Fe(III), Cu(II), Ag(I), and Cd(II) ions onto a chitosan nanofiber mat in a 100.0 $\mu g\ L^{-1}$ synthetic multielement solution as a function of sorbent amount. The experiments were conducted at pH of 6.0 to prevent the formation of metal hydroxides at higher pH values. Lower pH values were also avoided due to possible solubility of chitosan fibers as a result of protonation of the amine groups. As the sorbent amount increases, the sorption percentage of the ions increases slightly. This observation may be explained as follows. Electrospun fibers are randomly distributed as independent filaments without having preferential alignment. When fibers stay long time in solution under shaking, the fibers assemble in solution into fiber bundles. The mechanism of this process is not fully understood in literature (Demir et al. 2008). However, it is regarded as disadvantageous because it leads to decrease of surface-to-volume ratio of the system. Assembling of sorbents will yield a reduction in the specific surface area and an increase in the kinetic (diffusion) barrier against sorption of aqueous ions, hence hindering the effectiveness of the sorbent entities and lowers the efficiency of sorption. Since the production of electrospinning is slow, the smallest amount of chitosan nanofiber sorbent (0.10 mg) was fixed in all experiments. Another tentative explanation for reduction in sorption at high sorbent amount could be the aggregation of sorbate entities. It is generally assumed that the sorbate ions are individually and homogeneously dispersed in the solution medium. However, this might not always be the case. Such presumed aggregation will reduce the area of contact between the sorbate and solution medium, thus decreasing the extent of sorption. In addition, kinetically, any plausible aggregation will slow down sorption due to imposing further surface diffusion necessity on the sorbed ions.

The percentage sorption at different shaking times is illustrated in Figure 2.4b. As expected, the extent of sorption of Fe(III), Cu(II), Ag(I), and Cd(II) increased with shaking time and maximum sorption was achieved for each metal ion at about 60 min of contact time. Prolonged exposure to 120 min resulted in slight decrease in sorption, probably due to desorption of some weakly bonded ions. The loading percentage of chitosan nanofiber sorbent was approximately 95 % for copper, 94 % for iron, 87 % for silver, and 52 % for cadmium in the 60 min contact period.
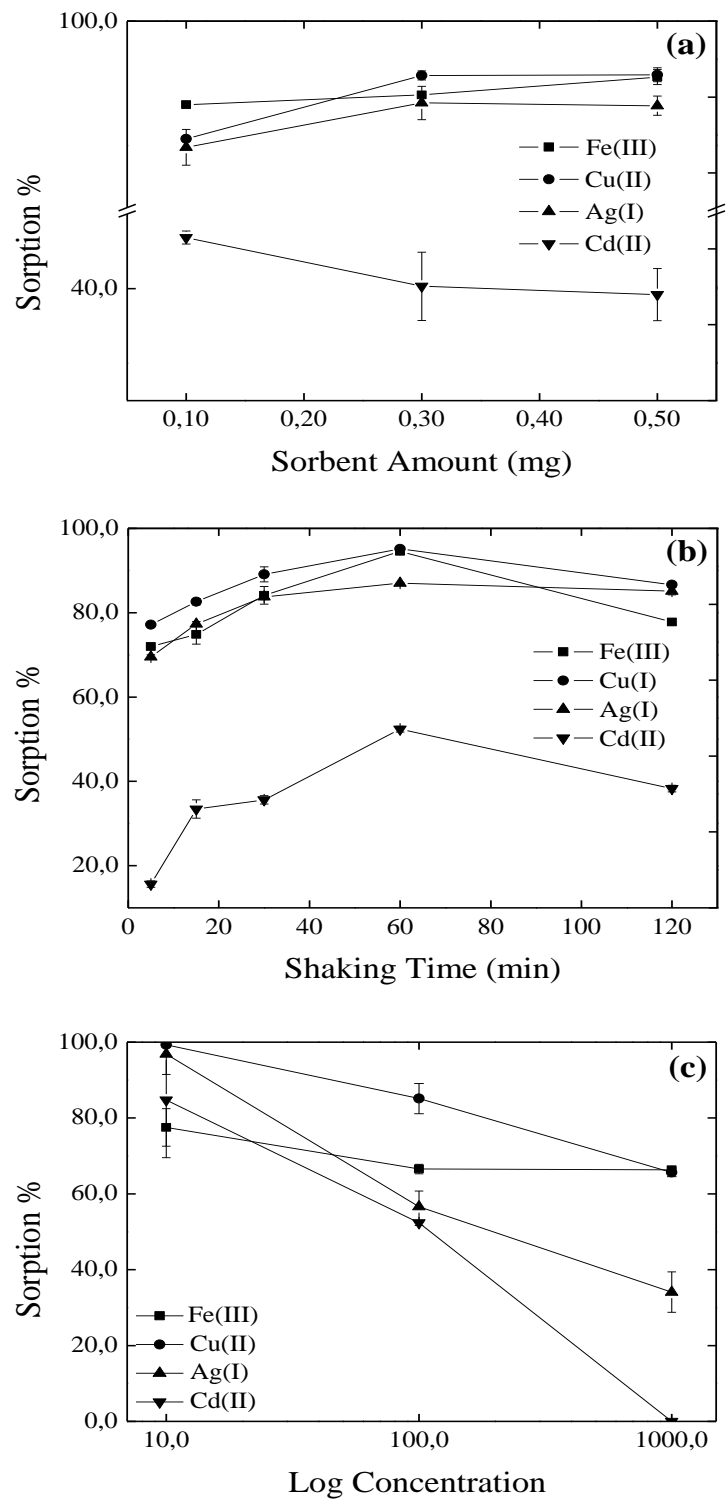
Figure 2.4. The effects of (a) sorbent amount, (b) shaking time, (c) initial metal ion concentration on the sorption of Fe(III), Cu(II), Ag(I), Cd(II) on chitosan nanofibers at pH=6

The effect of initial concentration of metal ions on the sorption behavior of chitosan nanofiber mat was determined for the concentrations of 0.01 mg L^{-1}, 0.1 mg L^{-1}, and 1.0 mg L^{-1}. The results, given in Figure 2.4c, indicate that, except for Fe(III), the sorption of metal ions decreased almost linearly with the increase in the initial metal ion concentration. The percentage sorption of Fe(III) was higher than 65 for all the concentrations tried. Maximum sorption percentages of 99 % for copper, 97 % for silver, 85 % for cadmium, and 78 % for iron were obtained at 0.01 mg L^{-1}, where the concentration of the analyte is not sufficiently high to saturate all available functional sites. Increasing the initial concentration to higher value resulted in differences of affinity of the sorbent toward the analytes. As it is usually the case, increasing the initial concentration caused a decrease in percentage sorption. Increasing the ion concentration causes larger competition of the ions to reach the limited number of functional groups, with the ions accommodated by these groups being usually smaller in number compared to ions remaining in solution.

The selectivity of the sorbent against the metal ions was also examined. Figure 2.5 gives the distribution coefficients (D) (Rodrigues 1986) for Fe(III), Cu(II), Ag(I), and Cd(II) ions which were determined under competitive conditions. These coefficients are frequently used as a measure of the capacity of a sorbent towards the sorbates. The order of decreasing selectivity at 100.0 µg L^{-1} is Cu > Fe > Ag > Cd, whereas at 1.0 mg L^{-1}, the order becomes Cu $\cong$ Fe > Ag > Cd. The distribution coefficients of Cu and Ag are three fold larger at 100.0 µg L^{-1} than at 1.0 mg L^{-1}. Thus, the concentration of the analyte is significantly effective for the selectivity of the sorbent towards the analytes of interest.

The extent of removal of metal ions pertains directly to the operating mechanism. The sorption mechanism on chitosan is quite complicated. It depends basically on the structural properties of the polymer (like the number of monomer units, the degree of deacetylation, crystallinity, etc.). Moreover, the structural parameters are reported to affect the equilibrium and kinetic aspects of sorption (Guibal 2004). The speciation of the metal ions under the prevailing experimental conditions is another important parameter in determining the sorption mechanism. Under neutral-slightly basic pH conditions, the major mechanism of metal sorption is binding to the free electron pair on amine groups. It is reported that chitosan has the highest chelating ability in comparison to other natural polymers obtained from seafood wastes and many other natural substances like activated sludge (Varma et al. 2004). Nevertheless, the

contribution of hydroxyl groups to metal uptake can not be totally disregarded, especially under pH conditions leading to deprotonation of these groups. In addition, the pH of the medium and the presence of ligands can change the speciation of the metal ion in a way that may result in turning the chelation mechanism into the electrostatic attraction mechanism (Guibal 2004).
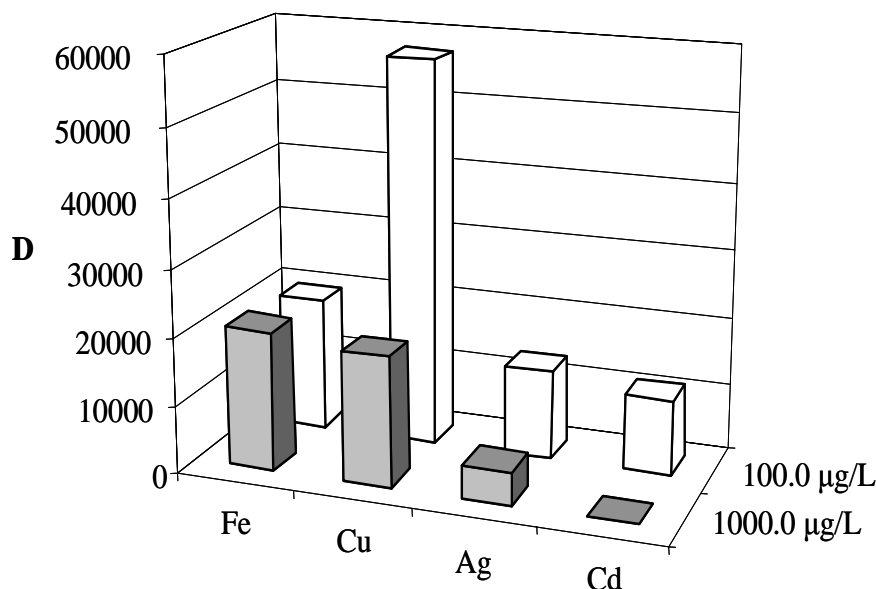
Figure 2.5. Sorption selectivity of chitosan nanofibers for the indicated metal ions at two different initial concentrations

As reported previously in this work, the extent of metal sorption was studied at pH of 6.0. At such pH, the deprotonation of amino and hydroxyl groups is not plausible, and as a result the metal ions seem to be fixed mainly by coordination to amine groups. The extent of such complexation is closely related to the speciation of those ions, their charge density, and electronic structure. Under the pH of our experiments speciation analysis using Visual MINTEQ (version 2.53) program suggests that the ions are expected to exist primarily in their 'bare' form (Ag^+, Cu^{2+}, Cd^{2+}, $Fe(OH)^{2+}$). Thus as a first approximation, it seems that the charge density and electronic structure (availability of unsaturated d orbitals) will determine the extent of complexation. The coordination mechanism might explain the relatively lower sorption of Ag^+ and Cd^{2+} in comparison to the Cu^{2+} and Fe^{3+}, as the d orbitals of Ag^+ and Cd^{2+} are full. From this perspective, Fe^{3+} would be expected to have the highest affinity, which is in line with the results observed at the highest studied concentration, i.e. 1.0 mg L^{-1}.

The preferential sorption behavior can also be explained in terms of steric reasons, *i.e.* ionic radii of the metal ions. The results obtained from the uptake of the metals throughout the study are in agreement of various results obtained with chitosan flakes that reported the same order of affinity for Cu^{2+} and Cd^{2+} (Bassi et al. 2000, Rhazi et al. 2002). It might be said that sorption of Cd^{2+} and Ag^+ is less favorable probably due to their larger ionic radii, the thing that might create mismatch to the binding sites on chitosan.

The mechanism can also be roughly viewed from another perspective. The liability of ions toward coordinative bonding with ligands can be explained based on hard-soft acid base principle (HSAB). This approach provides general guidelines that qualitatively describe the ion-ligand coordinative bond stability in light of the relative sizes and charge densities of the potential partners. Smaller ions with higher charge densities tend to behave as hard acids and bind preferentially to ligands of smaller size which behave as hard bases. On the contrary, larger ions with smaller charge densities (soft acids) would preferentially bind to ligands that are diffuse and bulky (soft bases). In our particular case, the amine group on the backbone of chitosan chains plays the main role in sorption of metal ions, and can be classified as a hard base. Based on HSAB principle, amine ligand will preferentially bind to hard acids (Fe^{3+} in this case) and demonstrate low tendency towards binding with soft acids (Ag^+ in this case), which is consisted with our experimental results, Both of Cu^{2+} and Cd^{2+} are classified as borderline acids, and as such, their different sorption affinities to amine groups can not be explained based on this approach.

The differences of sorption characteristics for commercial chitosan flake and the prepared nanofiber are illustrated in Figure 2.6. As seen, higher sorption was observed for the fiber in all cases. This result illustrates the most prominent advantage of the fibers prepared. The higher sorption of the fiber can be attributed to the increased surface area ($22.4 \text{ m}^2 \text{ g}^{-1}$) in comparison with commercial chitosan ($0.92 \text{ m}^2 \text{ g}^{-1}$), hence a much larger number of functional (surface active sites) are readily available for sorption in the case of the fiber. In addition, the crystallinity of the prepared sorbent was completely different from that of commercial chitosan which may also affect the sorption properties of the fibers (Guibal et al. 1999, Milot et al. 1998, Piron and Domard 1998).
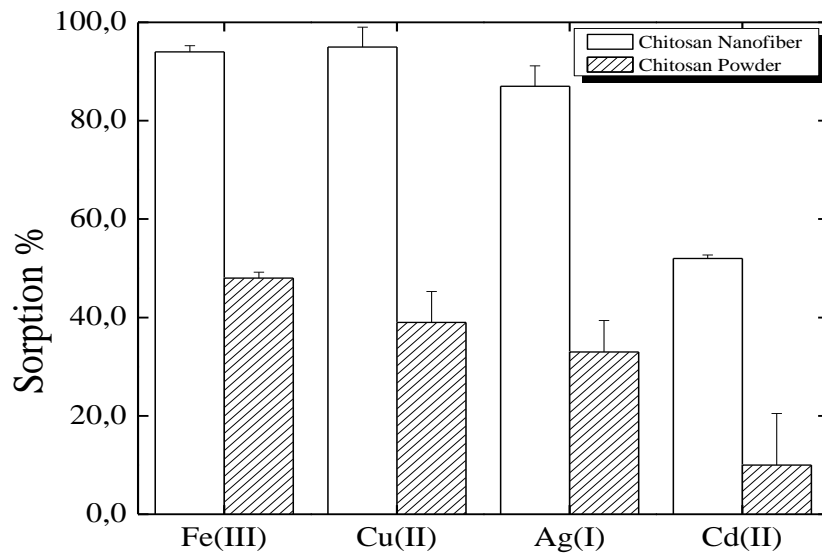
Figure 2.6. Comparison of the sorption efficiency of chitosan powder and chitosan nanofiber

To investigate the effect of temperature, two sets of sorption experiments were carried out at 25 °C and 50 °C. The obtained data was used to evaluate the apparent thermodynamic parameters of sorption as presented in Table 2.2, using a series of thermodynamic expressions (Shahwan et al. 2006).

$$\Delta H° = R \; In \; \frac{R_d(T_2)}{R_d(T_1)} \left(\frac{T_1 \, T_2}{T_2 - T_1} \right) \tag{2.6}$$

$$\Delta G° = -RT \; In \, R_d \tag{2.7}$$

$$\Delta S° = \frac{\Delta H° - \Delta G°}{T} \tag{2.8}$$

Table 2.2. Thermodynamic parameters of chitosan nanofibers (0.10 mg sorbent, 3.0 mL of 100.0 μg L^{-1} Fe(III), Cu(II), Ag(I), Cd(II), at pH 6.0, n = 3)

	ΔG° (kJ/mol)		ΔH° (kJ/mol)	ΔS° (J/molK)	
	298 K	323 K		298 K	323 K
Fe(III)	-27.2	-27.7	-21.4	19.5	19.5
Cu(II)	-29.9	-30.9	-17.3	42.2	42.2
Ag(I)	-31.0	-31.5	-25.9	17.3	17.3
Cd(II)	-25.0	-26.0	-13.0	40.3	40.3

The extent of sorption of the metal ions decreases as the temperature of the system increases, demonstrating an exothermic sorption behavior. This result is in line with the one reported earlier for As sorption on chitosan (Boyaci et al. 2010) The ΔS° values for Fe(III), Cu(II), Ag(I), and Cd(II) were found to be positive indicating that the system gains more entropy upon fixation of the ions. This could be resulting from dehydration steps of the ions upon sorption. The combination of ΔH° and ΔS° values yields negative ΔG° values, which characterizes situations in which the reaction products are favored over the reactants.
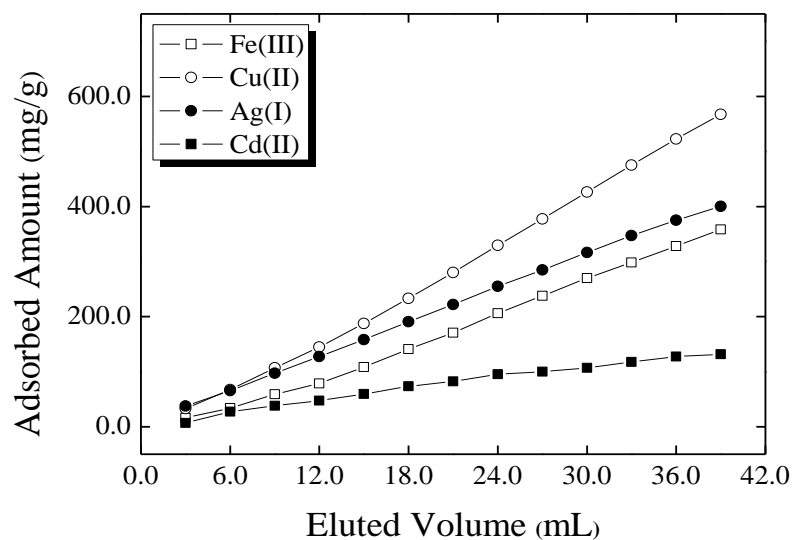
Figure 2.7. Microcolumn application of chitosan nanofiber mat on the sorption of Fe(III), Cu(II), Ag(I), Cd(II). (Note that each aliquot is 3 mL)

In order to investigate the applicability of the sorbents for column sorption studies, similar experiments were conducted with nanofiber-filled microcolumn. The sorption results obtained via column application are illustrated in Figure 2.7. These tests signify the adequacy of the prepared chitosan nanofibers for continuous removal of Fe(III), Cu(II), Ag(I), and Cd(II) from aqueous solutions. The first eluted 3.0 mL aliquots did not show significant differences in the extent of sorption of the studied ions, while further increase in solution volume significantly enhanced the difference between the sorbed amounts of the metal ions. Fe(III), Cu(II), and Ag(I) ions did not demonstrate sorption maxima after 39.0 mL of solution volume. This result states that the fibers are still active in sorption even after 13 repetition of elution. (thanks to electrospinning) On the other hand, Cd(II) ions almost reached maximum sorption. The lower sorption of Cd(II) was probably not related with saturation of the available functional groups, and may have resulted from different kinetic details and/or sorption mechanism in comparison to the other ions. Further investigation is required to clarify this issue. In addition, for Fe(III) and Ag(I) ions, the affinity of the nanofiber towards each ion is different from that observed in batch type sorption, while Cu(II) and Cd(II) show similar behavior with batch sorption studies.

2.5. Conclusion

Electrospinning of biopolymer chitosan is a difficult procedure due to its limited solubility in most organic solvents and strong inter and intrachain hydrogen bonding that leads to increase in viscosity of solution even at low weight fraction. In this study, uniform diameter of nanosized electrospun chitosan fibers were successfully fabricated by using medium molecular weight chitosan dissolved in HFIP. It was shown that chitosan nanofibers can be applied in the continuous removal of several metal ions. The environmentally friendly chitosan-based nanofibrous filter material has prominent benefits due to the high surface area per unit mass resulting from the very fine diameter. The results of the sorption study showed that shaking time, metal ion concentration, and temperature have strong influence on the sorption of Fe(III), Cu(II), Ag(I), and Cd(II) on chitosan nanofiber mat. In addition, Cu(II) was selectively filtered in contrast to Cd(II). Since the fibers are integrated to each other in a dense polymeric film, chitosan nanofiber mat can be used as sorbent for solid phase extraction (SPE) cartridges.

CHAPTER 3

CHITOSAN FIBER-SUPPORTED ZERO-VALENT IRON NANOPARTICLES AS A NOVEL SORBENT FOR SEQUESTRATION OF INORGANIC ARSENIC

3.1. Abstract

This study proposes a new sorbent for the removal of inorganic arsenic from aqueous solutions. Monodispersed nano zero-valent iron (nZVI) particles were nucleated at the surface of electrospun chitosan fibers (average fiber diameter of 195 $\pm$ 50 nm) by liquid phase reduction of $FeCl_3$ using $NaBH_4$. The material was characterized using SEM, STEM, XPS, and XRD. The diameter of iron nanoparticles was found to vary between 75–100 nm. A set of batch experiments were carried out to elucidate the efficiency of the composite sorbent toward fixation of arsenite and arsenate ions. The ion concentrations in the supernatant solutions were determined using inductively coupled plasma-mass spectrometry (ICP-MS). The results revealed that the chitosan fiber supported nZVI particles is an excellent sorbent material for inorganic arsenic uptake at concentrations ranging from 0.01 to 5.00 mg L^{-1} over a wide range of pH values. Based on XPS analysis, As(III) was found to undergo oxidation to As(V) upon sorption, while As(V) retained its oxidation state. By virtue of the successful combination of the electrospun fibers' mechanical integrity and the large reactivity of dispersed nZVI particles, the applicability of the resulting sorbent material in arsenic sorption holds broad promise.

3.2. Introduction

Arsenic, notoriously known for centuries as a poison, is currently considered as one of the most common and harmful water pollutants. The presence of dissolved arsenic in ground water affects the health of millions of people all around the world, and has given rise to a major environmental concern. Natural arsenic contamination of soil

and surface waters mainly originates from its geological presence and oxidative weathering. The discharge of industrial wastes resulting from anthropogenic activities like burning of coal, mining-related activities, usage of fertilizers and additives in agriculture contribute to arsenic pollution in ground water (Mandal and Suzuki 2002). A primary route of exposure of human body to arsenic occurs through the consumption of contaminated water and marine food which leads to arsenic poisoning or arsenicosis (Saha et al. 1999). Long term exposure to arsenicals eventuates in severe diseases as keratosis, gangrene or cancer (Choong et al. 2007). Acute poisoning shows symptoms such as bloody diarrhea and vomiting (Mohan and Pittman 2007). The predominant species of arsenic in natural ground and surface waters are either neutrally charged arsenite [As(III)] complex, or negatively charged arsenate [As(V)] oxyanions depending on pH, redox potential (Eh), and the presence of other chemical species. Arsenic is considered by the World Health Organization (WHO) to be among the chemicals of greatest health concern in some natural waters. The maximum contamination level of arsenic in drinking water set by WHO and the US Environmental Protection Agency (EPA) is 10 µg L^{-1}. Therefore, it is necessary to isolate arsenic from aqueous systems to avoid possible harmful exposure.

A number of arsenic removal technologies have been explored (Mohan and Pittman 2007). Many chemical treatments include oxidation/precipitation (Sun et al. 2009, Leupin and Hug 2005, Bissen and Frimmel 2003, Gihring et al. 2001), coagulation (Lacasa et al. 2011, Lakshmanan et al. 2010, Balasubramanian et al. 2009, Lakshmanan et al. 2008, Song et al. 2006, Wickramasinghe et al. 2004), sorption (Chutia et al. 2009, Boddu et al. 2008, Gimenez et al. 2007, Chen and Chung 2006, Deschamps et al. 2005, Cumbal and Sengupta 2005, Dousova et al. 2003, DeMarco et al. 2003, Lenoble et al. 2002, Dambies et al. 2000), ion-exchange (An et al. 2005, Kim and Benjamin 2004, Ghurye et al. 1999), and membrane technologies (Pagana et al. 2008, Iqbal et al. 2007, Shih 2005, Ning 2002). The traditional remediation processes based on sorption are characterized by its ease of application and low-cost (Daus et al. 2004). Various sorbents are available for arsenic removal such as activated carbon, activated alumina, silica, and titanium, zirconium, iron-based materials (Mohan and Pittman 2007). Although the efficiency of the aforementioned sorbents has been demonstrated, recent studies are proceeding for other innovative new materials. Nanoscale zero-valent iron (nZVI) technology has attracted considerable attention due to the high surface reactivity of the material which was reported to yield high arsenic

sequestration ability (Kanel et al. 2005, Kanel et al. 2006). However, the tendency of the nanoparticles to agglomerate impedes dispersibility and stability of the material and limits its potential in water remediation. Although nZVI particles allow for magnetic separation techniques (Ai et al. 2008, Karatapanis et al. 2012, Li et al. 2006, Sharma et al. 2009), their redispersion and accordingly reusability are not readily possible due to their strong magnetic interaction. The aggregation/agglomeration of the nanoparticles reduces significantly their effective surface area, as a result, their sorption efficiency. To overcome this problem, nZVI particles were either entrapped in a porous polymer (Geng et al. 2009, Gupta et al. 2012, Liu et al. 2012, Sun et al. 2011), supported on porous materials (Shi et al. 2011, Karabelli et al. 2011, Shahwan et al. 2010, Uzum et al. 2009, Xiao et al. 2009), or nanofibrous materials (Xiao et al. 2010, Xiao et al. 2011, Ma, Huang, et al. 2012). Chitosan is mostly chosen as a mechanical support because of its low-cost, wide availability, biodegradability, nontoxicity, as well as unique structural properties. The reactive amino groups on the backbone of chitosan enable fixation of several metal ions (Bailey et al. 1999). However, raw chitosan is not preferred for usage in the sorption of arsenic from water because of the pH limitation of chitosan in the arsenic uptake, reduced accessibility of chelating groups in case of crosslinked form (Crini 2005). Another disadvantage of raw chitosan is that it has poor physical nature and correspondingly low mechanical integrity leading to difficult isolation from the reaction media (Horzum et al. 2010).

Recently, Geng et al. proposed chitosan-stabilized nZVI particles produced by liquid phase reduction with potassium borohydride for the removal of hexavalent chromium in water.(Geng et al. 2009) The usability of Fe^0 nanowires modified with chitosan embedded in porous anodic alumina as sorbent towards the elimination of chromium ions was reported by Sun et al (Sun et al. 2011). To date, chitosan-nZVI based studies have mainly focused on the remediation of chromium ions. Distinctively, Gupta et al. evaluated that nZVI encapsulated chitosan spheres are potential candidate for the adsorption of total inorganic arsenic from aqueous systems (Gupta et al. 2012). Although the stability of Fe^0 nanoparticles was increased by the addition of chitosan, the resulting materials still have poor physical strength which is an undesirable property for filtration processes.

In this work, we focused on the fabrication of a new functional material which allows for advantageous combination of nZVI particles and electrospun chitosan fibers. Electrospinning has been known as versatile and efficient technique for the fabrication

of fibrous mats from a wide variety of both organic and/or inorganic materials (Huang et al. 2003). Electrospun nanofibers provide excellent characteristics as sorbents such as high surface area to volume ratio, enhanced surface functionalities, and superior mechanical performance compared with the powdered material (Horzum et al. 2010).

Due to the integrated high surface area inherent in both nanoparticles and submicron electrospun fibers which have also porous structure and high mechanical integrity, chitosan fibers-supported nZVI particles are optimal candidates for filtration applications. Contrasting to the available systems, we present a facile route to fabricate a new functional material, which overcomes the disadvantages of the nZVI particles and chitosan system such as agglomeration of the magnetic nZVI nanoparticles and pH limitation of chitosan particularly in acidic environment. The material was effectively used in As(III) and As(V) uptake from aqueous systems. The main advancement for the particular material combination arises from the following issues: (i) The proposed method is facile and yields a very effective material for sorption of As. (ii) The fiber material provides stable surfaces for the homogeneous dispersion of iron nanoparticles. (iii) The composite sorbent material composed of submicron sized nonwoven fibers possess high stability and mechanical integrity not only under shaking but also under continuous flow. (iv) The composite sorbent material can be repetitively used.

3.3. Experimental Section

3.3.1. Materials

All the chemicals were of reagent grade and were used without any further purification. Ultrapure water (Milli-Q Millipore 18.2 MΩ cm resistivity) was used throughout the study. Plastic containers and glassware were cleaned by soaking in diluted HNO_3 (10 %) and were rinsed with ultrapure water prior to use.

Medium molecular weight chitosan (M_v= 1096 kDa, 70-75% degree of deacetylation, Aldrich), iron(III) chloride hexahydrate (Merck, 99%), sodium borohydride (Aldrich, 98+%), ethanol (Sigma-Aldrich, ≥99.5%), As_2O_3 (Acros Organics, 99.5%), As_2O_5 (Merck, 99%), potassium dihydrogen phosphate (Alfa Aesar, 98%), magnesium chloride hexahydrate (Carlo Erba, 98%), and 1,1,1,3,3,3-Hexafluoroisopropanol (HFIP, Aldrich, ≥99%) were used as received without any

further purification.

3.3.2. Preparation of Chitosan Fiber-Supported nZVI

Figure 3.1 shows a facile route for the fabrication of chitosan fiber-supported nZVI particles. In a relevant experiment, the 0.4 wt% chitosan solution in HFIP was transferred to a 20 mL plastic syringe with a needle tip. The syringe needle was connected to a high voltage supply (Gamma High Voltage Research Ormond Beach, FL, US) and a potential of 10.5 kV was applied. The flow rate of the polymer solution was kept at 7.5 mL h^{-1} by using a microsyringe pump (LION WZ-50C6). The tip to collector distance was 5 cm. When the solvent evaporated, a mat-like chitosan film was obtained on the grounded aluminum plate and stored at room temperature.
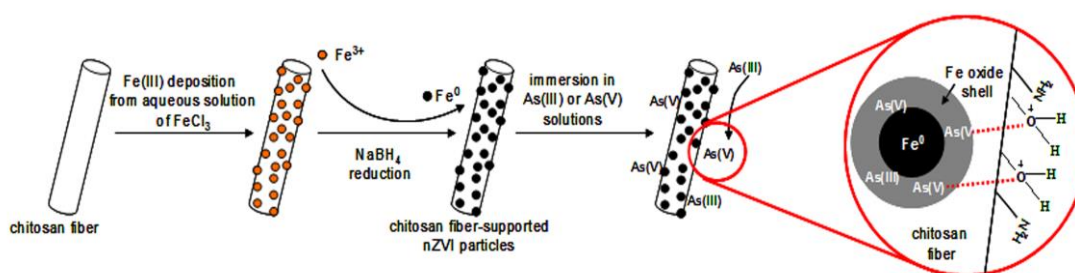
Figure 3.1. Experimental steps for the preparation of chitosan fiber-supported nZVI particles and proposed mechanism of As(III)/As(V) sorption

The growth of nanoparticles of zero-valent iron on the surface of the chitosan fibers was achieved by reducing iron ions using sodium borohydride. In the related experiments, 1.35 g FeCl$_3$·6H$_2$O (corresponding to 0.28 g iron) was dissolved in 25 mL of 4:1 (v/v) ethanol/water mixture, then 24 mg chitosan fiber was immersed into this solution and the mixture was vigorously stirred on a orbital shaker (IKA Vortex Genius 3) for 30 min. Fe^{3+} loaded chitosan fiber mat was then separated from the solution without any additonal washing steps and placed in a beaker. Meantime, 1.0 M sodium borohydride solutions were prepared such that BH$_4^-$/Fe^{3+} mole ratios were 1:1, 2:1 and 3:1. The amount of Fe(III) source was kept constant, while the concentration of NaBH$_4$ was gradually increased. The NaBH$_4$ solution was added to chitosan fiber mat drop by drop from the burette during stirring of the reaction mixture on a magnetic stirrer. After the addition of NaBH$_4$ solution, further mixing was maintained for 10 min. The

reduction reaction of ferric ions (Fe^{3+}) on chitosan fibers was marked by the formation of black particles characteristic for Fe^0. The reaction can be written as:

$$4Fe^{3+} + 3BH_4^- + 9H_2O \rightarrow 4Fe^0\downarrow + 3H_2BO_3^- + 12H^+ + 6H_2 \qquad (3.1)$$
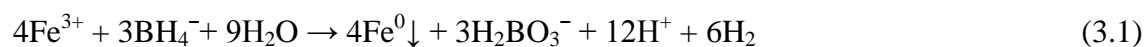
The solid material was separated from the liquid phase by vacuum filtration. The filtrate was washed with absolute ethanol in an ultrasonic bath for 5 min to remove any physically adsorbed nZVI. The washing procedure was repeated three times to stabilize nZVI against immediate oxidation. Finally, the prepared material was dried at 40 ºC overnight.

Scanning electron microscopy (SEM) was used for morphological characterization. This analysis was performed using a FEI Quanta250 FEG scanning electron microscope. Scanning transmission electron microscopy (STEM) mode was used to visualize nZVI particles on the surface of the chitosan nanofibers. The average fiber diameter was evaluated from the SEM micrographs for 100 individual fibers by using Fiji/ImageJ software. SEM micrographs were used also in the estimation of the surface area coverage of the nano- zerovalent iron particles using Scandium software (Soft Imaging System Corp.). EDX elemental mappings were obtained using ZEISS Libra 200FE TEM operating at 200 kV. Small chitosan nanofibres were mounted on holey carbon film supported on copper substrate, and elemental mappings at the fibers' thin edges for iron and carbon were revealed. The thermal properties of the sorbent were analyzed using a Perkin Elmer Diamond TG/DTA.

XPS spectra were acquired for chitosan-nZVI samples before and after the removal of each of As(III) and As(V) using VG Scientific ESCALAB 250 operating using Al K_α at 400 W. Data analysis and manipulation were performed using CasaXPS software, the binding energies for the collected photoelectrons were referenced using C 1s peak at 284.6 eV. X-Ray diffraction (XRD) was used for structural characterization of the composite material before and after sorption of As(III) and As(V). The XRD analysis was performed using a Philips X'pert Pro diffractometer monochromatized Cu K_α radiation (λ = 1.540 Å). Fourier transform infrared (FTIR) spectra were acquired using a Perkin Elmer Spectrum 100 FTIR Spectrometer (Shelton, U.S.A.), equipped with Pike Miracle single reflection horizontal attenuated total reflection (ATR) accessory.

3.3.3. Sorption Studies

Separate stock solutions of As(III) and As(V) ions were prepared at a concentration of 1000 mg L^{-1} by dissolving each of As_2O_3 and As_2O_5 in dilute HCl aqueous solution (1.0%, v/v). The initial concentrations used in the sorption experiments were 0.01, 0.05, 0.10, 0.25, 0.50, 1.00, 5.00, 10.0, and 25.0 mg L^{-1}, and were prepared by serial dilution from the stock solutions. The pH of the solutions was adjusted to 6.0 using 0.10 M and/or 1.0 M NH_3 or HNO_3.

Dried samples of chitosan fiber-supported zero-valent iron nanoparticles (0.50 mg) were immersed in 3.0 mL synthetic As(III) and As(V) solutions and continuously shaken in a GFL 1083 water bath shaker (Burgwedel, Germany) equipped with a microprocessor. The batch sorption experiments were performed as a function of initial concentration at 25 ºC for contact period of 1 h. The eluates were then separated from the fiber sorbent by centrifugation followed by decantation. The concentrations of the metal ions in solution after sorption were determined by ICP-MS (Agilent 7500ce Series, Japan). The ICP-MS operation parameters are given in Table 3.1.

Table 3.1. ICP-MS operation parameters

Operation Parameters	Value
RF power	1550 W
Make up gas flow rate	0,1 L min^{-1}
Argon carrier gas flow rate	0,87 L min^{-1}
Octopole collision gas flow rate	4,5 mL min^{-1}
Spray Chamber temperature	2 ºC
Sample depth	7,8 mm
Nebulizer	Concentric
Nebulizer pump	0,1 rps
Tune setting (m/z)	7,89,205
Isotopes monitored (m/z)	^{75}As, ^{56}Fe

The effect of pH was studied by adjusting the initial pH values to 4.0, 5.0, 6.0, 7.0, 8.0 and 9.0 using 0.10 M and/or 1.0 M NH_3 or HNO_3. For each experiment, separate 0.50 mg of chitosan/iron nanoparticles were placed into their respective solutions of 3.0 mL of 100.0 g L^{-1} As(III) and As(V). The speciation analysis of arsenic-containing ions at various pH values was performed using Visual MINTEQ software.

The extent of desorption was investigated by exposing the As-loaded fiber samples to 0.5 M KH_2PO_4 or 0.5 M $MgCl_2$ for 1h, and were then centrifuged and the supernatant solutions were finally analyzed for possibly released As ions.

3.4. Results and Discussion

3.4.1. Characterization of Chitosan-nZVI Fibers

The morphology and diameter distribution histogram of the chitosan fibers and chitosan fibers-supported nZVI particles are shown in Figure 3.2. SEM micrograph (Figure 3.2a) shows that the chitosan fibers have a smooth surface morphology with an average diameter of 195 ± 50 nm. ZVI nanoparticles were produced at the surface of electrospun chitosan mats by reducing $FeCl_3$ with $NaBH_4$. To obtain homogeneous particle dispersion on the chitosan fibers, the amount of BH_4^- with respect to Fe^{3+} was varied.
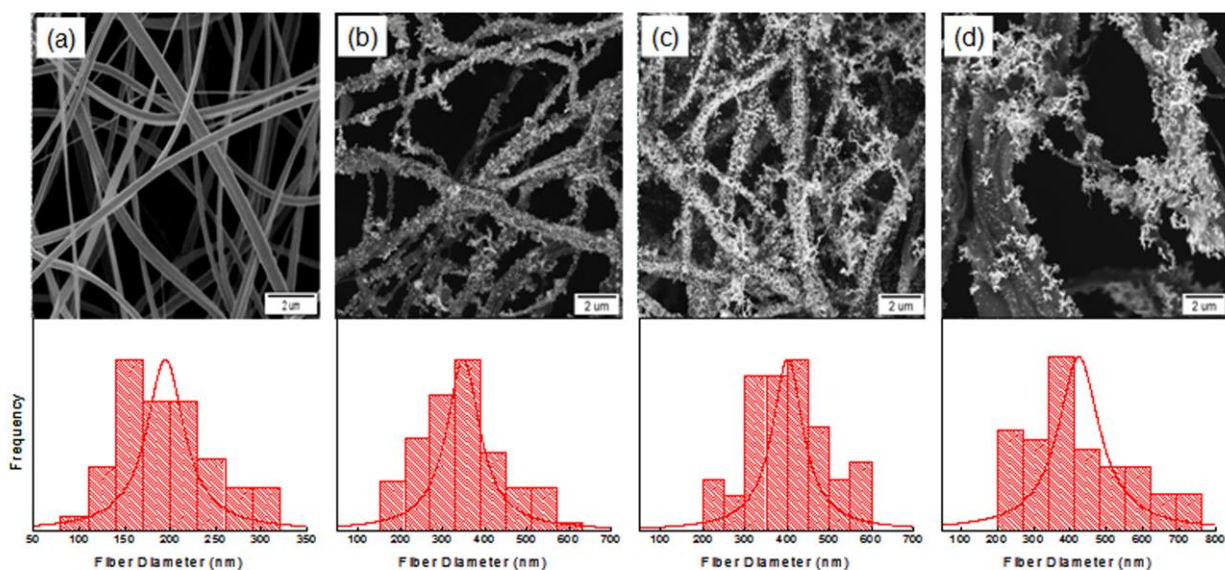
Figure 3.2.   SEM micrographs and fiber diameter distribution of (a) chitosan fibers and chitosan fiber-supported nZVI particles prepared in BH_4^-/Fe^{3+} ratio of (b) 1:1 (c) 2:1 (d) 3:1

Figure 3.2b-d indicates the formation of dispersed iron nanoparticles on the surface of the chitosan fibers at different amounts of BH_4^-. At the mole ratio of $BH_4^-:Fe^{3+}$ of 2:1, nZVI particles are seen to form on the fiber surface more homogeneously, with a higher density and increase in the fiber diameter compared to the mol ratio of 1:1. Further increase in reducing agent leads to aggregation of nZVI particles and results in separation of the particles from the fiber surface (Figure 3.2d).   The average fiber diameter of the composite fibers was determined to be 350 ± 95 nm, 400 ± 90 nm, and 425 ± 140 nm, respectively. The size of individual zerovalent iron nanoparticles ranged mainly between 75 and 100 nm, although some higher scale aggregates were also observed. Figure 3.3a shows STEM micrograph of the chitosan fiber-supported nZVI particles prepared in the presence of double amount of borohydride. Regularly shaped spherical nZVI particles appeared in dispersed form on the chitosan fibers. Typical EDX electron maps of the composite material in Figure 3.3b demonstrates the homogeneous distribution of C which forms the backbone of chitosan, while Figure 3.3c reveals the presence of iron in distinct domains on the chitosan surface.
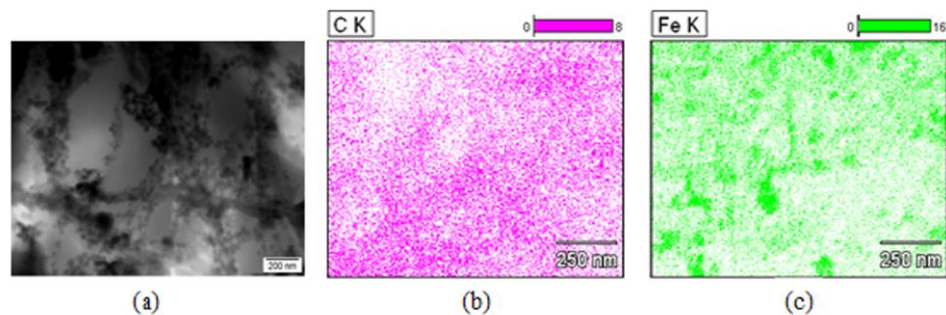
Figure 3.3. (a) STEM micrograph, and elemental EDX mapping images (K lines) of the surface of chitosan fiber-supported nZVI particles (b) C, and (c) Fe

Figure 3.4 displays the thermal decomposition profiles of the chitosan (curve a) and chitosan-nZVI composite fibers prepared at different BH_4^-/Fe^{3+} ratios. Curve b and c refer to 1:1 and 1:2, respectively. Both types of the fibers, regardless of the BH_4^-/Fe^{3+} mole ratio, exhibit three stages of decomposition. These are consecutive to the elimination of chemi/physisorbed water, degradation of 2-amino-2-deoxy-D-glucopyranose, and 2-acetamido-2-deoxy-D-glucopyranose units of chitosan (Nam et al. 2010). After heating beyond 250 °C, mass loss occurs sharply and the chitosan fibers seem to be decomposed completely at temperatures higher than 600 °C.
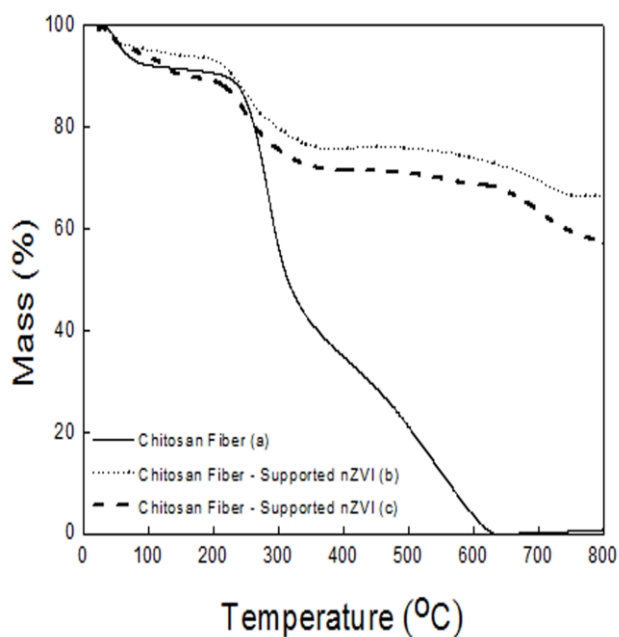
Figure 3.4. TGA curves of (a) chitosan fiber, and nZVI supported on chitosan nanofibers in BH_4^-/Fe^{3+} ratio of (b) 2:1 (c) 1:1

On the other hand, within the same temperature range, the composite fibers yield more than 60% of the initial mass. The remaining residue of the composite fibers can be attributed mainly to the iron based species developed on the fibers surface. Note that in comparison with the thermogram of neat chitosan fiber, the particles improve the thermal stability of chitosan-nZVI composite fibers approximately 30 °C particularly at early stage of the decomposition. Moreover, the composite fibers prepared with high BH_4^-/Fe^{3+} mole ratio yields higher amount of inorganic residual mass (67%) compared to the one prepared by the low ratio (57%). The higher residual mass can be attributed to the formation of higher number of Fe-based particles developed in the presence of higher amount of reducing agent (BH_4^-). This result seems to be in line with the electron microscopy micrographs (see Figure 3.2b and c).

The chitosan-nZVI samples were analyzed using XPS. The wide survey of the sample contained signals arising from the backbone of chitosan, namely C, N, and O, and signals that corresponded to iron (Figure 3.5). The iron signals are attributed mainly to the shell structure of nZVI, as the obtained signals in XPS arise from the upper few nm's of the surface. The insets in the figure correspond to Fe 2p and C 1s photoelectron profiles. The Fe $2p_{3/2}$ line appears to be centred at 711.2 eV binding energy which correspond to iron oxide. The shoulder that appears at 712.3 eV is very close to binding energy values reported earlier for iron oxohydroxide (FeOOH) (Wagner et al. 1979). The feature at 706.6 eV is close to the value reported for Fe in its zero oxidation state (Oku and Hirokawa 1979). This feature originates to the core region of the nanoparticles. The photoelectron profile of C 1s shows three distinct signals that are observed at 284.6, 286.2, and 289.0 eV. These features are attributed to three different C environments in chitosan structure, namely C-C, C-N, and C-O environments, respectively.
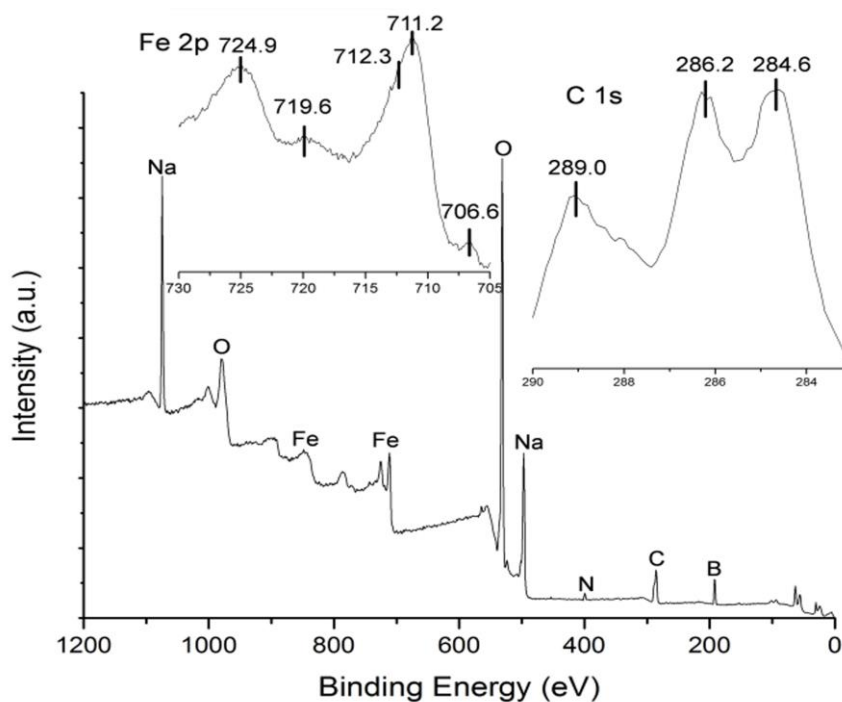
Figure 3.5. Wide XPS survey of the chitosan-nZVI fibers. The insets in the figure show Fe 2p and C 1s photoelectron profiles

The X-ray diffraction patterns of the chitosan-nZVI composite fibers before and after arsenic sorption are given in Figure 3.6. The crystalline structure of nZVI is characterized by the main reflection appearing at 2θ of 44.7° as shown in Figure 3.6a. The absence of chitosan signals in the XRD diagram can be referred to the fact that electrospun chitosan fibers have amorphous internal structure, as reported previously elsewhere (Horzum et al. 2010).
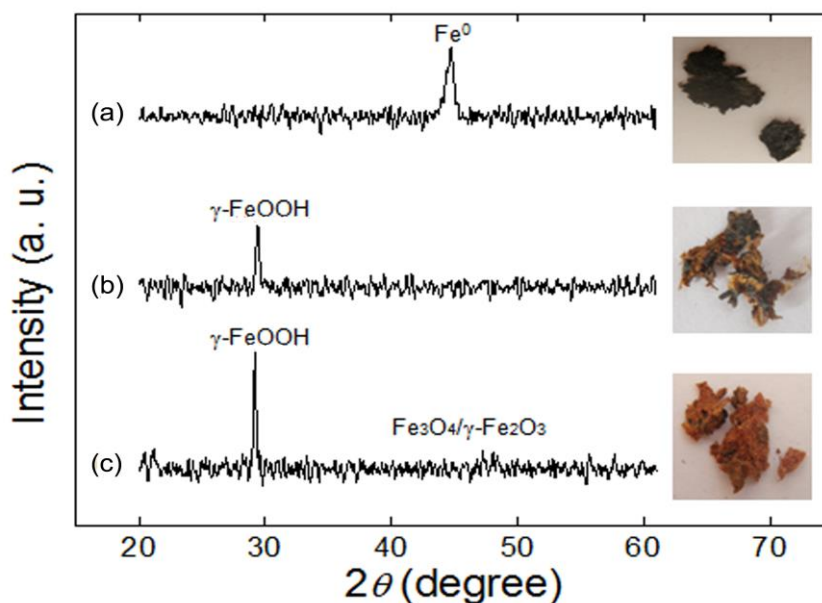
Figure 3.6. XRD patterns of the chitosan fiber-supported nZVI particles (a) before sorption (b) after As(V) sorption (c) after As(III) sorption

3.4.2. Material Properties after Sorption and Sorption Results

The XRD patterns of the fibers showed significant changes after sorption of aqueous arsenic ions. (Figure 3.6b and c) The signals of nZVI disappeared totally and the oxides appeared in the form of lepidocrocite (γ-FeOOH) and magnetite/maghemite (Fe_3O_4/γ-Fe_2O_3). The photographic images suggest that the freshly prepared chitosan-nZVI composite fiber (Figure 3.6a) is very dense and has black color. As shown in Fig. 3b and 3c, the fiber have turned brownish orange after As(V) sorption and orange after As(III) sorption, indicating that lepidocrocite and magnetite/maghemite particles were formed on the chitosan fiber surface due to the massive oxidation during the sorption process. The possible interactions between chitosan and nZVI particles, as well as the changes in the functional groups of chitosan-nZVI fibers after As(III) and As(V) sorption were identified by FTIR spectroscopy. Figure 3.7 presents the FTIR spectra of the chitosan-nZVI fibers as-prepared, and after sorption of As(III) and As(V), together with the spectrum of neat chitosan fibers. The spectrum of the neat chitosan fibers (green curve) shows characteristic bands centred at 3332 cm^{-1} (O–H stretching); 2920 and 2870 cm^{-1} (C–H stretching); 1651 cm^{-1} (C–N stretching in secondary amide); 1377 cm^{-1} (C–O stretching); 1073 cm^{-1} (N–H stretching). In the spectrum of the chitosan-nZVI fibers in Figure 3.7 (blue curve), some shifts on the characteristic bands were

47

observed depending upon the adsorption of nZVI particles on the chitosan surface. The stretching band of the hydroxyl groups at 3332 cm^{-1} in neat chitosan fibers are shifted to 3262 cm^{-1} in chitosan-nZVI fibers. On the other hand, there are shifts in the band corresponding to C-N stretching vibrations from 1651 to 1634 cm^{-1}, and also in the band of N-H stretching from 1073 to 1025 cm^{-1}. It is worth noting that the intensity of C–H, and C–O bands are significantly decreased in chitosan-nZVI fiber. The results clearly show that the interaction of nZVI with the O–H, C–N, and N–H groups of chitosan. Such phenomenon was already reported for Cu (Monteiro and Airoldi 1999), and Fe (Bhatia and Ravi 2003) metals, which were not only coordinated to NH$_2$, but also formed metal complexes with –OH groups.
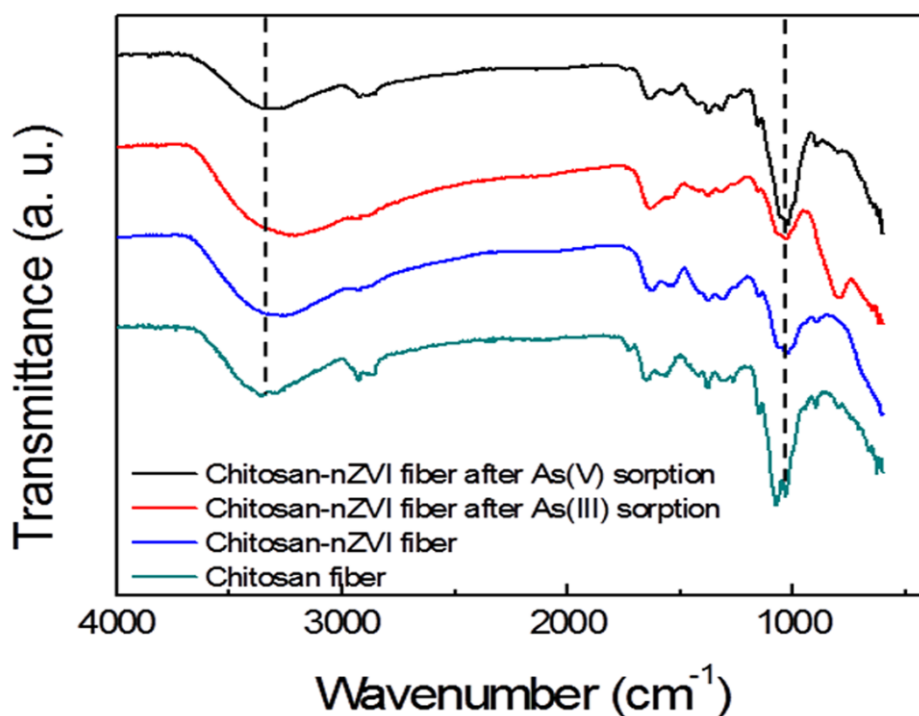
Figure 3.7. FTIR spectra of the chitosan-nZVI fibers as-prepared, after As(III), and As(V) sorption, compared with the spectrum of pure chitosan fibers

To gain further insight on the sorption mechanisms, the spectra of chitosan-nZVI fibers after As(III) (red curve) and As(V) (black curve) sorption are also investigated. The stretching band of the hydroxyl groups for chitosan-nZVI fiber after As(III) sorption is shifted to 3206 cm^{-1} accompanied by an increase in the intensity. In contrast, after As(V) sorption, a blue shift is observed in the hydroxyl band with a weaker intensity. Furthermore, the intensity of N–H stretching bands decreased in the chitosan-nZVI fiber after As(III) sorption, but increased in that of the sample after

As(V) sorption. The newly formed absorption band at 796 cm^{-1} may be attributed to the attachment of As(III) onto the chitosan-nZVI fibers.

The sorption experiments carried out to reveal the effect of initial concentration on the sorption of As(III) and As(V) on chitosan- nZVI composite fibers are presented in Figure 3.8. These experiments were performed in the concentration range of 0.01-25.0 mg L^{-1}, while the *V/M* ratio was fixed at 60 mL mg^{-1}. When the initial concentration was increased, a gradual decrease in percent sorption was observed. The data of As(III) and As(V) sorption on the chitosan-nZVI composite fiber mat were examined by Langmuir and Freundlich isotherm models, and the obtained isotherms are displayed in Figure 3.9.
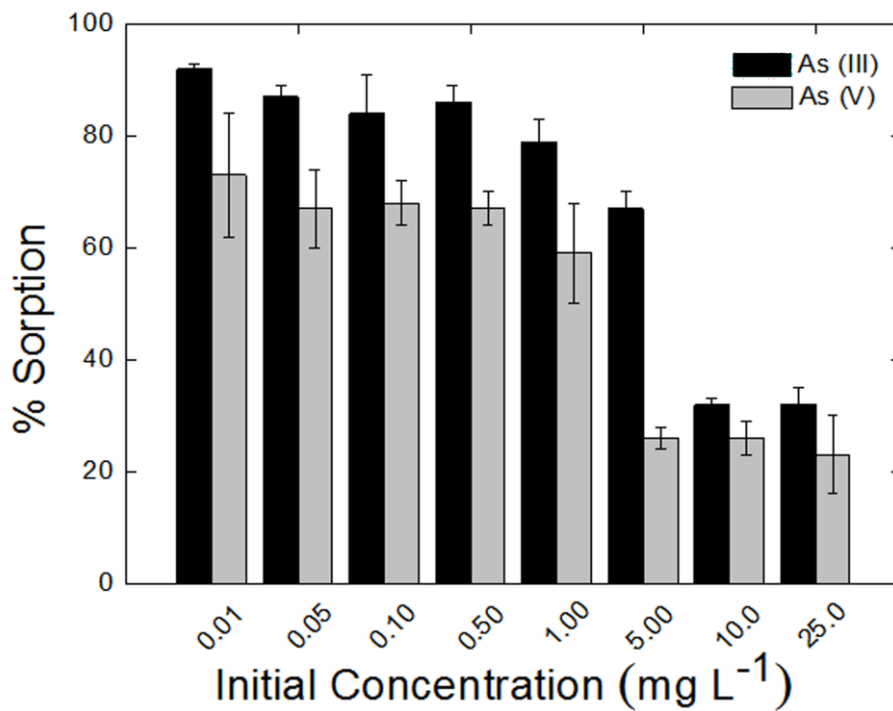
Figure 3.8. Variation of % uptake of As(III) and As(V) with the initial concentration

Langmuir theory assumes monolayer adsorption on a homogeneous surface. The non-linear form of Langmuir isotherm model is given by the equation:

$$q_e = q_{max} \frac{bC_e}{1+bC_e} \tag{3.3}$$

where q_e, is the amount of metal ions adsorbed onto the chitosan-nZVI composite fiber sorbent (mmol g^{-1}) at equilibrium, C_e (mmol L^{-1}) is the equilibrium concentration of metal ions in liquid phase, q_{max} (mmol g^{-1}) and b (L mmol^{-1}) are Langmuir constants related to the adsorption capacity and affinity, respectively.
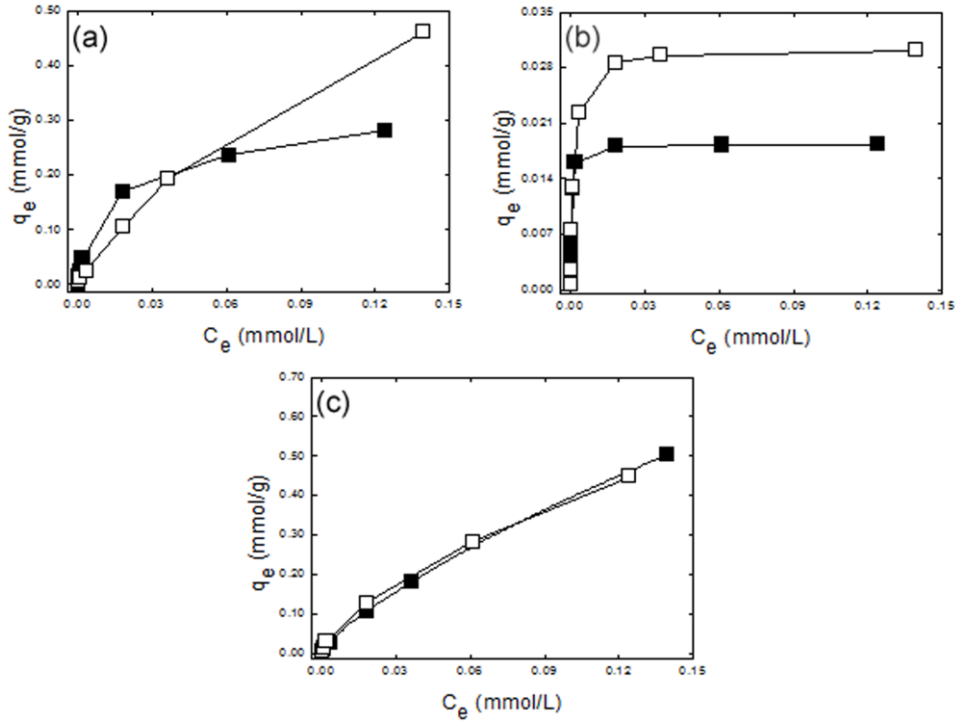
Figure 3.9. (a) Adsorption isotherm and non-linear fits of (b) Langmuir, (c) Freundlich models for (■)As(III) and (□) As(V) on the chitosan-nZVI composite fiber mat

The basic assumption of the Freundlich theory is that the adsorbent consists of a heterogeneous surface over a wide range of concentrations. Freundlich isotherm model is described by the equation:

$$q_e = K_F \, C_e^{1/n} \tag{3.3}$$

Here, K_F and n are the Freundlich constants for a given sorbent-sorbate system. The values of Langmuir and Freundlich constants were obtained from linear fits of the sorption data and are given in Table 3.2. Adequate linear correlations were observed for both Langmuir and Freundlich isotherm models. The adsorption capacities (q_{max}) of As(III) and As(V) for chitosan-nZVI composite fiber sorbent have been evaluated to be 0.0223 and 0.0305 mmol/g. The Langmuir constant, b, can be treated as an empirical

equilibrium constant, and used in the evaluation of the standard free energy of adsorption using the following equation;

$$\Delta G^\circ = -RT \, Inb \qquad\qquad (3.4)$$

The free energy of adsorption were found to be -19.99 kJ/mol for As(III) and -16.74 kJ/mol for As(V). The negative free energy values indicate that the adsorption reaction is driven far to the right, i.e. that products are much more favored over the reactants.

The value of Freundlich constant $(1/n)$ reflects sorption linearity, and it usually varies between 0 and 1. The corresponding values obtained from linear regression indicates that sorption is nonlinear, which is a typical behavior for surfaces with fixed and limited sorption capacities. The sorption of As(III) seems closer to linearity, which suggests higher extent of sorption. The K_F values show that the fiber sorbent possesses good affinity towards the adsorbate ions, with its affinity toward As(III) being relatively higher than As(V).

Table 3.2. Summary of model coefficients (Solution volume, shaking time, solution pH, sorbent amount and reaction temperature were 3.0 mL, 1 h, pH 6.0, 0.50 mg, and 25 °C, respectively, n = 3)

Adsorption model	Parameter	As(III)	As(V)
Langmuir	R^2	0.9888	0.9958
	Qmax (mmol/g)	0.0223	0.0305
	b (L/mmol)	3178.94	856.94
Freundlich	R^2	0.9950	0.9970
	K_F	9.5499	2.2542
	1/n	0.8323	0.7601

The effect of solution pH on the uptake of As(III) and As(V) ions on the chitosan-nZVI fibers is shown in Figure 3.10 at the initial concentration of 100.0 µg/L. In the case of As(III), chitosan-nZVI fiber sorbent shows higher than 80% removal at pH within 4.0-7.0. On the other hand, a significant decrease is observed in As(III) sorption beyond pH of 7.0. (Figure 3.10a) Similar trend of the pH dependence of As(III) sorption was also observed using nano scale zero-valent iron (Kanel et al. 2005). The underlying reason for the decrease in As(III) removal was explained by formation of its anionic specie that undergoes repulsion by the negatively charged sorbent surface. This is confirmed by the speciation analysis provided in the inset of Figure 3.10a which

reveals increase in formation of $H_2AsO_3^-$ in the alkaline conditions, accompanied with a decrease in the concentration of the H_3AsO_3 specie.
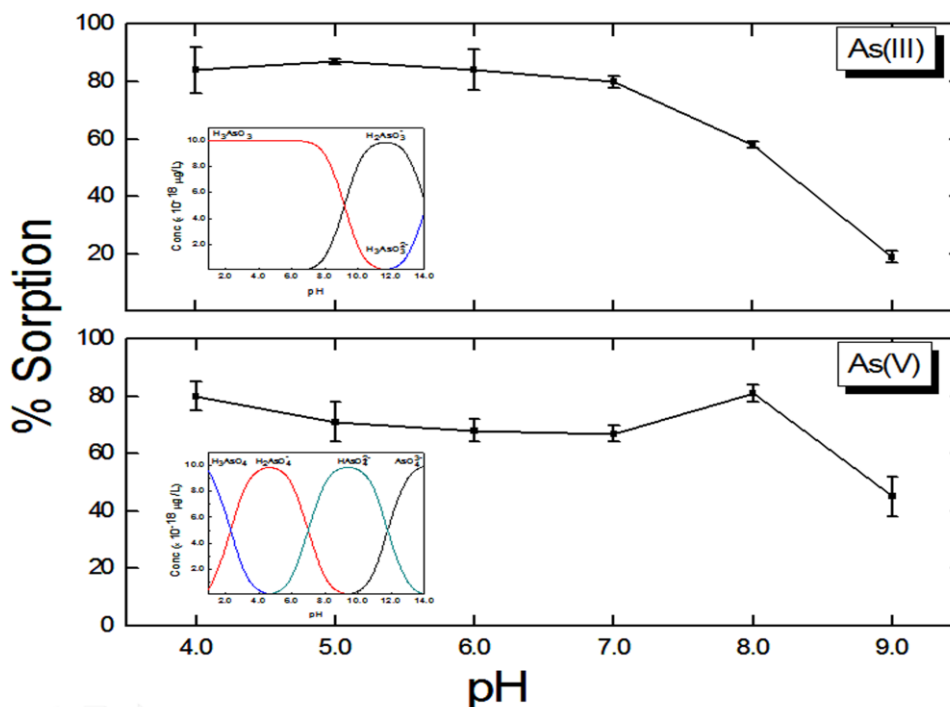
Figure 3.10. Effect of pH on the sorption of 100.0 μg L^{-1} (a) As(III), and (b) As(V) solutions by chitosan-nZVI fibers. The insets show speciation diagrams of As(III) and As(V)

It was reported that chitosan flakes do not show any affinity for As(III) over the wide range of pH values, whereas the same sorbent has highest As(V) sorption at pH 3.0 (Boyaci et al. 2010). However, at low pH values, the dissolution problem of chitosan precludes the possibility of its usage as a sorbent material for arsenic removal. As seen in Figure 3.10, pH trials for As(III) and As(V) sorption indicated that it is also possible to remove both species at neutral pH values using chitosan fiber-supported nZVI particles. The nature of As(V) sorption around pH 4-8, can be explained by coulombic interaction between chitosan-nZVI surfaces which exhibit positive charge at pH lower than the point of zero charge of 7.8 for nZVI (Kanel et al. 2005) and $H_2AsO_4^-/HAsO_4^{2-}$ ions which are the main species at the pH range.

It is worth noting that the fate of iron was taken into account while removing the arsenicals by using chitosan-nZVI fibers. Higher amount of dissolved iron was determined after As(V) sorption compared with the iron content after As(III) sorption.

The maximum iron concentration in solution after sorption process was 14 mg L^{-1}. It is estimated that the amount of dissolved iron is less than 0.7% of the initial nZVI amount assuming that the surface of chitosan is entirely coated with the particles.

Desorption experiments were performed in an analogous way to those with sorption experiments. The arsenic ion-loaded chitosan-nZVI fiber sorbents were individually treated with 0.5 M $MgCl_2$ or KH_2PO_4 for the release of arsenic ions. The desorption percentages for As(III) ions were 49% for KH_2PO_4, 40% for $MgCl_2$, and for As(V) ions were 36% for KH_2PO_4, 24% for $MgCl_2$. This indicates that the sorbed As(V) specie are more stable than those of As(III).
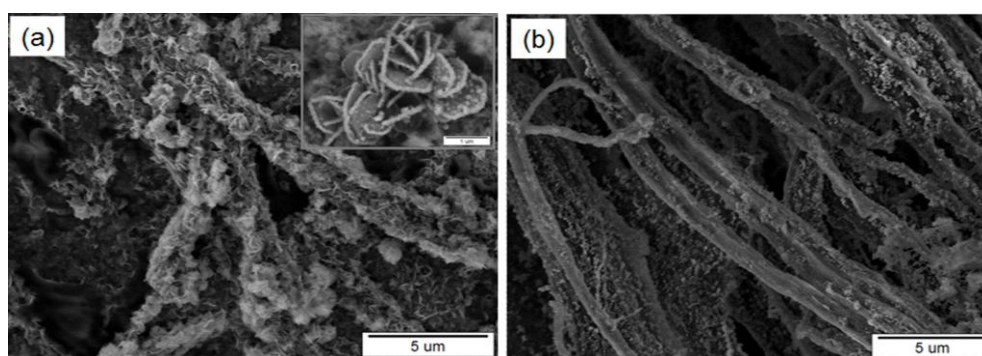
Figure 3.11. SEM micrographs of the chitosan-nZVI composite fiber after (a) As(III), and (b) As(V) sorption

SEM micrographs of dried chitosan-nZVI composite fibers after As (III) (Fig. 3.11a) and As (V) (Figure 3.11b) sorption studies showed a bundled fibrous structure along with lepidocrocite and/or magnetite/maghemite particles on the electrospun chitosan fibers. Agglomeration of iron oxides particles is also demonstrated by the figures. Distinctively, flower like structure on/between the fibers (Figure 3.11a, inset) has appeared after As (III) sorption.

The XPS features of Fe 2p before and after sorption of arsenic species are shown in Figure 3.12A. The oxidation of Fe is marked by the disappearance of Fe^0 feature that appears in curve a of Figure 3.12A around 707 eV. The oxidation leads to a shift in the Fe 2p peaks towards higher binding energies, indicating the development of iron oxyhydroxide groups on the surface. This is seen to be more pronounced in the case of As(V) sorption (curve c in Figure 3.12A), possibly leading to circumstances in which the ion is liable to complexation by oxyhydroxyl groups.

The O 1s profiles corresponding to the samples before and after sorption are

given in Figure 3.12B. The peak envelope centred around 531.0-531.3 eV showed relatively little changes, indicating that it belongs to structural O in the composite materials.
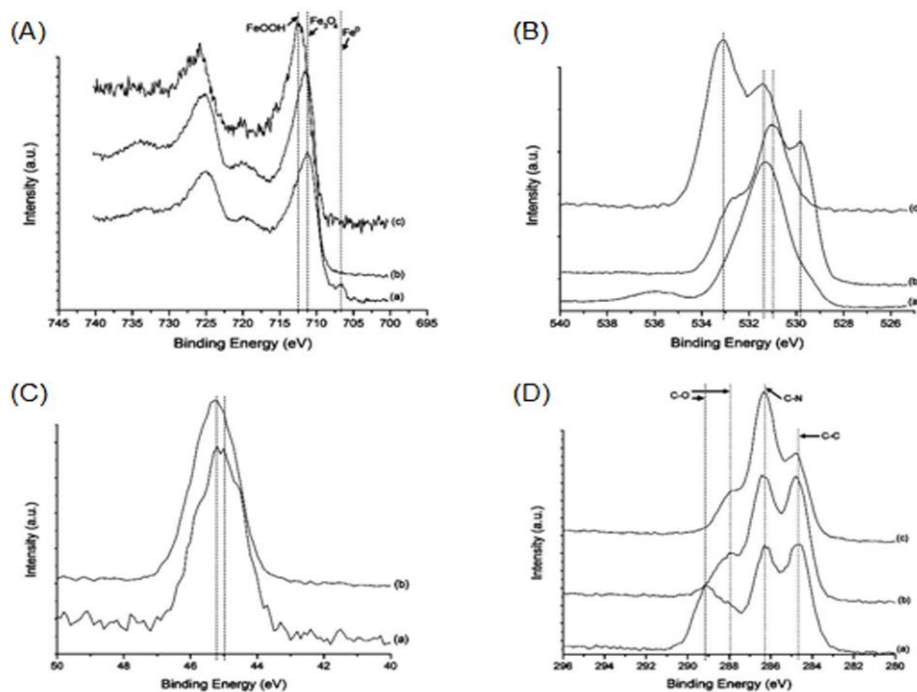
Figure 3.12. XPS profiles of the composite fibers showing (A) Fe 2p, (B) O 1s, (C) As 3d, (D) C 1s features before and after sorption process. In Figs. A, B, D; (a) represents the samples before sorption, (b) refers the samples after sorption of As(III), and (c) the samples after sorption of As(V). In Fig. C, (a) stands for As(III) signal and (b) stands for As(V) signal

The variety of chemical environments in which O exists in the composite materials makes it no easy to provide an accurate assignment for these envelopes of peaks. Nevertheless, it is possible to mention that these features display binding energies close to those assigned earlier for O^{2-} in the hydroxyl groups of α-FeOOH (goethite) and γ-FeOOH (lepidocrocite) reported at 531.0 eV and 531.1 eV, respectively.(Grosvenor et al. 2004) The sorption of As(III) leads to the development of an O 1s feature centred at 529.8 eV and a shoulder centred at 533.1 eV (curve b in Figure 3.12B). The former one (529.8 eV) is close to those assigned previously to O^{2-} in α-Fe_2O_3 (hematite) and that in γ-Fe_2O_3 (maghemite), reported at 530.0 eV and 529.9 eV, respectively,(Grosvenor et al. 2004) and could reflect the extensive oxidation of iron accompanying sorption. The latter feature at 533.1 eV is tentatively thought to

belong to the O in the sorbed arsenic species. This feature becomes more distinct when As(V) is sorbed (curve c in Figure 3.12B). Given that As(III) is largely oxidized to As(V) upon sorption, as discussed in next section, and the fact that O 1s level bonded to As(V) would experience a decrease in electron density, it seems logical to assign this feature to sorbed arsenate species.

3.4.3. Sorption Mechanism

The sorption mechanism of As specie by nZVI was addressed in several studies, and seems not to be totally resolved yet. Earlier studies reported that As(III) undergoes fast sorption on nZVI surface, and as time passes, As(III) near or in contact with the corroding nZVI surface may be oxidized to As(V), which subsequently is sorbed by an inner-sphere mechanism (Kanel et al. 2005). In a study of As(V) sorption on nZVI, it was confirmed that As(V) is fixed through an inner-sphere surface complexation.(Kanel et al. 2006) The same study indicated that until 60 days, only As(V) was detected, but on a longer time scale As(III) was identified due to the reduction of As(V).

In later studies, it was shown that As(III) undergoes both oxidation and reduction at nZVI particle surfaces (Ramos et al. 2009). Oxidation was reported to yield As(V), while reduction lead to formation of As(0). This was confirmed in another study in which it was stated that As(V), formed via oxidation of As(III), was fixed predominantly by outer surface of the oxide shell of nZVI surface, while reduced species were enriched in a subsurface layer close to the Fe(0) core (Yan et al. 2010). Recently, it was reported, based on analysis using the structural techniques − X-ray absorption spectroscopy (XAS) and X-ray absorption near-edge spectroscopy (XANES) − that for nZVI in anoxic As(III) solutions, As(III) species sorbed on nZVI surface undergoes diffusion across the thin oxide layer enclosing the nanoparticles, which results in arsenic forming an intermetallic phase with the Fe(0) core (Yan et al. 2012). The same study reported that As(V), presumably resulting from As(III), could not be detected, and attributed its detection in other studies to alteration of surface chemistry of nZVI during XPS analysis.

The XPS profiles obtained in this study for the sorption of As(III) and As(V) are shown in Figure 3.12C. The XPS profile of As 3d resulting from the sorption of As(V) seems to be centred at 45.2 eV (curve b in Figure 3.12C). Similarly, the profile of As 3d

resulting from the sorption of As(III) is slightly split to two peaks centred at 45.2 eV and 45.0 eV (curve a in Figure 3.12C). Based on this, it seems that, while As(V) retains its oxidation state upon fixation by nZVI surface, As(III) undergoes oxidation to As(V). The split might suggest the formation of two types of surface complexes of As(V). The absence of a signal at 43.5 eV indicates that As(III) is totally oxidized. Moreover, no signal of As(0) was observed in both cases, suggesting that reduction is not involved in the mechanism. These results should be viewed within the context of conditions applied in this study. The formation of As(0) was well documented before as one of the options of the fixation mechanisms for both of As(III) and As(V) on nZVI.(Ramos et al. 2009) However, the same study mentioned that arsenic concentration and solution pH, and the properties of iron materials play crucial roles in determining the final arsenic speciation.

The contribution of chitosan component in the composite material to the uptake of As ions cannot be ruled out. This has been well documented in literature,(Pontoni and Fabbricino 2012) and is obvious from the changes observed in the relative intensities of C 1s components in the XPS spectrum. It is important to mention that the fixation of As(III) and As(V) resulted in a great decrease in the intensity and shift in the binding energy of C 1s feature corresponding to C-O environment (Figure 3.12D), possibly indicating that the hydroxyl groups of chitosan form more attractive centers for arsenite and arsenate complexation. In both cases, no important change in the C 1s feature corresponding to C-N environment is observed. It could be useful to note also that the sorption of As(V) lead to a large decrease in the C 1s intensity corresponding C-C environment, possibly suggesting partial disruption of these bonds in chitosan structure upon sorption of As(V) species. As revealed by the speciation analysis mentioned above, within the pH conditions used of this study, the major forms of As(III) are expected to be $H_3AsO_3/H_2AsO_3^-$, while the major forms of As(V) are $H_2AsO_4^-/HAsO_4^{2-}$, hence the mode of interaction between these specie and the protonated hydroxyl groups on chitosan surface would be dominated by electrostatic attraction. Due to its neutral H_3AsO_3 form, the extent of sorption of As(III) by chitosan component is expected to be smaller than that of As(V).

3.5. Conclusion

Chitosan fiber-supported nZVI particles were synthesized and then used in the removal of inorganic arsenic species from aqueous systems. High sorption capacity and stable performance of the chitosan-nZVI fibers were achieved over a wide range of pH. The fiber sorbent showed higher affinity toward As(III) compared to As(V), and the sorption behavior was adequately described using both Langmuir and Freundlich isotherms. Spectroscopic investigation showed that the arsenic ions seem to be fixed to oxide and oxyhydroxide groups at the outer shells of nZVI surfaces. While As(V) retains its oxidation state upon fixation by nZVI, As(III) undergoes oxidation to As(V). Moreover, chitosan seems to contribute to arsenite and arsenate complexation mainly via its hydroxyl groups.

The ease of preparation of chitosan fiber-supported nZVI particles can offer a very convenient way for the development of sorption-enhanced materials to use in the removal of undesirable metal ions from water.

CHAPTER 4

SYNTHESIS OF AMIDOXIMATED POLYACRYLONITRILE FIBERS AND ITS APPLICATION FOR SORPTION OF AQUEOUS URANYL IONS UNDER CONTINUOUS FLOW

4.1. Abstract

This study reports a feasible method for the removal of radioactive U(VI) ions from aqueous systems via column sorption under continuous flow. Electrospun polyacrylonitrile (PAN) fibers were used as sorbent materials in a home-made minicolumn. The nitrile groups on the fibers' surface were modified to amidoxime groups using hydroxylamine hydrochloride. Surface modification was observed to enhance the sorption capacity of PAN fibers toward uranium ions by more than 4 folds, by virtue of the chelating ability of amidoxime groups. The experiments investigated the effect of pH, initial concentration, and repetitive loading on the sorption properties of amidoximated-PAN fibers. Based on the overall results, the surface-modified fibers seem as a suitable potential sorbent material for the applications in environmental cleanup particularly nearby nuclear plants.

4.2. Introduction

Uranium is the heaviest naturally occurring radionuclide that has various harmful fouling in the environment. There are hundreds of uranium species that accounts for 5% of all known minerals (Kalin et al. 2005). This element is present in most of rocks, soil, surface and groundwater in the order of a few parts per million. It is also discharged into the environment from many anthropogenic activites such as mining, military applications, production and use of phosphate fertilizers, combustion from coal and other fuels, and nuclear power facilities. The increasing usage of nuclear reactors for large scale energy production leads to radioactive contamination, hence

research concerning the separation of U(VI) ions from waters has been a critical environmental issue in the last decade (Mun et al. 2007, Pekel and Guven 2003, Sadeghi et al. 2012).

There are two commonly used ways to remove U(VI) ions from solutions: i) sequestration using organic compounds ii) fixation on surfaces of sorbent materials. The former involves the covalent interaction of uranyl ions with specific organic compounds until the ions are not radioactive anymore (Arnold et al. 2012). However, this requires reconsideration as radioactivity cannot be eliminated by chemical bonding. In the latter, the ions are fixed onto the surface of a heterogeneous material through sorption. While the concentration of uranyl ions decreases in solution, it is enriched on the surface of the sorbent material.

The sorption of U(VI) ions can be achieved by various forms of natural and synthetic adsorbents given in Table 4.1. Several works related to uranium sorption onto naturally occuring clay minerals and soil fractions have been performed. Hudson et al. (Hudson et al. 1999) examined vermiculate and hydrobiotite, and Sylwester et al. (Sylwester et al. 2000) examined silica, alumina and montmorillonite as sorbents. They both investigated the pH dependence of uranyl oxo-cation (UO_2^{2+}) sorption and determined the local structure around the sorbed uranium atom. Fouchard et al. (Kowal-Fouchard et al. 2004) illuminated the surface complexation of the uranyl ions and montmorillonite sorption sites. Kilincarslan and Akyil (Kilincarslan and Akyil 2005) studied uranium sorption on clinoptilolite zeolit surfaces and determined the optimum conditions such as pH, initial concentration, contact time and temperature. The sorption behavior of uranium on sodium aluminosilicate solid phases was investigated by Mensah et al. (Addai-Mensah et al. 2005). Greathouse and Cygan (Greathouse and Cygan 2006) concluded that siloxane groups of beidellite, montmorillonite, and pyrophyllite were responsible for uranyl sorption. Donat et al. (Donat et al. 2009) combined biomass and clay mineral to prepare *Ulva* sp.-sepiolite composite sorbent and Khani (Khani 2011) carried out optimization of uranium removal by *Padina* sp. algae biosorbent.

To improve the sorption capacity of sorbents, many attempts have been made on chemical modification of sorbent surfaces using functional groups such as amidoxime (Pekel and Guven 2003, Saeed et al. 2008, Takeda et al. 1991), imidazole (Pekel et al. 2000), and metal oxides (Zou et al. 2009, Sadeghi et al. 2012, Comarmond et al. 2011), which possess chelating abilities towards U(VI) ions. As commonly used sorbents are in

powder form, their utilization as a filter material is not convenient due to the difficulty in the isolation of the solid from solution medium following the sorption stage.

Table 4.1. Summary of sorption system suggested for uranium

Sorbents	Size	Types of Sorption	Reference
Streptomyces and *chlorella* cells	-	Column	(Nakajima et al. 1982)
Polyethylene hollow fiber	380 μm	Column	(Takeda et al. 1991)
Montmorillonite	< 2 μm	Batch	(Greathouse and Cygan 2006, Kowal-Fouchard et al. 2004, McKinley et al. 1995, Sylwester et al. 2000)
Vermiculite and hydrobiotite	< 45 μm	Batch	(Hudson et al. 1999)
Silica, alumina	0.48 μm	Batch	(Addai-Mensah et al. 2005, Sylwester et al. 2000)
Amidoximated poly(acrylonitrile/N-vinylimidazole)	4-5 mm in length	Batch	(Pekel and Guven 2003)
Clinoptilolite zeolite	< 74 μm	Batch	(Kilincarslan and Akyil 2005)
Hydrogels based on PEG and methacrylic acid	-	Batch	(Mun et al. 2007)
Ulva sp.-Sepiolite	<125 μm	Batch	(Donat et al. 2009)
Manganese oxide coated zeolite	60-200 μm	Column	(Zou et al. 2009)
Manganese oxide coated sand	670-990 μm	Batch	(Zou, Zhao, et al. 2011)
Padina sp. algae biomass	1.0-1.25 mm	Batch	(Khani 2011)
Titanium dioxide	4-240 nm	Batch	(Comarmond et al. 2011)
Iron oxide	<15 nm	Batch	(Sadeghi et al. 2012)

Therefore, additional treatments might be needed such as coating of these sorbents onto a supporting surface to efficiently use them for uranium removal. Zou et al. (Zou, Bai, et al. 2011) modified the natural zeolite surfaces using manganese oxide and tested uranium(VI) sorption performance by fixed bed ion-exchange column. The same authors reported the usage of manganese oxide coated sand as a sorbent for the removal of uranyl ions in batch process. Recent attention is paid to amidoxime chelating adsorbent in removing heavy toxic metals and/or selective-recovering of precious metals. Takeda et al. (Takeda et al. 1991) proposed fixed bed adsorption unit containing amidoxime-modified commercial polyethylene hollow fiber for the recovery

of uranium from seawater. Pekel and Guven (Pekel and Guven 2003) studied uranyl ions uptake by amidoximated poly(acrylonitrile/N-vinylimidazole) complexing sorbents. It was reported that uranyl ions adsorption was achieved via the complexation abilities of vinylimidazole and amidoxime groups. However, colloidal hydrogels as filter medium are not favorable for their lack of mechanical integrity accompanied with difficulty in the separation of the solid phase from aqueous medium.

Electrospun fibrous materials are emerging as suitable alternatives to conventional sorbents due to their structural advantages conveyed by the nanosized diameter of the constituent fibers (Demir et al. 2002, Desai et al. 2009, Haider and Park 2009, Klimov et al. 2010, Ren et al. 2012, Saeed et al. 2008, Si et al. 2012). The high surface area to volume ratio which leads to high sorption capacity, porosity and mechanical integrity are the benefits of electrospun fibers. The fibers also serve as substrates for functional groups upon surface modification (Agarwal et al. 2010, Dong et al. 2006). They can thus be potentially used for sorption and desorption of metal ions. Based on this, it seems reasonable to investigate the sorption efficiency of amidoxime modified electrospun fiber for the removal of radioactive and chemically toxic U(VI) ions from aqueous systems. The surface-modified electrospun fibers used in this work enjoy large surface area and porosity as well as mechanical integrity which are desirable properties in filtration applications. This makes such fibers superior in terms of sorption capability over many of powdered sorbents and colloidal hydrogels reported in earlier works. The sorption study described herein was designed to survey the characteristics of amidoximated- PAN fiber and to test their properties as a sorbent for U(VI) ions from synthetic solutions via a column system. Column-type continuous-flow sorption has an advantage over batch type sorption as the rate of sorption depends on the concentration of solute in the solution being treated. In column treatment, the filter material is continuously in contact with a fresh solution. By virtue of column sorption, the concentration in the solution changes very slowly, however in batch sorption, the concentration of the solute decreases much more rapidly and thereby reduces the effectiveness of the sorbent. Compared to batch sorption, column sorption is more convenient in industrial applications due to its simplicity, not requiring any additional processes such as filtration and centrifugation, and providing higher residence time. Many applications of filtering processes involve the removal of undesirable species under continuous flow of the solution. For example, in agriculture irrigation pipes, the filtering material is placed on cross section of the pipes such that it is normal to the flux

direction of solution, and as such the mechanical resistance to continuous flow becomes the main requirement for filtering material. Electrospun fiber mat, in this sense can be a promising candidate for such applications (Horzum et al. 2010).

4.3. Experimental Section

4.3.1. Materials

Acrylonitrile (AN) and benzoyl peroxide (BPO) were provided from Fluka Chemical Company. For the surface modification of PAN fibers, hydroxylamine hdyrochloride ($H_3NO\cdot HCl$) and sodium hydroxide (NaOH) were supplied from Sigma-Aldrich and Riedel-de Haen Chemicals, respectively. N,N-dimethylformamide (DMF) (Sigma-Aldrich) was used as electrospinning solvent and uranylacetate dihydrate ($UO_2(CH_3COO)_2\cdot 2H_2O$) (Merck's Reagenzien) was used as sorbate. Sodium bicarbonate ($NaHCO_3$) (Fluka), ammonium citrate ($C_6H_{17}N_3O_7$) (Sigma), ethylenediamminetetraacetic acid ($C_{10}H_{16}N_2O_8$) (Riedel-de Haen) were used as desorbing eluents. All the chemicals were of reagent grade and ultrapure water (18.2 MΩ cm) was used throughout the study.

4.3.2. Instrumentation and Software

Electrospun fibers were analyzed by scanning electron microscope (SEM) (Philips XL-30S FEG, Eindhoven, The Netherlands). ImageJ 1.43u software was used for the determination of fiber diameter from SEM micrographs. At each trial, 100 test fibers were measured in each trial, and the average fiber diameter (AFD) and its standard deviation were determined. Energy Dispersive X-ray (EDX) analysis was performed using FEI XL30 W instrument equipped with Apollo X Silicon Drift detector. Atomic distribution of the surface of the sorbents was obtained from randomly selected points.

The amidoximation reaction and uranyl sorption were investigated via Fourier Transform Infrared Radiation (FT-IR) spectroscopy. FT-IR measurements of the samples before and after the amidoximation reaction as well as uranyl sorbed-fibers were performed by Perkin Elmer Spectrum 100 FTIR Spectrometer (Shelton, USA)

with Pike Miracle Single Reflection Horizontal ATR Accessory. The amount of uranium ions was determined using an inductively coupled plasma (ICP) spectrometer (Agilent 7500ce Series, Japan). The ICP-MS operation parameters are given in Table 4.2. Standard solutions in 5.0, 10.0, 25.0, 50.0, 100.0, 200.0, 500.0, and 1000.0 μg L^{-1} concentrations were prepared by appropriate dilution of 10.0 mg L^{-1} of stock U(VI) solution to the required volume. All samples and standard solutions were acidified through the addition of proper amount of concentrated HNO$_3$ to produce 1.0% (v/v) acid in the final solution. The percentage of uranium sorption was calculated using Equation 4.1, where C_i is the initial and C_f is the final concentration in the solution.

$$\% Sorption = \frac{C_i - C_f}{C_i} \times 100 \tag{4.1}$$

The speciation analysis of uranium-containing ions at various pH values was performed using Visual Minteq software.

Table 4.2. ICP-MS operation parameters

Operation Parameters	Value
RF power	1550 W
Make up gas flow rate	0.1 L min^{-1}
Argon carrier gas flow rate	0.9 L min^{-1}
Octopole collision gas flow rate	4.5 mL min^{-1}
Chamber temperature	2 °C
Sample depth	7.8 mm
Nebulizer	Concentric
Nebulizer pump	0.1 rps
Tune setting (m/z)	7/89/205
Isotopes monitored (m/z)	^{238}U

4.3.3. Polymerization of Acrylonitrile

Polymerization of acrylonitrile was carried out at 60 °C using benzoyl peroxide as an initiator. AN (0.076 mol) and BPO (0.0076 mol) were mixed in a sealed glass tube and after sonication for 15 min. Three cycles of a freeze-thaw process were applied prior to polymerization. The glass tube containing the AN and BPO were placed into a preheated bath at 60 °C; the polymerization was performed under an N_2 atmosphere, and it was stopped after the desired time by quenching to room temperature. The resulting product were dissolved in DMF and purified in methanol under continuous mixing along 3 hours, then filtrated in vacuum. After filtration, the polyacrylonitrile were dried under vacuum for 6 hours at 40 °C.

The viscosity average molecular weight of the synthesized polymer was determined by using a petrotest capillary viscosimeter (Dahlewitz, Germany) placed in a water bath thermostatically controlled at 25 °C. The polymerization products were dissolved in DMF at concentrations ranging from 1.3 g L^{-1} to 3.9 g L^{-1}. Calculations were made using the Mark-Houwink equation $[\eta] = KM_v^{\alpha}$, where K and α are the specific constants for a given polymer which vary for the used solvent system and temperature (Seferis 1999). K and α of PAN are equal to 0.21 cm^3 g^{-1} and 2.20, respectively. The polymer used in the experiment has viscosity molecular weight (M_v) in the range of 180 kg mol^{-1}.

400 MHz NMR (Varian VnmrJ, Palo Alto, USA) was employed to determine the number average molecular weight (M_n) of the polymer and it was calculated as 14 kg mol^{-1}. The ratio of protons on the end-groups to the protons on the polymer backbone was determined by integration of ^{1}H NMR signals.

4.3.4. Electrospinning of Polyacrylonitrile

The electrospinning solution of the synthesized PAN was prepared by dissolving the polymer (4 wt%) in DMF. The PAN solution was placed in a 20 mL syringe fitted with a metallic needle of 0.2 mm of inner diameter. The syringe was fixed horizontally on the microinfusion pump (LION WZ-50C6) and the electrode of the high voltage power supply (Gamma High Voltage Research Ormond Beach, FL, US) was attached to the metal needle tip. The flow rate of the polymer solution was 2 mL h^{-1}, the voltage of

15 kV was applied to the needle and the distance between the needle and the collector was 5 cm. The electrospinning process was performed at room temperature and the resulting fiber mat was held in vacuum at 50 °C overnight to remove any residual solvent.

4.3.5. Surface Treatment of PAN Fibers

The hydrophilic character of the electrospun PAN fiber was increased by converting the nitrile groups of AN to amidoxime groups. For the amidoximation reaction, a recipe given in the literature was followed (Sahiner et al. 1999). Hydroxylamine hydrochloride (0.375 g), sodium hydroxide (0.375 g), and 25.0 mg of PAN nanofiber mats were added to a 50 mL beaker and continuously stirred for 2 days at RT. After surface reaction, the nanofiber mats were washed several times with distilled water to remove the remaining salts, and dried in a vacuum oven at 60 °C.

4.3.6. Sorption Studies

Aqueous U(VI) solutions were prepared by dissolving proper amount of $(UO_2(CH_3COO)_2 \cdot 2H_2O)$ in ultrapure water. Column studies were carried out in order to show the applicability of amidoximated-PAN fiber sorbent in the continuous removal of uranyl from aqueous solution. A home-made microcolumn system involving Teflon tubing with internal diameter of 1.5 mm and 50 mm of height was employed in the experiments. The 30 mm height of tubing was filled with amidoximated-PAN fiber sorbents. Cylindrically shaped small sponge pieces were squeezed into both ends of the tube such that amidoximated-PAN fibers were sandwiched and the back-pressure of the continuous flow was prevented. The schematic representation of the experimental setup of column study is illustrated in Figure 4.1. The U(VI) solution flowed downward flow at a flow rate of 0.15 mL min^{-1} using a peristaltic pump. The samples of effluent were collected regularly at 3 mL volume fractions at different initial concentrations and solution pH values.

The effect of pH on the extent of sorption was conducted after adjusting the initial pH's of the solutions to 3.0, 4.0, and 8.0 using 0.01 M, 0.1 M, 1.0 M of HNO_3 and NH_3 solutions. In each experiment 45.0 mL of U (VI) solution was circulated.

The experiments investigating the effect of initial concentration was performed at 5.0, 10.0, 50.0, and 100.0 µg g^{-1} concentrations. In each study 3.0 mL of U(VI) solution (adjusted to pH of 4.0) was circulated.
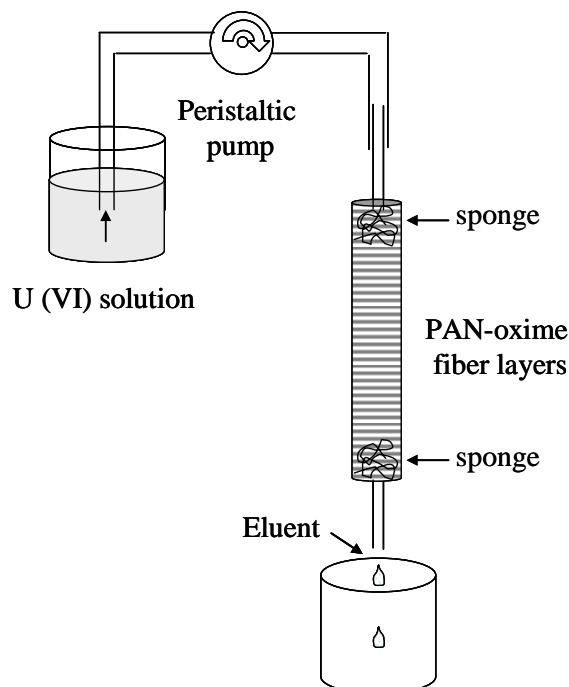
Figure 4.1. Schematic representation of experimental setup of column experiment

In order to study the effect of repetitive loading, a series of experiments were carried out. In each experiments 3 mL aliquots of fresh U(VI) solutions having initial concentrations of 50.0, and 100.0 µg g^{-1} was loaded for 14 times. The experiments were further continued using 100.0 µg g^{-1} solution and the sorbent was exposed to eighty successive doses of 3.0 mL solutions.

For desorption experiments, the uranyl ion loaded sorbent was treated with 3.0 mL aliquots of 0.5 M NaHCO$_3$, 0.5 M C$_6$H$_{17}$N$_3$O$_7$, and 0.1 M EDTA. Consecutive sorption-desorption cyles were performed to study the reusability of the amidoximated-PAN fiber sorbent. The eluted solutions were then analyzed for possibly sorbed and released U(VI) ions.

4.4. Results and Discussion

The main aim of this work was to design a sorbent material as well as an easily practicable column system to remove contaminating uranium(VI) ions from aqueous solutions. For this aim, we prepared submicron-diameter polyacrylonitrile (PAN) fibers using electrospinning method. The surface of the fibers was modified by amidoxime groups and the sorption ability of the both modified and unmodified fibers was studied.

4.4.1. Fabrication of PAN Fibers

PAN was synthesized through free radical bulk polymerization at 60 °C using BPO as an initiator. Figure 4.2 shows NMR spectra of acrylonitrile and polyacrylonitrile. The number average and viscosity molecular weights are 14 and 180 kg mol^{-1}, respectively. PAN fibers were obtained through electrospinning of PAN/DMF solution at different concentrations. The concentration was fixed to 4 wt% in terms of solid content. A series of trials were carried out to obtain bead free and uniform morphology at different potential differences and flow rates. The electrospinning process (the fiber fabrication) was optimized at 3 kV cm^{-1} potential difference and 2 mL h^{-1} flow rate.
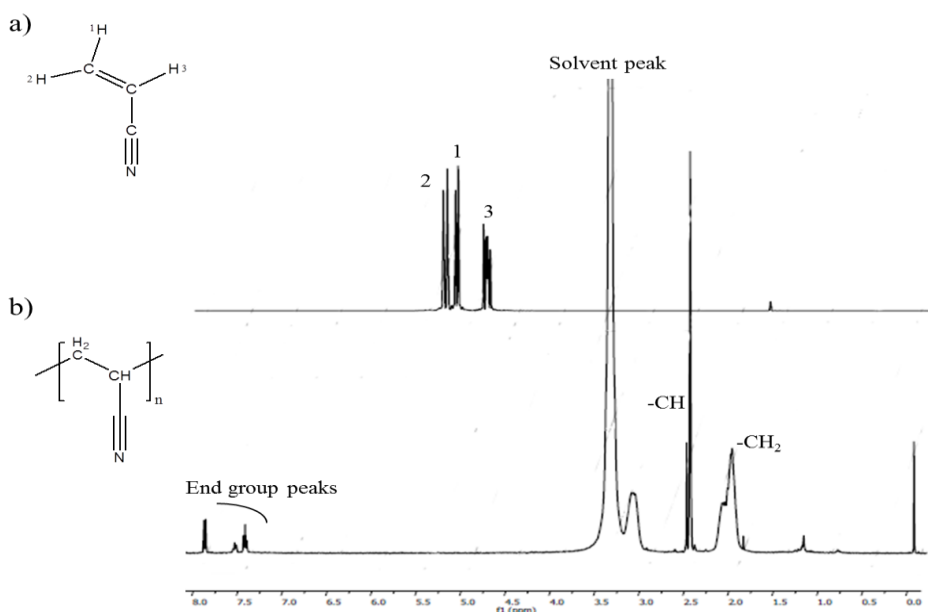
Figure 4.2. ^{1}H NMR spectra of acrylonitrile (AN) monomer and poly(acrylonitrile) (PAN) polymer in CDCl$_3$

4.4.2. Surface Treatment of PAN Fibers

The surface modification of PAN fibers was performed by a wet chemical process. Figure 4.3 shows the proposed reaction mechanism of hydroxylamine hydrochloride with PAN nitrile group in a neutralized medium. The nitrile groups on the surface of PAN fibers react with H_2NOH at room temperature. The hydroxylamine undergoes nucleophilic addition to the fibers surface and a subsequent arrangement to carboximidamide. Eventually, the surface of the fibers is functionalized for chelating uranyl cations. The conversion of nitrile group in PAN into amidoxime group (C_n) was estimated using the following equation (Lin et al. 1993).

$$C_n = \frac{W_1 - W_0}{W_0} \; x \; \frac{M_0}{M_1} \; x \; 100 \tag{4.2}$$

Here, W_0 and W_1 are the weights of the PAN nanofiber mat before and after amidoximation reaction, respectively. M_1 is the molecular weight of hydroxylamine (33 g mol^{-1}) and M_0 is the molecular weight of acrylonitrile repeat unit (53 g mol^{-1}). Conversion of the nitrile group in polyacrylonitrile into amidoxime group was calculated as 30%. The resulting fibers were soft and light yellow and this observation is compatible with previously reported results (Saeed et al. 2008).
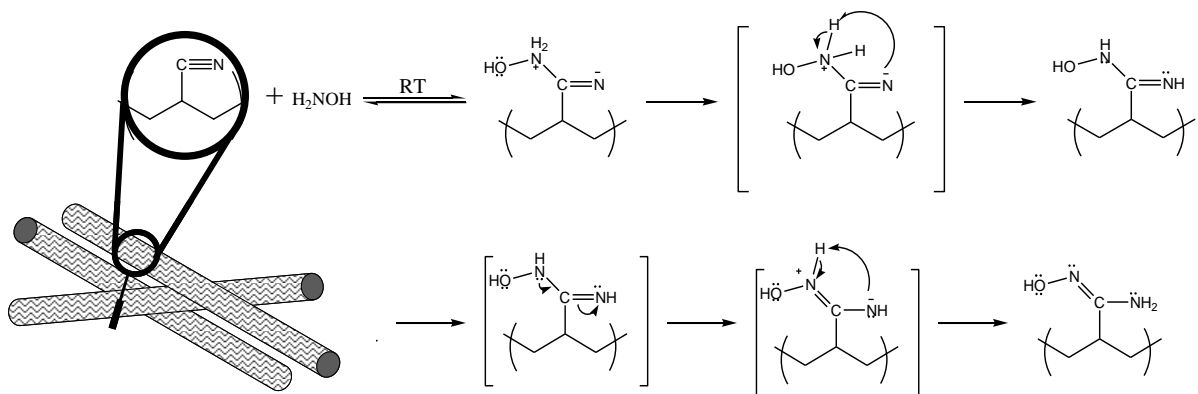
Figure 4.3. The conversion of nitrile groups to amidoxime groups in PAN fiber

Figure 4.4 shows FTIR spectra of PAN fiber and amidoximated-PAN fiber as well as the fiber after sorption of uranyl ions. A characteristic band of nitrile groups at 2260 cm^{-1} is present on the surface of all types of fibers. In the FT-IR spectrum of amidoximated-PAN fibers, there are additional bands arising from the newly formed H$_2$N-C=N-OH groups that supports the successful surface modification. The reaction of hydroxylamine with nitrile groups leads to the formation of C=N groups characterized by the band at 1665 cm^{-1}. The broad band at 3000-3700 cm^{-1} can be attributed to H-bondings of NH$_2$ and O-H in the amidoxime structure (panel a). Upon the sorption of UO$_2^{2+}$ ions, a shift was observed in the stretching band of C-N from 1218 cm^{-1} to 1248 cm^{-1} (panel b). The implication of this on the sorption mechanism is discussed in the last section.
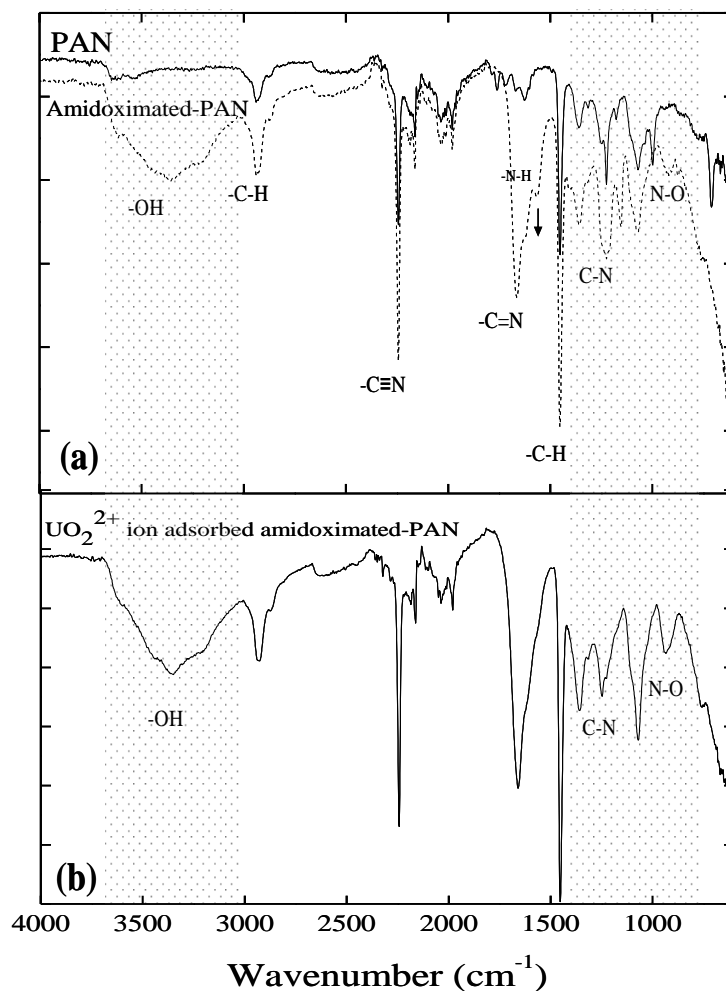
Figure 4.4. FTIR spectra of (a) PAN and amidoximated-PAN fibers, (b) uranyl ion adsorbed amidoximated-PAN fibers

Figure 4.5 presents SEM micrographs and diameter distributions of PAN, amidoxime-modified PAN, and the modified fibers after uranyl sorption. Panel a of Fig. 4.5 shows PAN fibers prepared from 4 wt % PAN/DMF solution. The average fiber diameter (AFD) was 122±39 nm. The fibers appear to possess a homogeneous morphology with some surface roughness. Upon the amidoximation process, the AFD came out to be slightly larger (127±24 nm) than untreated PAN fibers (panel b). The sorption of uranyl ions by the amidoximated-PAN fibers seemed to render the fiber thicker and undulating, as the AFD for the fibers increased to 132±26 nm (panel c). No serious deterioration of the surface texture or roughness was observed after the sorption process, and the morphology and the integrity of fibers were preserved.
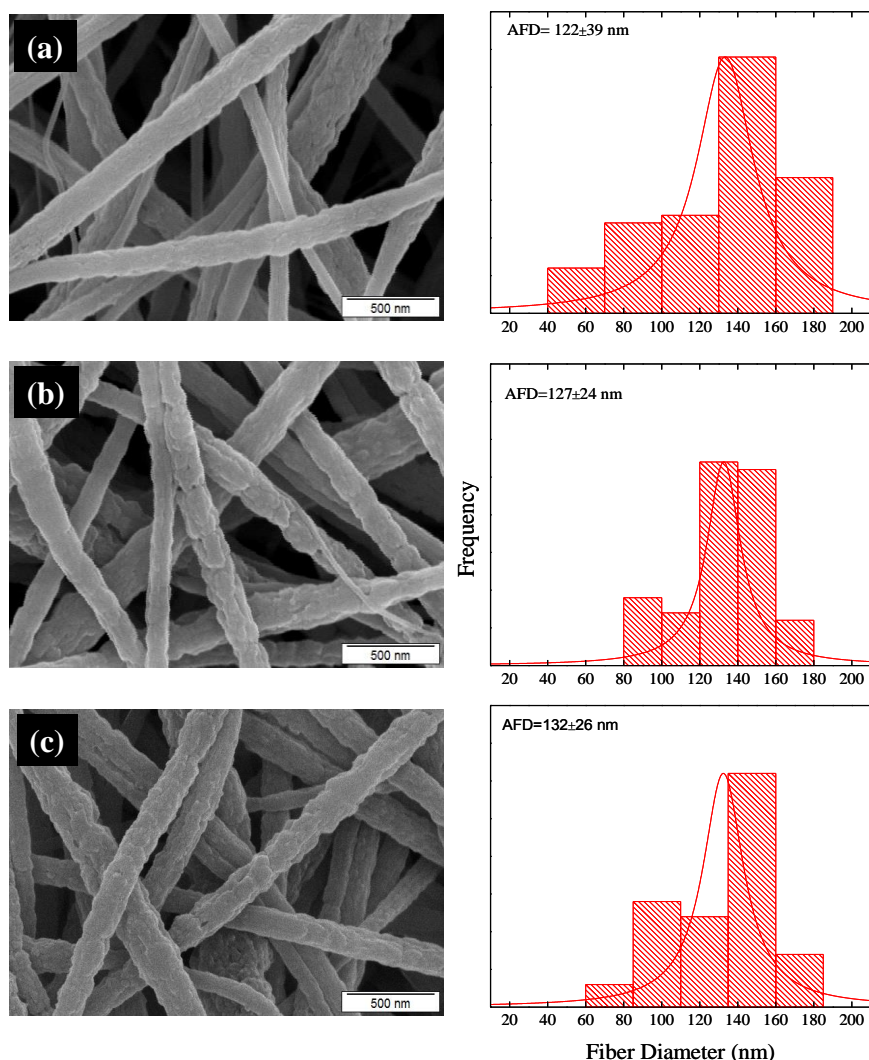
Figure 4.5. Scanning electron micrographs and corresponding fiber diameter distributions of (a) PAN fibers, (b) amidoximated-PAN fibers and (c) amidoximated-PAN fibers after uranyl ion sorption

The elemental composition of amidoximated-PAN fiber after uranyl ion sorption was elucidated using EDX analysis. Figure 4.6 shows a typical EDX spectrum of uranyl ion-loaded fiber, exposed to an initial concentration of 100 mg L^{-1}. High U(VI) initial concentration was selected due to the detection limit of EDX. The quantification is given in Table 4.3. C, N, and O signals originated from polyacrylonitrile and the presence of uranium signal indicated that uranium was fixed on the surface of the amidoximated PAN fiber. The atomic percentage of U on the fiber surface was within the range of 0.50-1.09.
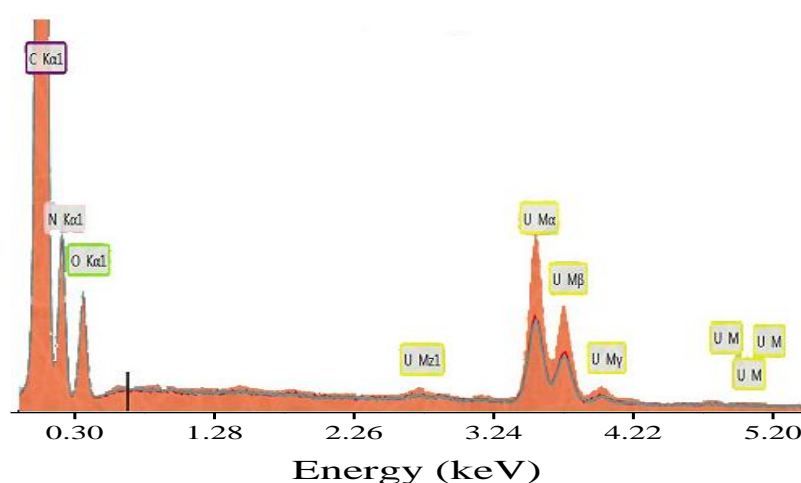
Figure 4.6. EDX spectrum of amidoximated-PAN fiber mat after uranyl ion sorption at pH 4.

Table 4.3. The weight percentages and atomic percentages (in brackets) of C, N, O, and U in amidoximated-PAN fiber after column sorption

Element	C	N	O	U
Sampling Area 1	58.69 (67.83)	26.19 (25.95)	6.60 (5.72)	8.52 (0.50)
Sampling Area 2	59.62 (68.14)	26.21 (25.69)	6.70 (5.75)	7.48 (0.43)
Sampling Area 3	55.62 (70.27)	20.39 (22.09)	6.87 (6.55)	17.06 (1.09)

4.4.3. Sorption Studies

The sorption capability of amidoxime-modified PAN fibers was compared with that of unmodified PAN fibers. The unmodified PAN fibers exhibited 19% sorption; on the other hand, amidoxime modified PAN fibers showed nearly 4 times higher sorption capacity (81%). It is worth noting that sponge has no contribution to uranyl sorption. The surface modification also transformed the hydrophobic nitrile groups into hydrophilic amidoxime groups, and the sorption of uranyl ions increased due to the chelating ability of amidoxime groups (Pekel and Guven 2003, Saeed et al. 2008, Takeda et al. 1991).

4.4.3.1. Effect of pH

The initial pH value of solution is a significant parameter in uranium(VI) sorption. Figure 4.7 shows the speciation diagram of U(VI) as a function of pH (panel a), and the extent of sorption of U(VI) ions on amidoximated-PAN fiber at different pH values (panel b). The percent U(VI) uptake increased with increasing pH from 3.0 to 4.0. The amidoximated-PAN fiber sorbent seemed to demonstrate maximum sorption at pH 4.0. At this pH, UO_2^{2+} ion is main (approximately 85% of the U(VI)) species among other chemical forms. Under lower pH values, uranium is still present in the form of free UO_2^{2+} ions, however competitive sorption with protons occurs, and ion-exchange interactions are favored (Hudson et al. 1999, Sylwester et al. 2000). Protonation can occur on the imino group of amidoxime (pKa 5.95) (Koikov et al. 1998), leading to a decrease in the chealating ability. For solutions adjusted at pH above 4.0, hydrated uranyl cations like $UO_2(OH)^+$, $[(UO_2)_3(OH)_5]^+$, $UO_2(OH)_2$, $[UO_2(OH)_3]^-$, and $[UO_2(OH)_4]^{2-}$ seem to be dominant according to the speciation analysis. In high pH media, carbonate also might contribute as ligands in solutions open to atmosphere. The change in the chemical form in terms of charge and number of hydroxyl ligands associated with possible steric limitations might be expected to decrease the extent of fixation of U(VI) at higher pH values. The major species present in solution at pH of 8.0 is the neutral uranyl cations ($UO_2(OH)_2$), the liability of which to complexation is less than the positively charged U(VI) species, the thing expected to result in lower extent of sorption.
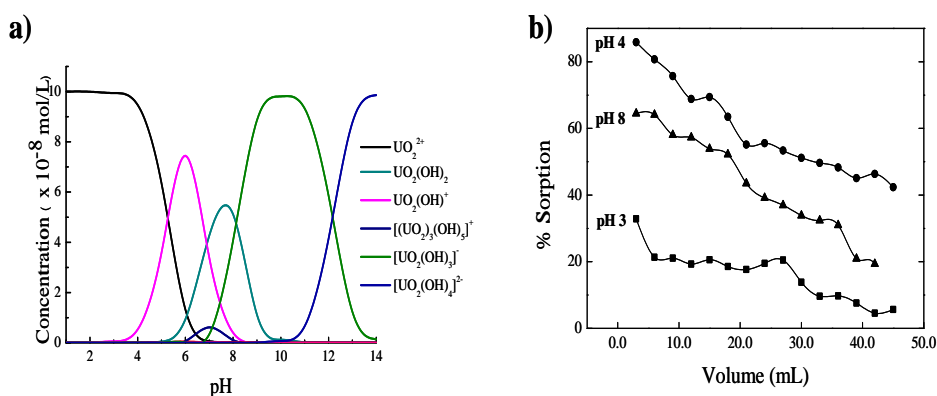
Figure 4.7. (a) Speciation diagram of U (VI), and (b) microcolumn study for U (VI) at different pH values (b). (Reaction conditions: The initial U(VI) concentration of 100 µg L^{-1}, 0.15 mL min^{-1} flow rate, 25.0 mg sorbent)

4.4.3.2. Effect of Initial Concentration

The effect of initial concentration on the extent of removal of uranyl ions by amidoximated-PAN fiber was investigated. Throughout these experiments, a fixed amount of sorbent (25.0 mg) was employed, and the initial concentration of U(VI) solutions varied in the range from 5 µg L^{-1} to 100 µg L^{-1} at a fixed pH of 4.0. Figure 4.8 displays uranyl ion sorption as a function of initial concentration. The amount of adsorbed uranyl ions increased with increasing the initial uranyl ion concentration, and at initial uranyl concentration of 100 µg L^{-1}, the sorption approached the saturation plateau. The observed behavior is probably due to the decrease in hydration effects of water, increase of entropy effects of ions in solution, and consequently a greater mobility of the uranyl ions as concentration is increased. In addition, when more U(VI) ions are present in the solution, higher fraction of available active sites takes part in the sorption process (Sureshkumar et al. 2010). This could be attributed to the associated limitation in the number of water molecules available for hydration of the exposed hydrophilic groups at the fiber surface.
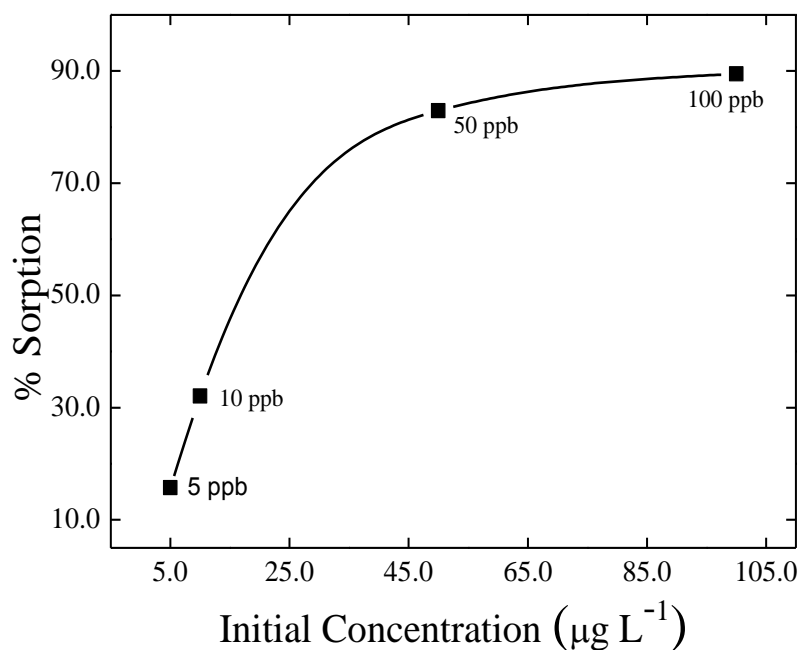
Figure 4.8. Uranyl ion sorption at various initial concentrations. (Reaction conditions: 3.0 mL sample volume, 0.15 mL·min^{-1} flow rate, 25.0 mg sorbent, at pH 4.0)

4.4.3.3. Repetitive Usability

To test the repetitive usability of the amidoximated-PAN fiber sorbent, 3 mL portions of fresh U(VI) solution at the initial concentrations of 100 µg L^{-1} and 50 µg L^{-1} were exposed to fiber samples for 14 successive trials. The results are presented in Fig. 4.9. The amidoximated-PAN fiber sorbent seems to be effective in removal of aqueous U(VI) ions even after 14 consecutive uses. In the initial trials, more uranyl ions appear to be removed at higher initial concentration, which is in line with results above. None the less, at the initial concentration U(VI) initial concentration of 100 µg L^{-1}, the percent sorption seems to decrease gradually with more applications of the fiber. It is worth noting that the repetitive loading experiments continued for 80 trials before saturation of the sorbent was reached. (Figure 4.10) The results showed that more than 85 % uranyl ion was sorbed after one use, and although sorption ability towards uranyl ions decreased steadily, 46 % removal of uranyl ions can still be achieved even at the eightieth trial of the same sorbent in the column. The most prominent consequence of this experiment is the high capacity of the sorbent under continuous flow.
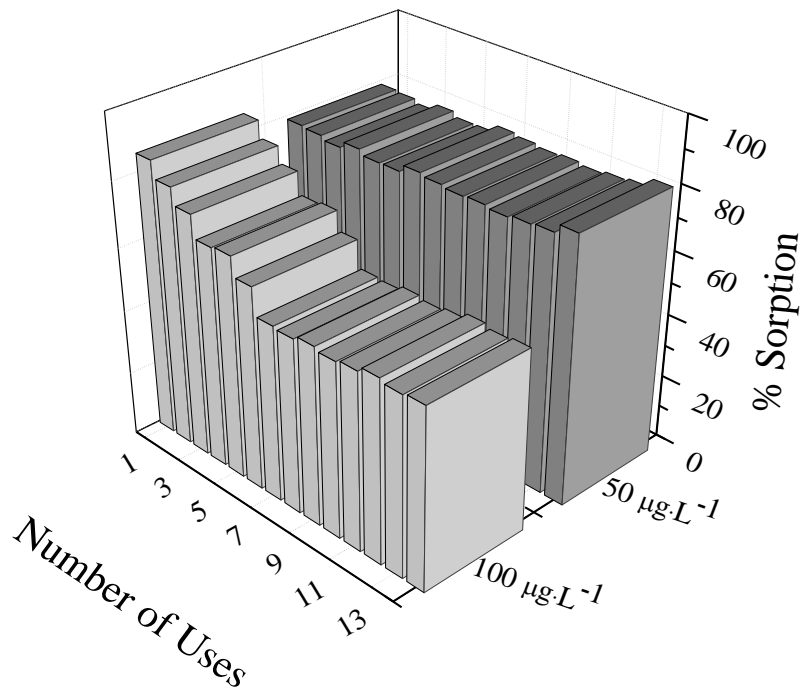
Figure 4.9. Variation of percent sorption of uranyl ion with the number of repetitive usage of the same fiber sorbent at the initial U(VI) concentrations of 50 µg L^{-1} and 100 µg L^{-1}. (Reaction conditions: 3.0 mL sample volume, 0.15 mL min^{-1} flow rate, 25.0 mg sorbent, at pH 4.0)
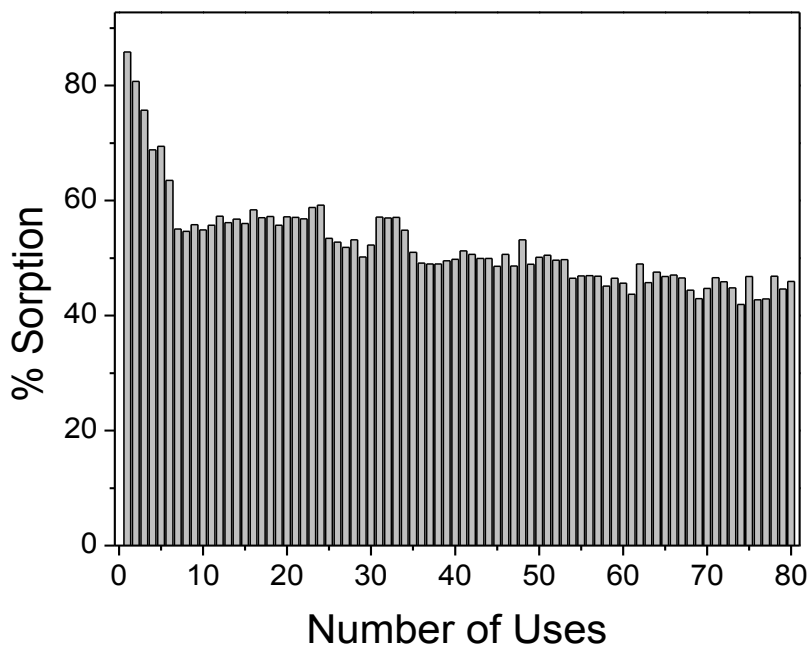
Figure 4.10. Variation of percent sorption of uranyl ion for 80 repetitive trials (initial U(VI) concentration of 100 µg L^{-1}, 0.15 mL min^{-1} flow rate, 25.0 mg sorbent, at pH 4.0)

The cumulative fixation of uranyl ions after tens of trials is interesting. The first conclusion to draw from this behavior is that the fibers possess a high density of sorption sites in comparison with the employed concentration of uranyl ions. The second conclusion relates with the apparent effectiveness of the hydration forces in solution. For ions with high charge like U(VI), the chemical potential is largely affected by the hydration forces in solution, especially in dilute solutions. As long as the chemical potential of the adsorbate on the surface is less than its chemical potential in solution, sorption proceeds spontaneously. When the ionic concentration is high, the ions become more mobile (their chemical potential increases) due to ionic repulsions, and as a result can reach the surface/compete to sorption sites more readily. This seems to be achieved when a fresh solution is fed into the column.

4.4.3.4. Desorption Tests

The uranyl ion loaded amidoximated-PAN fiber sorbents were subsequently treated with different desorbing eluents. $NaHCO_3$, EDTA, and ammonium citrate were employed as chelating agents for the release of uranyl ions and the regeneration of the sorbent. Figure 4.11 shows the elution curves which presents almost similar behavior in each case. Most of the U(VI) ions were desorbed within the first 3.0 mL cycle, and the amounts of desorbed metal ions were almost unchanged. The desorption percentages of U(VI) were 80% for 0.5 M $NaHCO_3$, 45% for 0.5 M ammonium citrate, and 34% for 0.1 M EDTA. Therefore, $NaHCO_3$ was selected as desorbing eluent due to its relatively higher desorption yield. Uranium forms negatively charged or neutral carbonate complexes, and adsorbed uranyl could be eluted from the sorbent using $NaHCO_3$ through the addition of carbonate ions as ligands to uranyl complexes.

Figure 4.12 displays the reusability of the fiber sorbent in five sorption/desorption cycles using 0.5 M $NaHCO_3$. After five cycles, the efficiency of sorption decreased from 86.0% to 59.5% while the recovery of U(VI) decreased from 80.0% to 55.0%. Therefore, $NaHCO_3$ can regenerate the sorbent effectively thus facilitating the reuse of this new fibrous material.
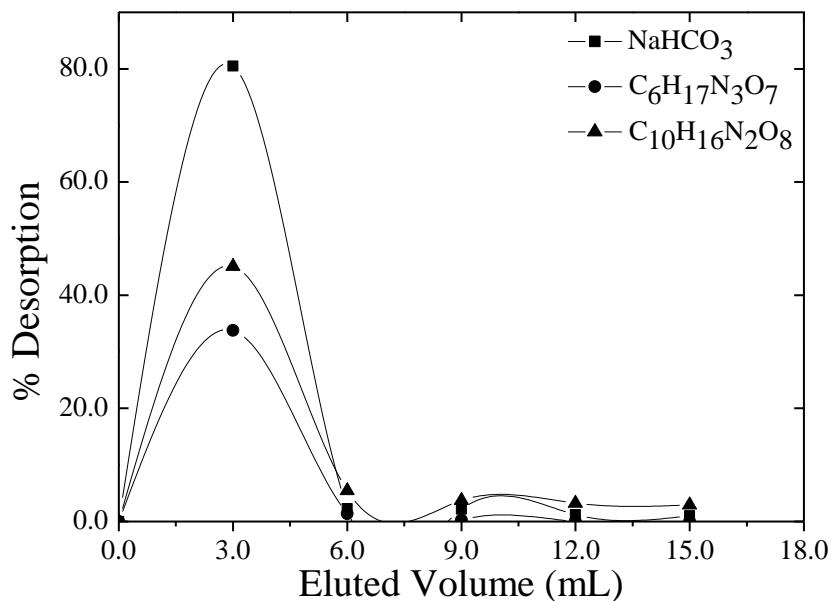
Figure 4.11. Uranyl ion desorption as a function of eluted volume. (Reaction conditions: The initial U(VI) concentration of 100 μg L^{-1}, 0.15 mL min^{-1} flow rate, 25.0 mg sorbent)
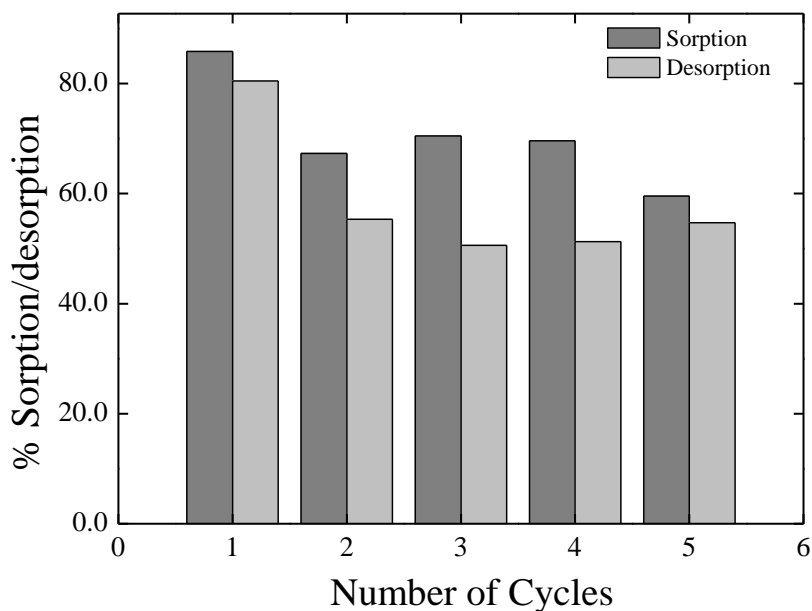
Figure 4.12. Consecutive sorption/desorption cycles of amidoximated-PAN fiber for 100 μg L^{-1} of U(VI) solution using 0.5 M NaHCO$_3$ as desorbing agent.

4.4.3.5. Brief Comments on Sorption Mechanism

As mentioned previously, the amidoximated-PAN fiber sorbent demonstrated maximum sorption at pH 4.0. Speciation analysis discussed previously suggests that, at this pH, approximately 85% of the U(VI) exists in the UO_2^{2+} chemical forms. From the sorbent side, as shown above based on FTIR characterization, the surface of the functionalized fiber is dominated by hydroxyl, amine, and nitrile groups. In acidic media these groups would normally be expected to undergo protonation. Thus at pH of 4.0, the chemical forms of the sorbent surface and the sorbate ions does not support an electrostatic hypothesis of sorption. Thus, the fixation of the UO_2^{2+} ions might be expected to proceed via formation of surface complexes that possess coordinative nature, with the lone pairs on O and N atoms in the surface groups playing the main role in interaction with the uranyl species.

The interaction of UO_2^{2+} ions with amidoximated-PAN fibers is reflected in a blue shift in the stretching band of C-N from 1218 cm^{-1} to 1248 cm^{-1}, as mentioned above in section 4.4.2. This result is compatible with previous works. For example, Pekel and Guven (Pekel and Guven 2003) observed similar type of shift at C-N streching band for amidoximated poly(acrylonitrile/*N*-vinylimidazole) complexing sorbent and was ascribed as proof for the interaction of UO_2^{2+} ions with vinylimidazole ring.
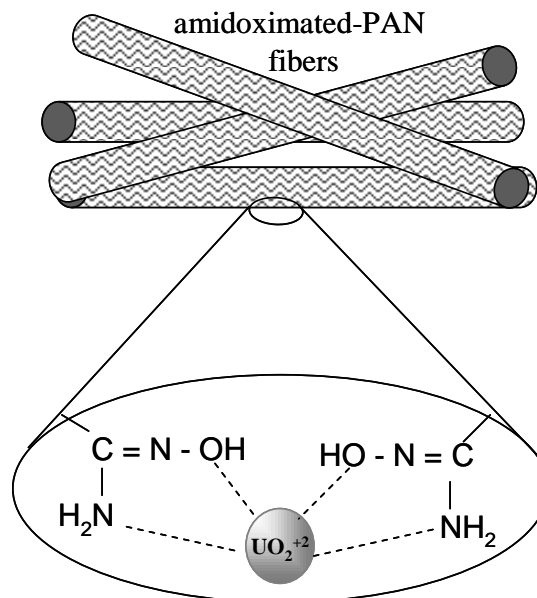
Figure 4.13. Speculative binding mechanism

It is proposed that the sorption of uranyl oxo-cations with amidoximated-PAN fibers is achieved by virtue of the strong chelating ability of amidoxime groups, which act as bidentate ligands. Based on the above discussion, a tentative binding mechanism can be suggested in Figure 4.13. This is in line with previously suggested chelation mechanisms. For example, Hirotsu et al. (Hirotsu et al. 1986) reported that the sorption of uranium originated from ligand exchange between carbonate ions and amidoxime groups accompanied by deprotonation of the amidoxime groups. Similarly, Pekel et al. (Pekel et al. 2004) proposed that the binding of amidoxime group to UO_2^{2+} ions proceeded by replacement of protons by UO_2^{2+} ions.

More spectroscopic and structural investigations are required to make more precise and detailed comments on the sorption mechanism.

4.5. Conclusion

This study demonstrated that amidoximated-PAN fibers produced by electrospinning form an effective sorbent for the removal of U(VI) from aqueous media via column-type operations. In the fabrication process, first, PAN fibers were produced. Then, a wet chemical process was applied for surface modification of PAN fibers. The nitrile groups on PAN fibers were converted to amidoxime groups using hydroxylamine hydrochloride in a neutralized medium. The surface functionalized PAN fiber network provided higher metal binding ability. The extent of U(VI) sorption on the fibers was found to depend on the pH of the medium and the initial concentration of the salt. The optimum pH for U(VI) sorption by amidoximated-PAN fibers was found to be 4.0, at which UO_2^{2+} ion is the main species. The adsorbed amount of U(VI) ions increased with an increase in initial U(VI) concentration. The ease and applicability of the process we propose in filtration can offer a convenient method for the removal of U(VI) ions via a column system. Moreover, the amidoximated-PAN fibrous filter material used in this study has high mechanical resistance, sorption ability, and efficient reusability which are in fact desired for filtration applications. Based on our preliminary results, this material is also capable to uptake various undesirable ions such as Fe(III), Cu(II), and Cd(II) from aqueous solutions. A detailed study dealing with isotherms and sorption mechanisms is underway.

CHAPTER 5

HUMIDITY SENSING PROPERTIES OF ZnO-BASED FIBERS BY ELECTROSPINNING

5.1. Abstract

Zinc oxide (ZnO) based fibers with a diameter of 80-100 nm were prepared by electrospinning. Polyvinyl alcohol (PVA) and zinc acetate dihydrate were dissolved in water and the polymer/salt solution was electrospun at 2.5 kV·cm^{-1}. The resulting electrospun fibers were subjected to calcination at 500 °C for 2 h to obtain ZnO-based fibers. Humidity sensing properties of the fiber mats were investigated by quartz crystal microbalance (QCM) method and electrical measurements. The adsorption kinetics under constant relative humidity (RH) between 10 % and 90 % were explained using Langmuir adsorption model. Results of the measurements showed that ZnO-based fibers were found to be promising candidate for humidity sensing applications at room temperature.

5.2. Introduction

Sensing and controlling humidity are particularly significant for both human life and various industrial fields. The major domestic applications of humidity sensors have been the humidity control in heating, ventilating, and air conditioning (HVAC) systems, food packaging, greenhouse agriculture, the production of electronic devices, automotive industries and in meteorology stations. In responds to the strong demands for automatic control systems, reliable, cheap, sensitive humidity sensors operated at ambient temperatures are of critical importance (Pelino et al. 1994).

Sensing devices based on metal oxide semiconductors with nanostructures have perfect chemical reactive surfaces that have water adsorbing and desorbing properties, thermal stabilities, and mechanical durability (Zhang et al. 2005, Park et al. 2010, Okur, Uzar, et al. 2012, Liu et al. 2009). The considerable attention has been focused on

the studies of one dimensional (1D) nanostructured metal oxides, *i.e.* nanorods (Zhang et al. 2005, Qi et al. 2008), nanowires (Zhang et al. 2005, Okur, Uzar, et al. 2012), nanoparticles (Erol et al. 2010), nanotetrapods (Qiu and Yang 2007), or nanofibers (Zhang et al. 2010, Wang, Li, et al. 2009, Wang et al. 2008, Qi et al. 2009, Park et al. 2009, Ding et al. 2009), and their influence on the humidity sensing performance. Many available techniques such as carbothermal reduction synthesis (Wu et al. 2008), chemical vapor deposition (CVD) (Wu and Liu 2002), electrospinning (Wang et al. 2008), hydrothermal synthesis (Liu and Zeng 2003), vapor-liquid-solid (VLS) (Xia et al. 2008), conventional precipitation (Yadav et al. 2009, 2008) have been attempted to obtain nanostructures. Among them, electrospinning provides a convenient and facile route for the fabrication of fibrous materials possessing high surface area, uniform diameters and variety of composition. Electrospinning is a facile and robust method for the production of not only polymeric (Demir et al. 2002), but also composite (Demir et al. 2004, Demir et al. 2008) and ceramic fibers (Ramaseshan et al. 2007) with diameters ranging from several nanometers to few micrometers. Moreover, chemistry tool box of electrospinning process is very wide. To date, > 200 polymer/solvent systems have been processed by this method. In addition, electrospun mats have superior feature compared to the other in terms of mechanical property. It provides mechanical integrity even if it is subjected to calcination process.

Zinc oxide, which is a wide band gap (3.37 eV) semiconductor with large exciton binding energy (60 meV) (Demir et al. 2008, Ozgur et al. 2005, Ramaseshan et al. 2007) is an ideal candidate on the production of sensors (Ding et al. 2010, Hess et al. 2009). Previously, Qiu and Yang (Qiu and Yang 2007) presented that ZnO nanotetrapod film exhibited much higher sensitivity to humidity than ZnO nanoparticle one and investigated the response and recovery time as 36 and 17 s, respectively. Hu et al. (Hu et al. 2008) evaluated response (50 s) and recovery (6 s) behavior of ZnO colloidal nanocrystal clusters. An efficient humidity sensor based on ZnO nanorods was reported by Qi and co-workers (Qi et al. 2008). LiCl-doped ZnO nanofiber humidity sensor was studied by Wang et al. (Wang, Li, et al. 2009) The best result is obtained for 1.2 wt% LiCl-doped sample, which exhibits high humidity sensitivity, rapid response (3 s) – recovery (6 s) and good reproducibility. Qi et al. (Qi et al. 2009) suggested 5.7 wt% KCl-doped ZnO nanofibers as humidity sensor with super-rapid response (2 s) and recovery (1s). Zhang et al. recently showed a contribution on Na^+-doped ZnO nanofiber membrane for humidity sensor underlying the effect of NaCl doping as 4.6 wt% and

reported the response (3 s) and recovery (6 s) behaviors. However, the humidity sensing properties and adsorption-desorption kinetics of pure ZnO nanofibers have not been reported. In the present study, we demonstrate a simple and effective route for the synthesis of ZnO nanofibers with rapid response (0.5 s) and recovery (1.5 s) to humidity. The adsorption kinetics of the fiber sensor was investigated by QCM technique which is one of a wide branch of surface acoustic wave (SAW) techniques (Ding et al. 2009). The change in resonance frequency of QCM was observed with increasing relative humidity up to 90 %. The adsorption kinetic parameters were examined using Langmuir model.

5.3. Experimental Section

5.3.1. Preparation and Characterization of ZnO Nanofibers

In a typical procedure, a sample of 2.5 g of zinc acetate dihydrate ($Zn(CH_3COO)_2.2H_2O$, Sigma-Aldrich) was mixed with 4.0 g of polyvinyl alcohol solution (18 wt%) (PVA, Sigma-Aldrich, $M_w = 30,000\text{-}70,000$ g mol^{-1}) stirred for 5 h in a water bath at 60 ºC. The metal concentration of the composite was increased by adding zinc acetate dihydrate, and the $PVA/Zn(CH_3COO)_2.2H_2O$ composites with $Zn(CH_3COO)_2.2H_2O$ concentrations ranging from 10 to 20 wt% were obtained. To perform the electrospinning process, the prepared solution was loaded into a plastic syringe and 15 kV potential difference was applied to the tip of a needle of syringe. The distance between the syringe and the metal collector was 6 cm. The feeding rate was kept constant at 4.5 mL h^{-1} using a microsyringe pump (LION WZ-50C6). The obtained electrospun fibers were dried under vacuum at 70 ºC for 8 h and calcined for 5 h at 500 ºC with a heating rate of 4 ºC min in the furnace. Figure 5.1 illustrates the procedure of manufacturing electrospun PVA/ZnO composite fibers.

The morphology of ZnO nanofibers was observed under scanning electron microscopy (SEM) using a Philips XL-30S FEG. The diameter of fibers was measured using an image processing software, ImageJ. The crystalline structure of the samples was analyzed using an X-ray diffractometer (Philips X'Pert Pro X-Ray Diffractometer) with Cu Kα radiation.
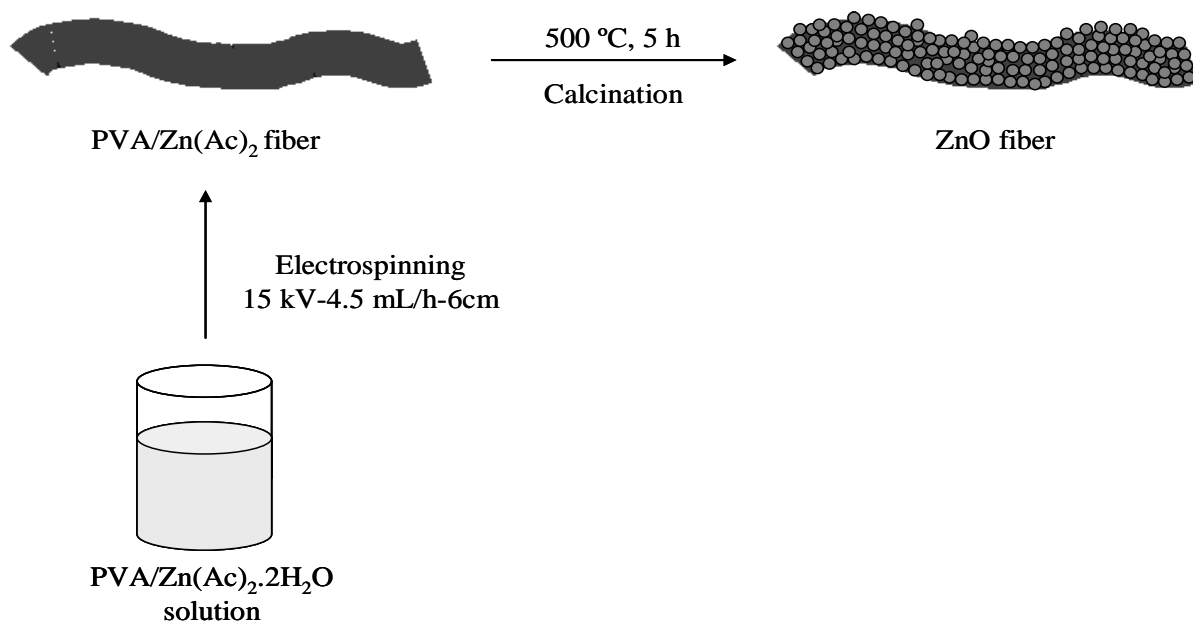
Figure 5.1. Schematic representation for preparation of PVA/ZnO composite fibers

5.3.2. Humidity Measurements Using QCM Technique

QCM technique has been used to determine the mass changes due to moist molecules with a resolution of $\sim$1 ng/cm^2. QCM consists of a quartz disk with 0.196 cm^2 area between two Au coated electrodes on both sides. The mass change (Δm) on surface of the quartz crystal was calculated from the frequency change (Δf) as shown by Sauerbrey (Sauerbrey 1959);

$$\Delta f = -\frac{2 f_0^2 \Delta m}{A\sqrt{\mu\rho}}$$

(5.1)

where f_0 is the resonant frequency of the fundamental mode of the QCM crystal, A is the area of the gold coated electrodes on the quartz crystal, ρ is the density, and μ is the shear modulus of quartz substrate. QCM with the model of CHI400A Series from CH Instruments (Austin, USA) has been used to measure the change in the resonance frequency due to mass loading of water molecules after exposure of the QCM electrodes for various humidity levels between 10 % and 90 % relative humidity (RH). QCM is connected via a USB interface to a computer. QCM electrodes used in our study are made of AT-cut piezoelectric quartz crystal with oscillation frequencies between 7.995

MHz-7.950 MHz. The density (ρ) of the crystal is 2.684 g cm^{-3}, and the shear modulus (μ) of quartz is 2.947×10^{11} g cm^{-1} s^{-2}. The change of 1 Hz corresponds to the mass of 1.34 ng of materials adsorbed onto the crystal surface of an area of 0.196 cm^2. Both QCM sensor and gold contacts for electrical measurements with 15 μm channel length and 300 μm channel width fabricated with thermal evaporation technique under vacuum of 5×10^{-6} torr.

Figure 5.2 shows the experimental setup to investigate the adsorption and desorption kinetics of ZnO nanofiber films under various humidity environments between 10 % - 90 % RH at room temperature. Relative humidity value inside a test cell with volume of 100 cc is varied between 10 % - 90 % by controlling the ratio of wet and dry air flow via MKS flow-meter control system between 0-1000 sccm between 10 steps. The measurements were simultaneously taken using a combined system of QCM sensor and a commercial Sensirion humidity sensor. The sensor has an EI-1050 selectable digital relative humidity and temperature apparatus with a response time of 4s. The humidity sensor is connected to a PC using a Labview program to collect data via USB port controlled by U12 ADC system combined with a single chip sensor module (SHT11) manufactured by Sensirion (Staefa, Switzerland).
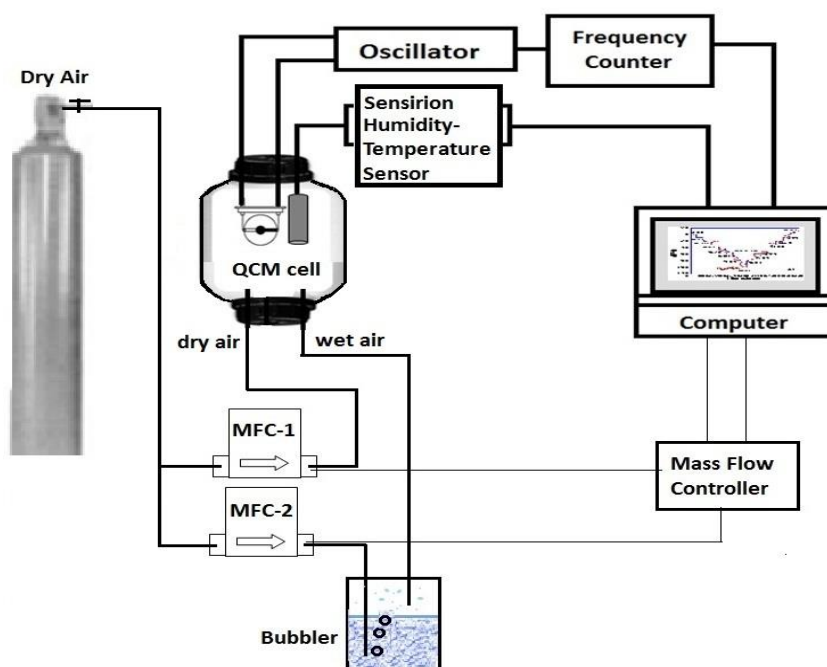
Figure 5.2. The experimental QCM setup to measure the adsorption and desorption kinetics of ZnO nanofiber films under various relative humidity conditions between 10 % RH and 90 % RH.

The commercial humidity sensor shows 10 % RH when 1000 sccm of dry air is sent through the QCM cell, while it shows 90 % RH when 1000 sccm of wet air (obtained by passing dry air through a bubbler kept at a constant temperature of 25 ^{o}C).

5.4. Results and Discussion

5.4.1. Structural Characterization of ZnO Nanofibers

The graphical demonstration of this entire process in given in Figure 5.1. Aqueous solutions of PVA and zinc acetate dihydrate were mixed and homogeneous solutions were subjected to electrospinning at 2.5 kV/cm. Figure 5.3. (a-d) shows SEM micrographs of PVA/Zn(CH$_3$COO)$_2$ fibers (before calcination). They have smooth surface and average fiber diameter (AFD) was in the range of 100 to 120 nm. The salt content in electrospinning solution is one of the important parameters to control the diameter of fibers. The dependence of the AFD on weight percentage of the salt is shown in Figure 5.4. It exhibits an exponential growth with salt content. The ionic strength of solution is directly proportional with salt concentration. This reflects an increase in current during electrospinning process, i.e. solid content transferred from tip to the grounded collector increases. Thus, thicker fibers are obtained in salty electrospining solutions. The PVA/ Zn(CH$_3$COO)$_2$ fibers were subjected to calcination at 500 ºC in air and ZnO-based fibers were obtained. In other words, the integrity of fibers remains almost unchanged upon calcination process. However, a significant reduction in diameter was observed approximately 20 % on average for all solutions we tried. The occurence of shrinkage is due to the removal of PVA from the fiber volume and crystallization of ZnO phase (Fig. 5.3(e-h)). In calcination process, the temperature was fixed to 500 °C at which nucleation and growth process readily occurs. Particulate ZnO crystals are evident on the fibers.
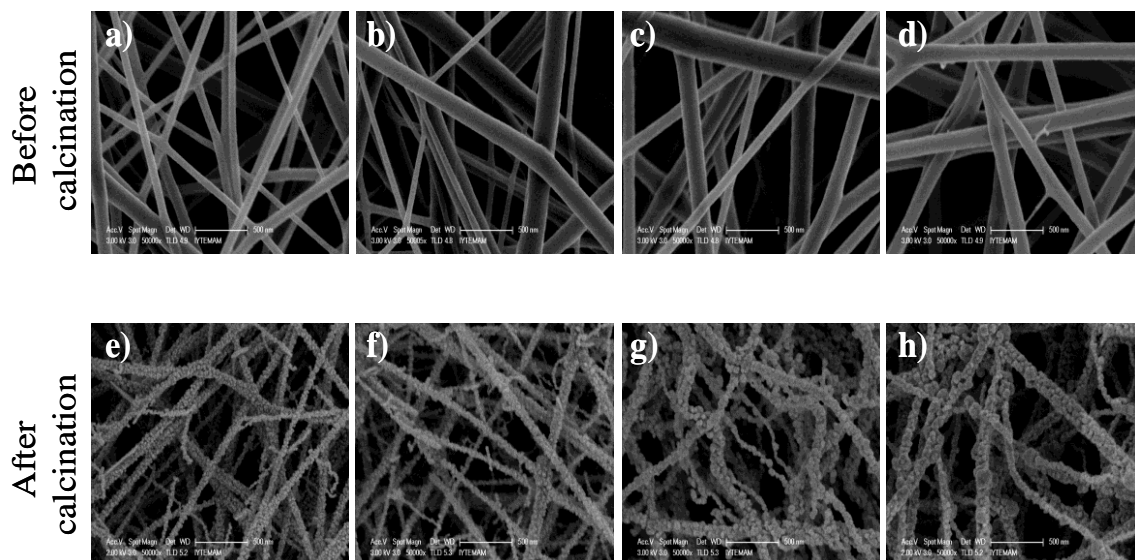
Figure 5.3. SEM micrographs of PVA/ZnO composite fibers and ZnO nanofibers with respect to increasing amount of $Zn(OAc)_2.2H_2O$ (a,e) 10 wt%, (b,f) 14 wt%, (c,g) 17 wt%, (d,h) 20 wt%
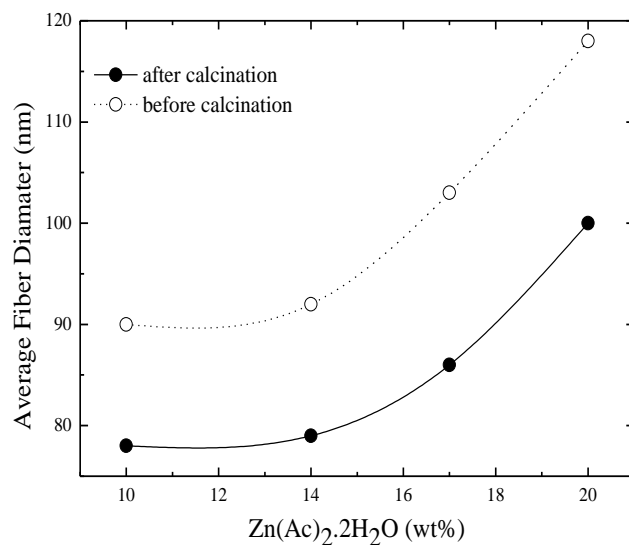
Figure 5.4. Average Fiber Diameter (AFD) versus percent weight of $Zn(OAc)_2 \cdot 2H_2O$

XRD pattern of the ZnO fiber mat is displayed in Figure 5.5a. From the diffractogram, eight diffraction planes corresponding to (100), (002), (101), (102), (110), (103), (112), (201) are present. They are characteristics signals of the wurzite type ZnO phase (JCPDS 79-0207). Furthermore, the average crystallite size of the

product was estimated by Debye-Scherrer equation employing on the maximum intense reflection (101), it was found to be approximately 15 nm. This size is consistent with the size of particles we observed in SEM micrographs. Figure 3.4(b) shows the FTIR spectra of ZnO fibers. Along with the vibrational signal of ZnO at 600 cm^{-1}, an intense signal of -CH$_2$ stretching was also observed at around 1450 cm^{-1}. Moreover, the bands at about 850 and 750 cm^{-1} are assigned to the vibrations of C-O, C-C groups, respectively. This presence of these signals indicates that PVA still remains in the system and polymeric residue is not removed completely upon calcination. This system was subjected to thermogravimetric analysis to figure out the mass content of organics after calcination process. According to this measurement, approximately 10 % organic residue remains in the fibrous system. This amount of polymeric residue may be argued about to reduce the humidity efficieny of material. However, this property meets the requirement of many applications. It must be considered that pure inorganic fibers cannot provide flexibility due to their brittle nature. The presence of low amount of organics in the system may prevent the formation of undesirable brittle nature.
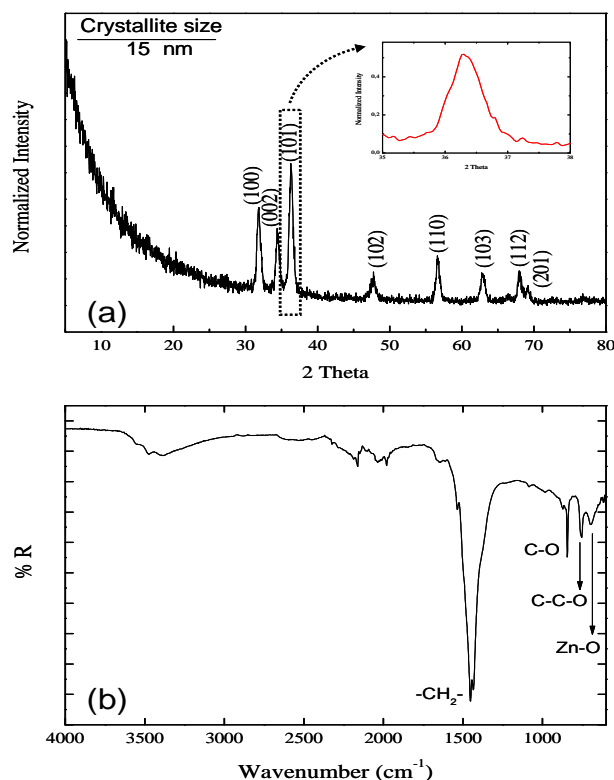
Figure 5.5. (a) X-ray diffraction pattern of ZnO nanofibers and the inset is an enlargement of the ZnO (1 0 1) peaks for the calculation of crystallite size, (b) FTIR spectra of ZnO nanofibers after calcination.

5.4.2. QCM and Electrical Responses under Varying RH

Figure 5.6 shows both adsorption - desorption responses due to the change in QCM resonance frequency comparing with simultaneously measured resistance changes of ZnO nanofiber coated sensors. The RH lies in the range of 10 % and 90 %. The negative frequency response (blue line) is given on the left side of the plot, while the corresponding resistance (red circle) is presented on the right side of the plot. Three types of adsorption and desorption cycles zoomed out in Figure 5.6b-d have been used to observe reproducibility and sensitivity of ZnO nanofiber coated QCM sensors against relative humidity changes. Resistance of the ZnO nanofiber sensor is changed on the order of 4 under 12V applied bias voltage as a result of the possible disassociation of the adsorbed moist molecules on the oxygen vacancies on the n-type ZnO surface similar to our previous work (Erol et al. 2010). Figure 5.6b shows three cycles of QCM and resistance responses when sent only dry and wet air consequently with 200s periods to observe maximum adsorption and desorption kinetics.
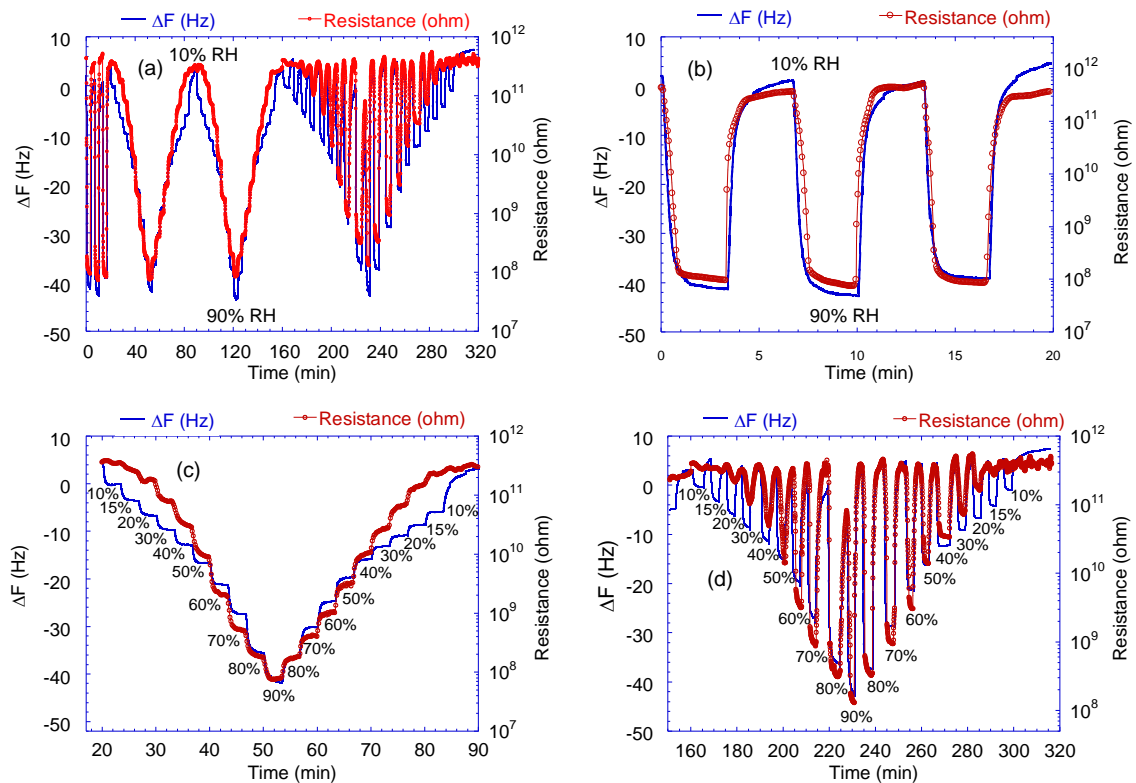
Figure 5.6. Adsorption/desorption responses due to QCM resonance frequency changes comparing with simultaneously measured resistance changes of ZnO nanofiber coated sensors between 10 % and 90 % RH for 6 hours (320 min)

QCM frequency counter is set to '0' Hz as the starting point for the minimum relative humidity at 10 % RH when full of dry air with 1000 sccm is sent through the test cell. The negative QCM frequency response shows maximum change around - 43 Hz, when wet air with 1000 sccm is sent (at 90 % RH measured with Sensirion humidity sensor). Resistance of the sensor is decreased from 5×10^{11} to 7×10^{7} ohm. Figure 5.6c shows the long time (around 1h) stepwise adsorption and desorption response of ZnO nanofiber loaded QCM and resistive sensors. To create step change in the relative humidity inside the test cell, the wet/dry air ratio is increased to 1000 sccm with 200s intervals. Both QCM frequency response and resistance change showed similar behavior above 60 % RH during adsorption/desorption processes. Similar responses are observed when short time relative humidity changes are applied. Figure 5.6d shows the short time (200 s) adsorption and desorption response of ZnO nanofiber loaded QCM and resistive sensors. To create short time relative humidity pulses, the wet/dry air flow ratio is increased as 100 sccm for each 200s periods, while after each adsorption process, the maximum desorption process is applied by sending maximum dry air with 1000 sccm. The results show that the response time against quick relative humidity changes of ZnO nanofiber sensors are less than 0.5s for adsorption process, while it is around 1.5s, 3 times larger for desorption process.

Figure 5.7 shows maximum adsorption/desorption responses due to QCM resonance frequency and resistance changes of ZnO nanofiber sensors comparing with relative humidity (RH) values simultaneously measured with a Sensirion commercial RH sensor between 10 % and 90 % RH. There are two distinct behaviors for both QCM and resistance signals before and after 60 % RH. The QCM resonance frequency decreases linearly with relatively higher slope ($m = -0.74 \, RH / Hz$) up to 75 % RH with increasing relative humidity as shown in Figure 5.7c. Similar trend is observed in resistance changes in Figure 5.7b. But resistance decreases exponentially with increasing relative humidity as shown with exponential fit ($R=2.14e^{-0.125xRH} \, ohm$).

The hysteresis-like behavior in both QCM and resistance signals between adsorption and desorption process for varying relative humidity between 10 % and 90 % is clearly seen in Figure 5.7c. But the resistance hysteresis is quite larger during desorption process compare to QCM frequency change. The exponential relationship between QCM frequency and resistance changes is shown in Figure 5.7d. There is a

dramatic exponential dependence of resistance change on the amount of absorbed moist molecules during desorption process at higher relative humidity values due to possible
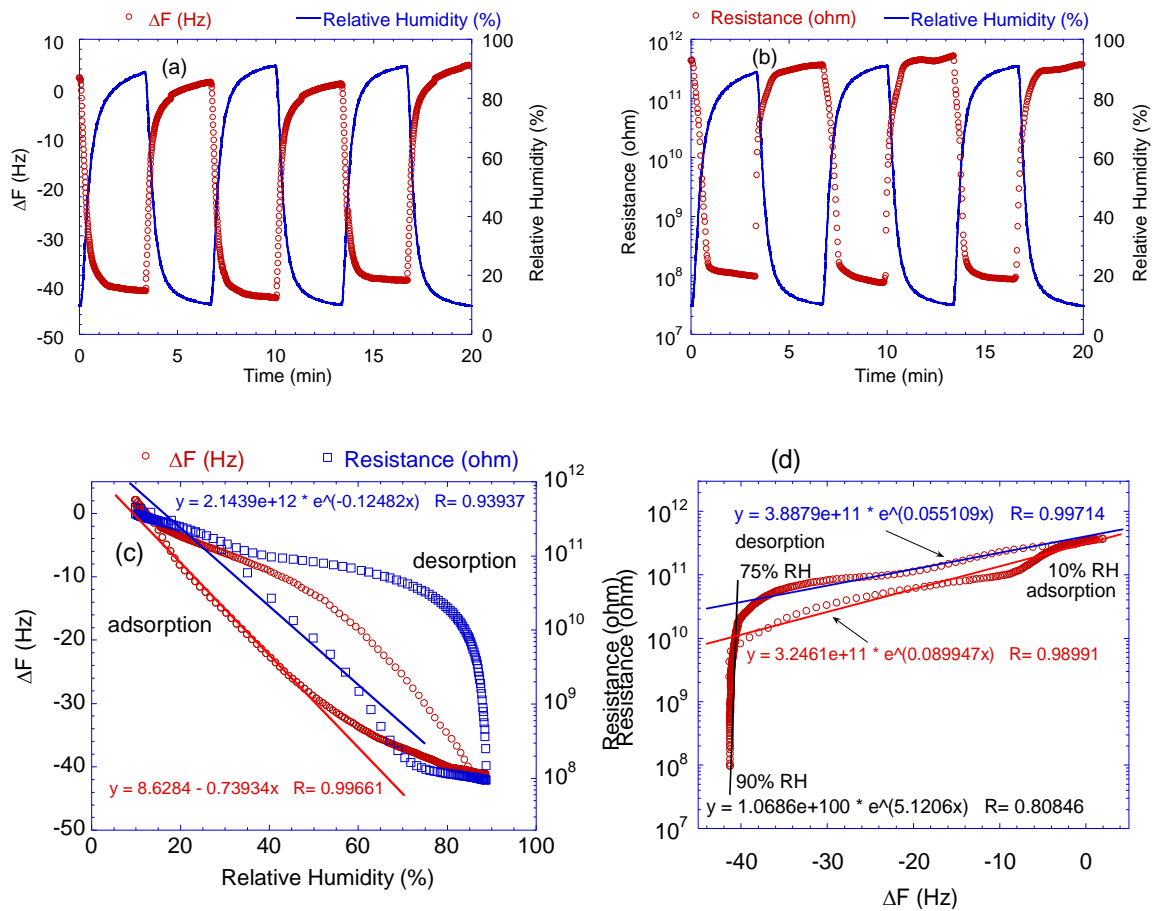
Figure 5.7. Adsorption/desorption responses due to (a) QCM resonance frequency and (b) resistance changes of ZnO nanofiber sensors comparing with (c) relative humidity (RH) values simultaneously measured with a Sensirion commercial RH sensor between 10 % and 90 % RH. (d) The exponential relationship between QCM frequency and resistance changes

condensation. This exponential relationship between adsorbed moist molecules and the increasing conductance of ZnO-based nanofiber sensors under varying relative humidity was explained by Erol et al. with hopping transport mechanism of electrolytic conductance (Erol et al. 2010). It is well-known that ZnO is n-type semiconductor due to localized donor levels in the band gap caused by oxygen vacancies and interstitial Zn atoms in the lattice. The oxygen vacancies become active sites for dissociation of the water molecule (Schaub et al. 2001). The dipoles of the first hydroxylated layer of water meniscus on the surface create an affinity for moisture molecules via Vander Walls

forces for physisorption process. The electric field applied to the water molecules between gold electrodes with 15 μm gap and under 12V is close to $0.8{\times}10^6$ V m^{-1}. Under such a high electric field, hydroxyl groups are formed providing protons as charge carriers of the hopping transport. Hence electrolytic conduction causes an exponential decrease in the resistivity of ZnO nanofiber-based humidity sensor.

The mechanism can also be viewed from macroscopic perspective. Interaction of water molecules with ZnO fiber surface plays an important role in adsorption process. The surface of ZnO fibers is sensitive to atmospheric moisture due to its high reactivity with water molecules. The molecules can be adsorbed on metal oxide surface molecularly either through H bonding or dissociated form of H_2O. Therefore; metal oxide surface is inevitably covered by surface adsorbed water molecules meaning that there is a skin layer made up of surface adsorbed water molecules. The adsorbed water on zinc oxide surface can be categorized into two distinctively different water species: i) chemisorbed water containing rigid water species with restricted mobility near the solid surface; ii) physisorbed water molecules that are very loosely adsorbed water molecules which are mobile and can exchange slowly with gaseous water molecules in air (Nagao 1971a, Demir, Koynov, et al. 2007). Mass transfer of water molecules to and from the interaction region is mainly mediated and facilitated by the latter type of water present on the outermost surface. Demir et al previously showed the existence of surface-bound water on ZnO using temperature dependence solid state nuclear magnetic (NMR) spectroscopy (Demir, Castignolles, et al. 2007). Annealing of ZnO nanoparticles at mild temperatures < 360 K were performed during NMR measurement. It was clearly demonstrated that as the annealing process is performed, the proton signal originating from the water species decreases. This result indicates the dynamic desorption process taking place at the physisorbed layer of the watery skin of ZnO nanoparticles. We believe that similar type of adsorption-desorption process takes place in our particular fibrous ZnO system.

5.4.3. Theoretical Analysis of QCM Results Using Modified Langmuir Model

The Langmuir adsorption isotherm model was frequently used to analyze adsorption data to explain the adsorption-desorption kinetics of gas molecules in the literature (Erol et al. 2010, Okur et al. 2010). Basically, the relationship between the

surface adsorption and desorption rates and frequency shift (Δf) for QCM can be expressed as following,

$$\frac{d\Delta f}{dt} = (\Delta f_{max} - \Delta f)k_a C - k_d \Delta f \qquad (5.2)$$

where Δf_{max} is the maximum frequency change at the maximum humidity range, C is the concentration of the adsorbed gas, k_a and k_d are the adsorption and desorption rates, respectively. Integration of the Equation 5.2 leads to the solution of the first order differential equation as following,

$$\Delta f(t) = \Delta f_{max} K'(1 - e^{-k_{obs}t}) \qquad (5.3)$$

where K' is the association constant and k_{obs} is the inverse of the relaxation time. The change in the mass due to moisture adsorption can be fitted to the Langmuir adsorption isotherm model since the frequency shift is directly proportional with the change of the absorbed mass according to the Sauerbrey relation given in Equation 5.1. The time dependence of the amount of absorbed water molecules on the film surface Δm_t can be defined as,

$$\Delta m_t = \Delta m_\infty \left(1 - e^{-t/\tau}\right) \qquad (5.4)$$

where $\tau^{-1} = k_a$ [$water\ vapour\ molecules$] $+ k_d$, Δm_∞ is the maximum adsorbed mass of the moist molecules on the surface, for very long times, when t→ ∞, is calculated as 54.75 ng.

Figure 5.8 shows the least square fit (solid line) using the Langmuir adsorption isotherm model given in Equation 5.4 for the adsorption parts of the data between 10 % RH and 84 % RH given in Figure 5.7b. The relaxation time τ is obtained as 0.3 min. The average values of adsorption and desorption rates (k_a and k_d) between 10 % RH and 90 % RH were calculated as 3453.6 M^{-1} s^{-1} and 0.0147 s^{-1}, respectively.

The corresponding Gibbs free energy ΔG of adsorption/desorption process at a constant temperature can be calculated with $\Delta G = -RT \ln K_{eq}$ (Qiu et al. 2009), where K_{eq} is equilibrium constant ($K_{eq} = k_a / k_d$), R is the universal gas constant and T is the temperature (298K). The calculated equilibrium constant K_{eq} and Gibbs free energy

$$\Delta m_t = \Delta m_{\infty} \left(1 - e^{-t/\tau}\right)$$

	Value	Error
Δm_{∞}	54.75 ng	0.0407
τ	0.3 min	0.0206
Chisq	63.762	NA
R	0.9989	NA
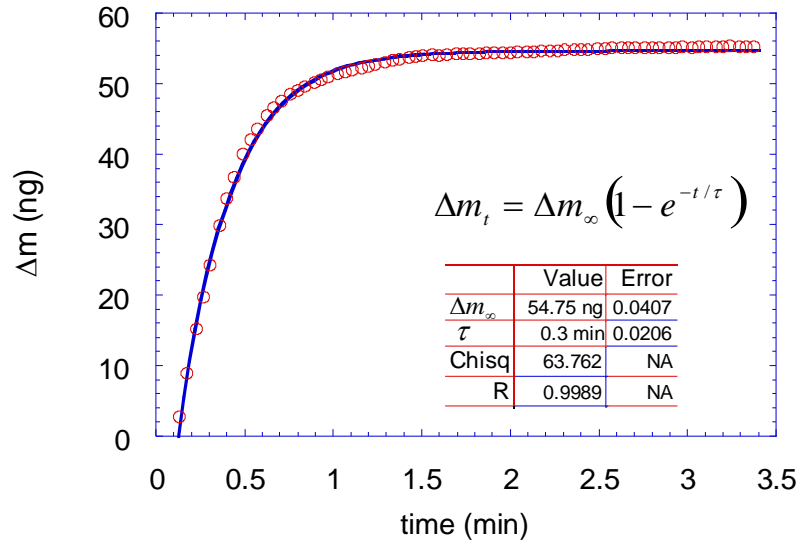
Figure 5.8. The least square fit (solid line) to the Langmuir adsorption isotherm model given in equation (4) for the adsorbed water mass between 10 % - 84 % RH.

values are 234939 and -30.64 kJ/mol for the adsorbed water mass between 10 % - 90 % RH, respectively. The Gibbs free energy with negative sign shows that there is an energy loss for water molecules on ZnO nanofiber film surface during adsorption process.

5.5. Conclusion

In this study, Quartz Crystal Microbalance (QCM) technique is used to analyze the water vapor adsorption and desorption kinetics of ZnO-based fibers synthesized using electrospinning. The resistance of the fiber sensor decreases by about four orders of magnitude with increasing relative humidity (RH) from 10 % to 90 % RH. The response and recovery time of the sensor is around 0.5s and 1.5s, respectively. The QCM resonance frequency decreases linearly while the resistance decreases exponentially with the increasing RH. The adsorption and desorption of moisture rates and Gibbs free energy kinetic parameters were determined by using dynamic Langmuir

model. The values of adsorption and desorption rates were calculated as 3453.6 M^{-1} s^{-1} and 0.0147 s^{-1}, respectively. The Gibbs free energy for adsorption cycle is found to be as -30.64 kJ mol^{-1}. Thus, QCM results show that the ZnO nanofibers are very sensitive to relative humidity changes and give reproducible adsorption and desorption kinetic behaviors for both short and long time periods. The ZnO nanofibers on QCM respond like a commercial RH sensor and can be used for potential humidity sensor applications.

CHAPTER 6

VOCs SENSOR BASED ON METAL OXIDE NANOFIBROUS MEMBRANE/QCM SYSTEM PREPARED BY ELECTROSPINNING

6.1. Abstract

We report a simple synthetic route to fabricate crystalline ZnO and CeO_2/ZnO nanofibrous mats and their sensing characteristics against volatile organic compounds (VOCs) such as benzene, propanol, ethanol, and dichloromethane. Precursor fibers were fabricated by simultaneous electrospinning of poly(vinyl alcohol) and metal salt(s) at 2.5 kV cm^{-1}. The fibers were directly deposited on the crystal surface of quartz crystal microbalance (QCM). The crystal, which was coated by nanostructured PVA/metal precursor(s) fibers, was subjected to calcination in air at 500 °C for 5 h. The formation of oxide based nanofiber mat was revealed by scanning electron microscopy and X-ray diffraction. Upon exposure of the nanofiber mats to the VOCs, the compounds adsorbed to the surface of oxidic fibers. The physisorption of the compounds was confirmed by FTIR and QCM. Both systems showed sensitivity to the VOCs and they hold a broad promise particularly for sensing applications of volatile alcoholic compounds. The introduction of CeO_2 into the ZnO structure reduced the sensitivity of ZnO most probably due to the change in crystalline structure and decrement of oxygen vacancies.

6.2. Introduction

Volatile organic compounds (VOCs) are major contributors to indoor air pollution. Involuntary inhalation of VOCs leads to the numerous diseases for children and elderly people particularly for those having asthma, allergies, or other respiratory illness and causes special risks. Prolonged exposure to these pollutants can cause cancer, central nervous system damage, haematological problems, as well as sensitization involving the skin, eyes, and lungs (Jones 1999, Kampa and Castanas

2008, Hakim et al. 2012). Because of the importance of indoor air quality for the health and welfare of people, the utilization of highly efficient sensors for the detection and monitoring of VOCs became a crucial attempt.

The currently available sensing approaches to detect VOCs are mainly depending on the identification of output signals of optical, electrochemical, potentiometric, and quartz crystal microbalance (QCM) measurements (Bevan et al. 1991, Elostua et al. 2006, Mori et al. 2009, Si et al. 2007). Among them, QCM sensors are stable, sensitive to mass changes even smaller than nanogram scale, as well as are operated at room temperature. The operation principle of QCM is based on resonance frequency shift upon adsorption of species on the QCM electrode. The sensing ability of QCM toward a toxic vapor is indubitably influenced by the characteristics of coating materials that function as an adsorptive surface. To date, ceramics, metals, polymers, thin films, lipids, dendrimers, waxes and ionic liquids have been employed as active coatings on QCM surface (Grate 2000, Ricco et al. 1998, Xu et al. 2008). Wang and coworkers (Wang et al. 2010) proposed fibrous polyethyleneimine (PEI)/polyvinyl alcohol (PVA) membranes as sensitive QCM coatings for formaldehyde sensing. The sensitivity of the fibrous membrane coated sensors was three-fold higher compared to that of flat membrane coated ones. Especially interesting is the effort in the fabrication of coating highly sensitive to trimethylamine by the same group of authors (Wang et al. 2011). They deposited nano-nets of polyacrylic acid (PAA) membranes by electrospinning/electro-netting on a QCM electrode.

Recent attempts to enhance the sensor sensitivity and selectivity for specific analytes have focused on developing one-dimensional (1D) nanostructural coatings (Ding et al. 2010, Lee et al. 2009, Wang et al. 2006). Nanofibers are broad class of 1D nanostructures, which have evoked considerable attention as sensing materials because of their excellent chemical and physical properties by virtue of gigantic aspect ratios. Probably the most versatile and practical technique for the fabrication of organic and/or inorganic nanofibers is electrospinning (Huang et al. 2003, Sigmund et al. 2006). This technique allows controlling over the diameter, morphology, porosity, alignment, and composition of the resulting fibers which may lead to enhanced sensing capacity compared to continuous films.

Electrospun semiconductor metal oxide (SMO) fibers have been recognized with perfect chemical reactive surfaces that have excellent sensitivity, fast response and recovery were used for vapor sensing. For example, Liu et al. have observed toluene sensing property of NiO-SnO$_2$ composite fiber (Liu et al. 2011). The LaFeO$_3$, (Fan et al. 2011) ZnO and In$_2$O$_3$ (Zhang and Qiao 2012) nanofiber sensors have showed good reversibility and selectivity to ethanol. However, the optimum sensing properties of the afore-mentioned materials were achieved at high operating temperature, and accordingly the applied technique restricts their applicability for the detection of VOCs in the ambient environment. As a representative example to metal oxide coated QCM applications for volatile sensing is, by far, TiO$_2$ fibers functionalized with PEI layers. The efficient formaldehyde sensing responses of PEI-modified TiO$_2$ fibers were attributed to both high surface area of electrospun TiO$_2$ based fibrous mat and the interaction between formaldehyde molecules and primary amine groups of PEI (Wang, Cui, et al. 2012).

Herein, QCM and electrospinnning techniques were merged for the high performance sensing against VOCs. We focused on the fabrication of simple and binary metal oxide membranes consisting of electrospun fibers (ZnO and CeO$_2$/ZnO) on quartz crystals for the detection of benzene, propanol, ethanol, and dichloromethane. The structural properties of the metal oxide fibers and sensing performances of the resulting membranes were examined.

6.3. Experimental Section

6.3.1. Chemicals

Poly(vinyl alcohol) (Sigma-Aldrich, 87-90% hydrolyzed), cerium(III) nitrate hexahydrate (Fluka, ≥99.0%), zinc acetate dihydrate (Sigma-Aldrich, ≥98%), dichloromethane (Sigma-Aldrich, 99%), benzene (Merck, ≥98%), ethanol (Merck, 96%), 2-propanol (Merck, 99.8%) were all used as received. Deionized water (18.2 MΩ cm) was used throughout the study.

6.3.2. Fabrication of Electrospun Metal Oxide Nanofibers

The metal salt, $Zn(CH_3COO)_2.2H_2O$ (2.5 g, 11.4 mmol) was added to a 18 wt% aqueous solution of PVA. For the fabrication of binary metal oxide fibers, $Zn(CH_3COO)_2.2H_2O$ (2.5 g, 11.4 mmol) and $Ce(NO_3)_3.6H_2O$ (2.0 g, 4.60 mmol) were added analogously to the polymer solution. The resulting mixtures were stirred for 5 h in a water bath at 60 ºC.

The fibrous membranes coating on the QCM electrode via electrospinning is schematically depicted in Figure 6.1. The viscous solutions of PVA/metal salt precursor(s) were loaded into plastic syringe, and connected to a high voltage generator (Gamma High Voltage Research, Ormond Beach, FL, U.S.A.). As a counter electrode, QCM crystal was removed from its electrodes and attached to the grounded aluminium foil. The feeding rate was fixed at 5.5 mL h^{-1} using a microsyringe pump (LION WZ-50C6). The electrospinning process was performed through the QCM electrode at a 4 cm tip-to-collector distance for 5 min. A voltage of 10 kV was applied to the needle of the syringe. The electrospun fibers coated QCM was dried under vacuum at 70 ºC for 8 h and calcined for 5 h at 500 ºC with a heating rate of 4 ºC min^{-1} in a chamber furnace (Protherm PLF 120/12).
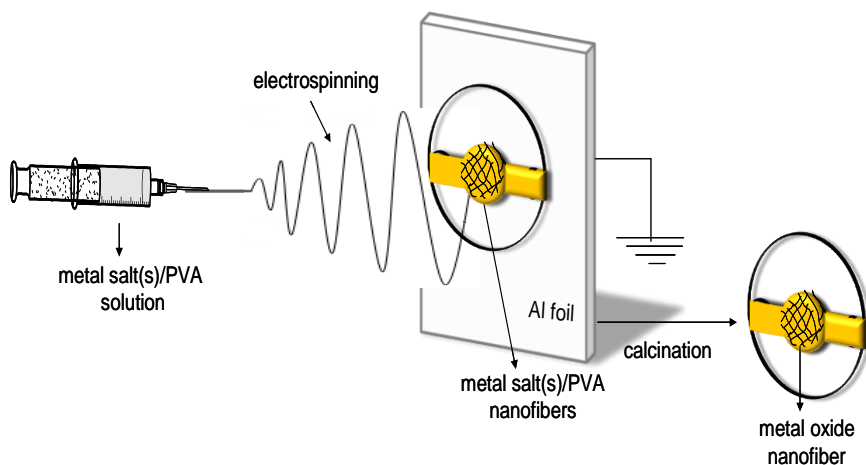
Figure 6.1. Scheme of the preparation of electrospun metal oxide fibers coated QCM

6.3.3. Characterization Methods

The morphological observations of the nanofibers on QCM crystal were performed using Scanning Electron Microscope (SEM) in a FEI Quanta 250 FEG. The average fiber diameter was calculated from SEM micrographs using the Fiji/ImageJ software. X-Ray diffraction (XRD) patterns were acquired by using a Philips X'pert Pro diffractometer monochromatized $Cu_{K\alpha}$ radiation (λ = 1.540 Å). The sizes of the crystallites were estimated by using the Scherrer equation (Klug and Alexander 1974b). Thermogravimetric analysis (TGA) of the composite fibers was studied by a Perkin Elmer Diamond TG/DTA. The Brunauer-Emmett-Teller (BET) surface area of the samples was measured by nitrogen adsorption using a Micromeritics Gemini V instrument. Prior to the measurement, the samples were degassed at 400 °C for 6 h in vacuum to remove any adsorbed material from the fiber surface. Fourier transform infrared (FTIR) spectra were registered in a Perkin Elmer Spectrum 100 FTIR Spectrometer (Shelton, U.S.A.), equipped with Pike Miracle single reflection horizontal attenuated total reflection (ATR) accessory.

The sensing responses of metal oxide nanofibers were measured by QCM technique. A schematic representation of the experimental setup was reported elsewhere (Horzum et al. 2011). A time-resolved QCM (CHI400A Series from CH Instruments (Austin, USA)) was used to measure the change in the resonance frequency due to the loading of volatile organic compounds after exposure of the QCM electrodes (AT-cut piezoelectric quartz crystal). The mass change (Δm) on surface of the quartz crystal was determined with the Sauerbrey equation (Sauerbrey 1959):

$$\Delta f = -\frac{2f_0^2 \Delta m}{A\sqrt{\mu\rho}} \qquad (6.1)$$

where Δf is the frequency change (Hz) and f_0 is the fundamental frequency of the crystal (7.995 MHz). The density (ρ) of the crystal is 2.684 g/cm^{-3}, and the shear modulus (μ) of quartz is 2.947×10^{11} g cm^{-1} s^{-2}. Around oscillation frequency, the net change of 1 Hz corresponds to 1.34 ng of gas molecules adsorbed onto the crystal surface of an area of 0.196 cm^2. Gas flow into test cell was provided by N_2 calibrated

mass flow meters (MKS,179A Mass-Flo®) and RS232 controlled gas flow control unit (MKS).

As volatile compounds, dichloromethane, benzene, ethanol, 2-propanol were used for adsorption process and high-purity nitrogen gas (N_2) was used for desorption process. The change of resonance frequency of QCM was monitored with varying VOC ratio with changing flow rate of VOC/N_2. The saturated vapor pressure of volatiles were determined with Antoine equation (Lange 1979):

$$\log P^* = A - \frac{B}{T + C} \tag{6.2}$$

T is the experimental temperature in °C and A, B, C are Antoine coefficients characteristic to the selected compounds. The concentration of volatile vapor was calculated with the following equation, assuming that the vapor behaves like an ideal gas.

$$P^* = C_{(mol/L)}RT \tag{6.3}$$

The concentration in the unit of ppm was determined with the relation between the molar mass (*M*) and the density (*d*) of the VOCs (Choi et al. 2012).

$$C_{(ppm)} = C_{(mol/L)} \times \frac{M}{d} \times 10^6 \tag{6.4}$$

6.4. Results and Discussion

The aim of this work was to fabricate fibrous metal oxide deposited directly onto the QCM electrode for the detection of VOCs such as benzene, propanol, ethanol and dichloromethane. The properties of sensing material were presented for two metal oxide systems: electrospun ZnO and CeO$_2$/ZnO composite mats.

6.4.1. Fabrication and Structural Characterization of the Metal Oxide Nanofibers

Both ZnO and CeO$_2$/ZnO nanofiber mats were prepared by employing similar pathway. Initially, poly(vinyl alcohol) (PVA) and a metal salt(s) [(Zn(CH$_3$COOH)$_2$·2H$_2$O and/or Ce(NO$_3$)$_3$·6H$_2$O)] solution were dissolved in water. The resulting homogeneous solution was electrospun using horizontal set-up at 2.5 kV cm^{-1}. The fiber mats were detached from the surface of metal substrate as a free standing polymeric film. Secondly, the resulting composite fibers were converted to metal oxide fibers by controlled thermal treatment in air. Thermal degradation of the precursor fibers of PVA/metal salt(s) is presented in Figure 6.2. Three consecutive mass losses are observed at 70, 225, 425 °C for the PVA/(Zn(CH$_3$COOH)$_2$ fibers. They are attributed to the elimination of adsorbed water and the dehydration of zinc acetate, degradation of PVA, and decomposition of anhydrous zinc acetate to zinc oxide, respectively (Yang et al. 2004). On the other hand, the thermal decomposition of the PVA/(Zn(CH$_3$COOH)$_2$/Ce(NO$_3$)$_3$ fibers showed four mass losses. In addition to the mass losses given above, the loss of coordinated water in the hydrate of cerium nitrate (Shih et al. 2010) and zinc acetate accompained by the degradation of PVA. Further mass loss was not observed beyond 450 °C indicating the formation of CeO$_2$/ZnO. Therefore, the calcination temperature was increased and fixed at 500 °C, the condition under which the removal of polymer is guaranteed.
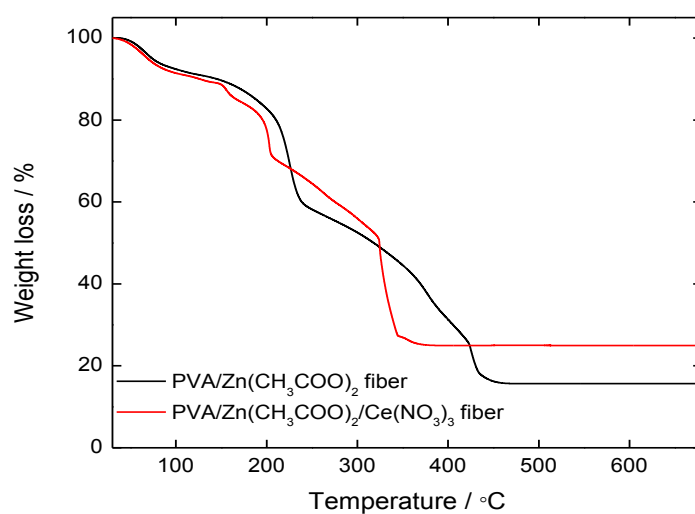
Figure 6.2. TGA termograms of $PVA/(Zn(CH_3COOH)_2$ and $PVA/(Zn(CH_3COOH)_2/Ce(NO_3)_3$ fibers

Experimentally measured metal oxide contents were 16 and 25 % for ZnO and CeO_2/ZnO systems, respectively. Theoretical contents of the remaining oxide residues can be calculated from the initially added metal salt(s) to the electrospinning solution assuming complete conversion to the corresponding oxide structure. The theoretical contents were listed in the second column of Table 6.1. Surprisingly, experimentally measured metal oxide content was found to be higher than the theoretical calculation. This discrepancy might be due to the formation of carbonaceous species present on the surface of fibers from thermal treatment of the polymeric component.

Table 6.1. Percent compositions and surface area characteristics of the metal oxide fibers

Sensing material	$ZnO+CeO_2$[a] (wt %)	$ZnO+CeO_2$[b] (wt %)	BET surface area ($m^2\,g^{-1}$)	Pore volume ($cm^3\,g^{-1}$)	Pore size (nm)	Crystallite size[c] (nm)
ZnO fiber	16	14	10	0.05	19	15
CeO_2/ZnO fiber	25	20	33	0.11	15	9

[a]Measured with TGA. [b]Theoretical content. [c]Calculated from the Scherrer equation.

102

Figure 6.3 shows XRD pattern of the metal oxide fibers obtained after calcination of PVA/(Zn(CH$_3$COOH)$_2$·2H$_2$O and/or Ce(NO$_3$)$_3$·6H$_2$O. In the presence of cerium nitrate, the diffractogram confirms the formation of a mixed phase of cubic fluorite structure of CeO$_2$ (JCPDS card no. 81-0792), along with hexagonal wurtzite structure of ZnO (JCPDS card no. 79-0207). The size of the crystallites estimated by the Scherrer equation (Klug and Alexander 1974a) from the (101) reflection was 15 nm for ZnO and 9 nm for CeO$_2$/ZnO fibers, respectively. The elemental composition of the calcined fibers was also elucidated using EDX analysis which supported the XRD results. (Figure 6.4) The composition of the fibers was mainly based on the corresponding metal and oxygen.

Figure 6.5 presents SEM micrographs and diameter distributions of ZnO and CeO$_2$/ZnO fibers after calcination. The diameter of the pre-calcined fibers of PVA/zinc acetate and PVA/zinc acetate/cerium nitrate were 315 ± 95 and 270 ±70 nm, respectively. The addition of cerium nitrate resulted in reduction of the fiber diameter in comparison to the PVA/zinc acetate fiber. This can be explained by the increase of charge density upon addition of the ceria salt. A higher elongation force leads to obtain thinner fibers due to repulsion of the charges on the jet. Upon calcination at 500 ºC in air, ZnO and CeO$_2$/ZnO fibers were obtained while the integrity of fibers is preserved. The diameter of the fibers decreased to 160 ±55 nm for ZnO and 80 ±30 nm for CeO$_2$/ZnO fibers as a result of removal of the carrier polymer and crystallization of the metal oxide phases.
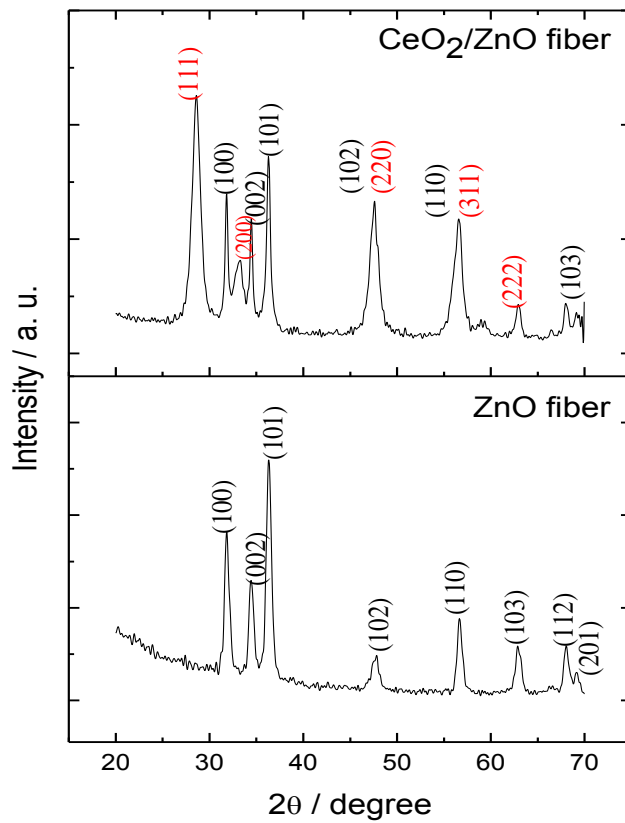
Figure 6.3. XRD patterns of CeO$_2$/ZnO and ZnO fibers
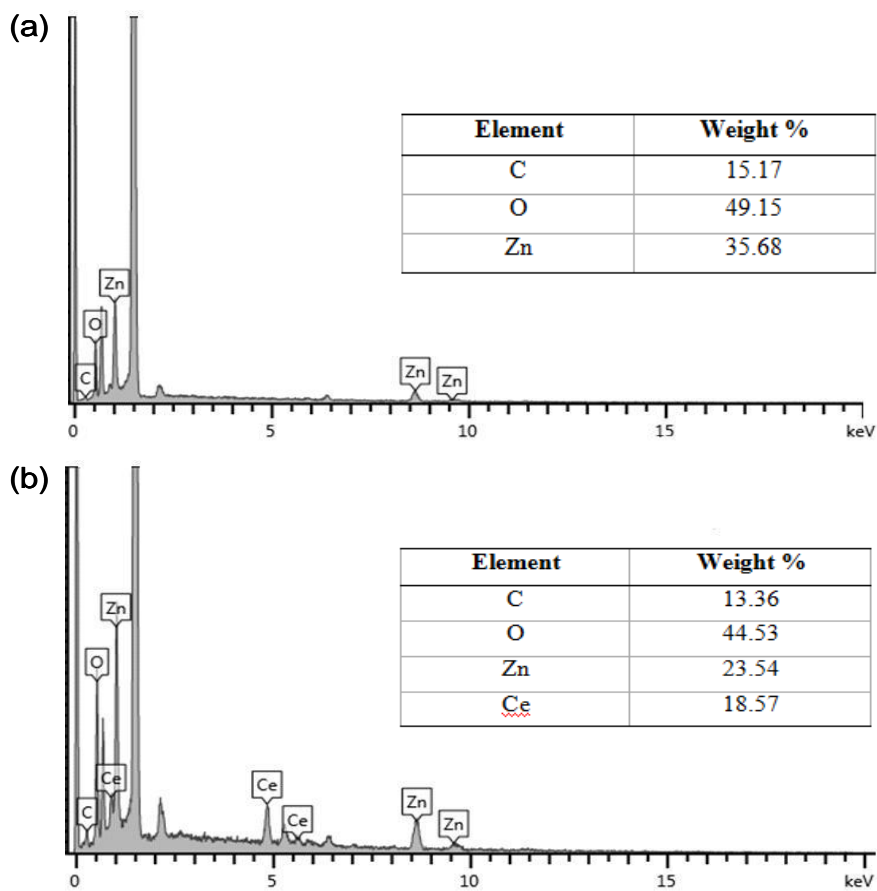
Figure 6.4. EDX spectra of electrospun (a) ZnO and (b) CeO$_2$/ZnO fiber
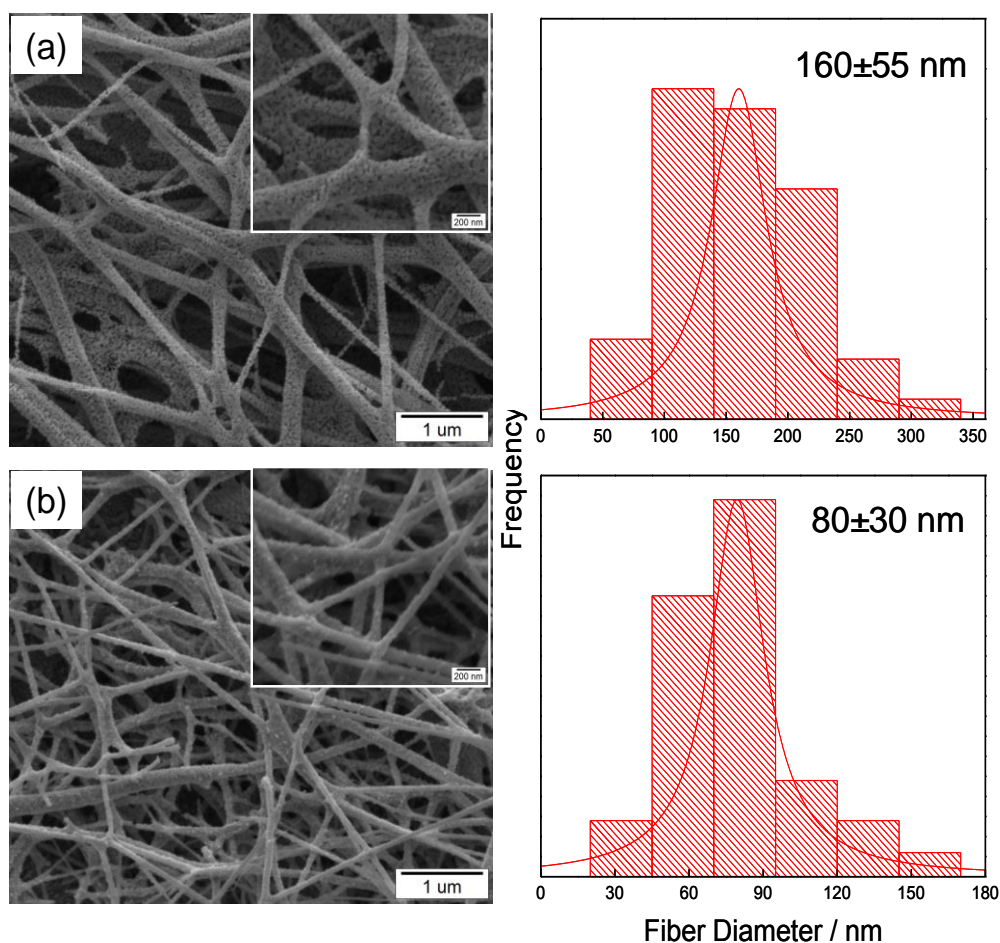
Figure 6.5. SEM micrographs and diameter distributions of (a) ZnO and (b) CeO$_2$/ZnO fiber

BET analysis provides surface area, pore volume and pore diameter of the calcined fibers (Table 6.1). The specific surface area was found to be 10 and 33 m^2 g^{-1} for ZnO and CeO$_2$/ZnO fibers, respectively. ZnO has large pore size, its surface area and pore volume is small, which indicated that the porosity in this structure is not very high. The addition of cerium salt reduces the size of ZnO crystallites and pore size. As a result, the surface area and porosity are relatively increases.

6.4.2. Sensing Properties of Metal Oxide Nanofibers

Here, we examined the sensing feature of both ZnO and CeO$_2$/ZnO systems. These oxide-based nanofiber mats were readily developed on the surface of QCM electrode and used as VOCs sensor. We have also investigated the effect of CeO$_2$ on the sensing activity of the ZnO nanofiber mats toward a representative VOCs, benzene

vapor at room temperature. Figure 6.6a shows a typical adsorption/desorption characteristics of ZnO and CeO$_2$/ZnO fibers. The QCM frequency counter is set to '0' Hz as the starting point when N$_2$ gas is sent through the QCM cell with 1000 sccm. In order to observe reproducibility and sensitivity of the fibrous membrane coated QCM sensors, N$_2$ and wet N$_2$ have been sent consecutively in 200 s periods. The change in the resonance frequency of QCM was found to be proportional to the mass of the analyte adsorbed onto QCM. This sensor system showed a stable signal with almost no hystresis after the first two cycles. The QCM frequency signals exhibited maxima at 116 Hz and 147 Hz for CeO$_2$/ZnO and ZnO fibers, respectively.

Panel b and c of Figure 6.6 display the changes in frequency shift of CeO$_2$/ZnO and ZnO fibers coated QCM crystals measured at different concentrations of benzene vapor. In Figure 6.6b, the level of wet N$_2$ was increased and subsequently decreased by 200 sccm steps with a time interval of 200s. The response of sensor to benzene vapor increased gradually with increasing analyte concentrations. For the linear responses of CeO$_2$/ZnO and ZnO fibers, analogously, the wet N$_2$ level was increased by 20 sccm for equal time intervals of 5 s. (Figure 6.6c) The frequency shift of the QCM sensor was dependent on the analyte concentration and exhibited a linear increase with benzene concentrations. The regression coefficients were 0.984 and 0.998 for CeO$_2$/ZnO and ZnO fibers, respectively.

Langmuir adsorption isotherm model has been frequently used (Baleanu et al. 2011, Demir et al. 2011, Horzum et al. 2011, Okur, Ceylan, et al. 2012, Okur, Uzar, et al. 2012) for various gases such as humidity on organic or inorganic films to describe adsorption kinetics. According to this model, the rate of surface reaction to form a monolayer on the surface is given with the following equations:

$$\frac{d\theta}{dt} = k_a(1-\theta)C - k_d\theta$$

(6.5)
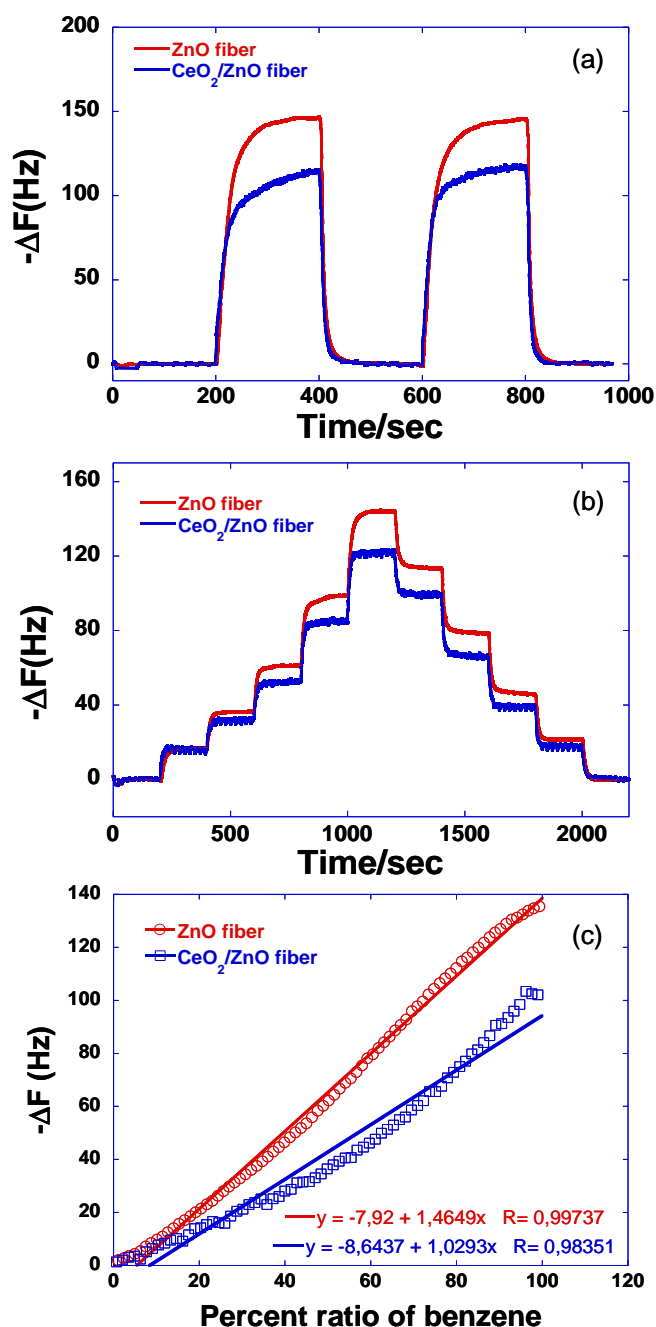
Figure 6.6. (a) The two cycles of QCM responses against benzene vapor as a function of time. (b) The step responses for adsorption and desorption of benzene with CeO$_2$/ZnO and ZnO nanofiber coated QCM. (c) The linear adsorption responses as a function of percent ratio of benzene flow

θ is a unitless quantity, which express the fraction of surface coverage, C is the gas concentration in the air, k$_a$ and k_d are the adsorption and desorption constants, respectively. Integration of Equation 6.5 leads to:

$$\theta(t) = K'(1 - e^{-k_{ads}t}) \qquad (6.6)$$

where k_{ads} is the inverse of the relaxation time and K' is the association constant defined as following:

$$K' = \frac{k_a C}{k_a C + k_d} \text{ and } k_{ads} = k_a C + k_d \qquad (6.7)$$

QCM has been used to measure the fractional coverage as a function of time during the adsorption of VOC molecules by ZnO or CeO$_2$/ZnO fibers, while the increase in the frequency shift reflects the molecular mass uptake or loss. Thus, the difference between the oscillation frequency shift (ΔF) of coated and uncoated QCM is directly proportional to the adsorbed mass of VOC molecules. The relationship between the surface adsorption kinetics and frequency shift (ΔF) of QCM can be expressed as following:

$$\Delta F(t) = \Delta F_{max} \ K' \ (1 - e^{-k_{ads}t}) \qquad (6.8)$$

Using Sauerbrey relation, ($\Delta m = -(1.34 \text{ng/Hz}) \Delta F$), the time dependent variation of mass of the adsorbed VOC molecules on the ZnO or CeO$_2$/ZnO fibers' surface, Δm_t can be defined as following:

$$\Delta m_t = \Delta m_\infty (1 - e^{-t/\tau}) \qquad (6.9)$$

$$\tau^{-1} = k_a \times C \left[\text{VOC molecules} \right] + k_d \qquad (6.10)$$

Δm_∞ is the maximum amount of adsorbed VOC molecules on the surface for $t \to \infty$ and τ is the relaxation time. Figure 6.7 shows the least square fit (solid line) using the Langmuir adsorption isotherm model given in Equation 6.9 for the adsorption parts of the data for 456 ppm benzene concentration. The values of Langmuir constants were obtained from the least square fit to the Equation 6.9 and are given in Table 6.2. The response and recovery time of CeO$_2$/ZnO fibers were found to be 62 s and 18 s, and they were 55 s and 20 s for ZnO fibers, respectively. A faster response time of ZnO fibers can be attributed to the surface characteristics correspondingly higher available active sites for sensing the target analyte.
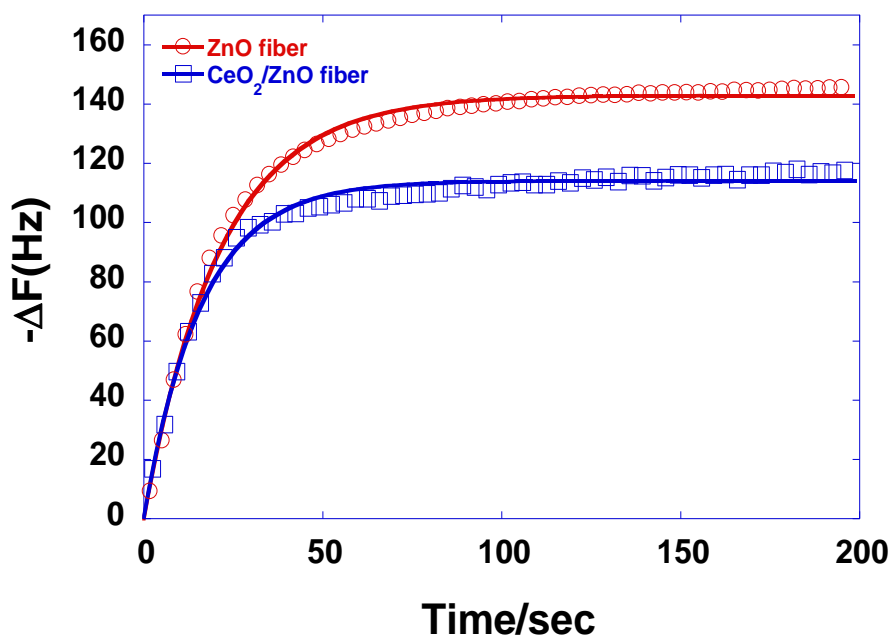
Figure 6.7. Least square fit (solid lines) using the Langmuir adsorption isotherm model for 456 ppm benzene concentration

Table 6.2. The values obtained using the Langmuir adsorption isotherm model for 456 ppm benzene concentration

	ZnO fiber	CeO$_2$/ZnO fiber
Δm_∞ (ng)		
	153	115
τ (s)		
	23	16
k_a (M^{-1} s^{-1})	93	81
k_d (s^{-1})	0.00127	0.00111
Response time (s)	55	62
Recovery time (s)	20	18
Chisq	4299	17170
R	0.999	0.992

The comparatively longer recovery time of ZnO mat can be a consequence of the higher amount of benzene molecules adsorbed to its available active surface sites. Although the flux of gas propogation through the mats is fixed, ZnO catches higher

amount of molecules so that its desorption from the surface accordingly takes longer time as compared to CeO_2/ZnO system.

The possible interactions between benzene vapor and metal oxide fiber surface were identified by FTIR spectroscopy. Figure 6.8 shows FT-IR spectra of the ZnO and CeO_2/ZnO fibers before and after benzene vapor treatment.
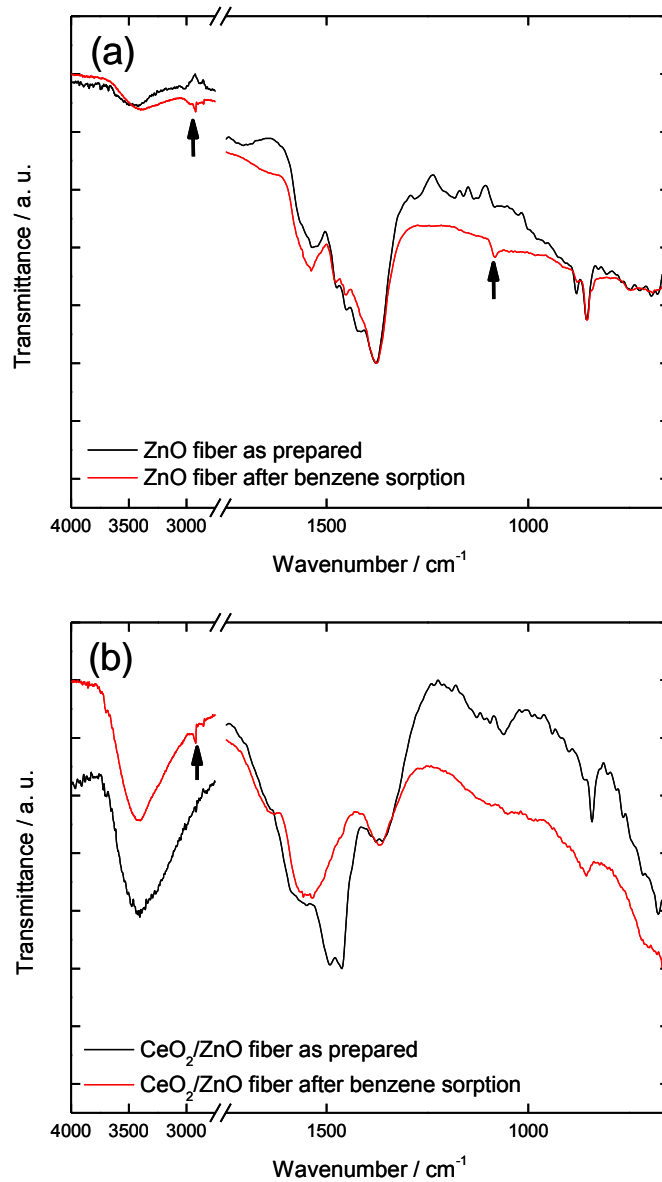
Figure 6.8. FTIR spectra of (a) ZnO fibers and (b) CeO_2/ZnO fibers, as prepared (black curve) and after benzene vapor treatment (red curve)

The broad absorption at around 3460 cm^{-1} is attributed to the presence of surface hydroxyl groups. The bands in the 3400 cm^{-1} and 1360-1475 cm^{-1} are assigned to Ce-O modes (Mokkelbost et al. 2004). (Figure 6.8b) The increase in the intensity of the broad band between 3000-3800 cm^{-1} originates from the vibration mode of CeO$_2$. After benzene sorption, both spectra show newly formed absorption signals at 2920 cm^{-1} and 1083 cm^{-1}, which may be attributed to the physisorption of benzene onto the fibers' surface.

The frequency shift of the CeO$_2$/ZnO and ZnO fiber coated QCM sensor upon exposure to benzene, propanol, ethanol and dichloromethane vapor were measured. The metal oxide fiber coated QCM sensors showed different response curves for each of the VOC depending on their concentration. The characteristics of the volatile substances are listed in Table 6.3.

Table 6.3. Properties of the volatile organic compounds

VOCs	Molar Mass (g mol^{-1})	Density (g cm^{-3})	Saturated vapor pressure[a] (atm)	Concentration (ppm)
Benzene	78.11	0.8740	0.125	456
Dichloromethane	84.93	1.3250	0.560	1474
Ethanol	46.07	0.7890	0.078	187
Propanol	60.10	0.7850	0.056	176

[a]The vapor pressure at 25 °C was calculated from Antoine equation.

The change of frequency shift depending on unit change of concentration is defined as sensitivity of the sensor (Islam et al. 2005). To make more accurate comparison, the sensitivity of the CeO$_2$/ZnO and ZnO fiber coated sensor to benzene, propanol, ethanol and dichloromethane vapor is presented in Figure 6.9. Both ZnO and CeO$_2$/ZnO systems showed sensitivity to the VOCs employed; however, ZnO fibers

were found to be more effective although it provides smaller surface area compared to CeO$_2$/ZnO. In comparison with the CeO$_2$/ZnO fibers, the better sensing performance of ZnO fibers could be attributed to the crystal structure of the oxidic systems. ZnO has hexagonal wurzite structure with zinc ions surrounded by tetrahedra of oxygen ions. This tetrahedral coordination results in tetrahedral symmetry and accordingly spontaneous polarity along the hexagonal axis. The polar Zn-O bonds arise charge contrast between zinc and oxygen planes (Jagadish and Pearton 2006) where Zn atoms are partially positive. Thus, lone pairs on the alcoholic compounds tend to be attracted toward the positively charged metal atoms.
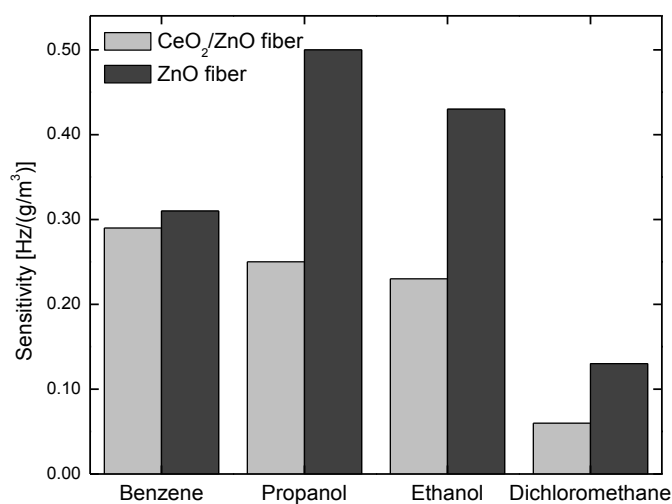
Figure 6.9. Sensitivity of the CeO$_2$/ZnO and ZnO fiber coated sensor to benzene, propanol, ethanol and dichloromethane vapor

On the other hand, CeO$_2$ that has fluorite crystal structure does not have polarity as much as ZnO does. This is because the addition of CeO$_2$ into ZnO structure does not seem to be effective in sensing applications although it provides larger surface area (Table 6.1). The efficiency of these materials in sensing applications was not merely originated from surface area and porosity, rather, may result from the surface chemical feature of the metal oxide systems.

The sensing feature of the VOCs to the nanofiber-coated QCM is based on adsorption/desorption mechanism. This pair of process is a surface phenomenon; therefore, surface chemistry of the sensing materials must be carefully examined. Since the metal oxide fibers were obtained by calcination of PVA and metal precursor(s), the surface of the fibers is covered by different species. For example, carbonaceous species

may be present left over from the thermal degradation of PVA. When polymeric component undergoes degredation at 500 °C, the formation of carbon rich organic residue on the fiber surface is highly possible. Moreover, the surface of oxides is inevitably covered with a thick layer of water molecules with different structure and mobility. The first layer of molecules is strictly bound to the surface of metal oxide surface. The interaction of the molecules decreases and correspondingly their mobility increases radially outward from the metal oxide surface (Nagao 1971b, Demir, Koynov, et al. 2007). Yet, the presence of both surface species (carbonaceous and surface hydroxyls) speculated here in fact was revealed by vibrational spectroscopy. The sensitivity of the oxide surfaces to benzene may be explained by the interaction of surface carbonaceous species with benzene molecules through nonpolar interactions. On the other hand, the polar oxidic surface feature may better associate with polar organic compounds for instance alcohols.

The sensing ability of the nanomaterials can also be roughly viewed from another perspective. The liability of the VOCs toward interaction with surface metal atoms can be explained based on the Lewis acid-base pairing. Higher oxygen vacant sites in wurzite crystal structure of ZnO fibers refer to deficiency of negative charge, therefore; ZnO can be considered as Lewis acid (Hu et al. 2013). The presence of oxygen vacancy may act as trapping centers. For example, oxygen atoms due to having two lone pairs with high electron density and the oxygen atom can donate electron pairs, thus alcohols act as Lewis base. ZnO shows a higher sensitivity compared to CeO_2/ZnO regardless of the compounds. On the other hand, the fibers coated sensor show low sensitivity to dichloromethane. Because of the electronegative chlorine atoms in dichloromethane, the molecule acts as weak base making Zn atom difficult to accept an electron pair from the base.

6.5. Conclusion

CeO_2/ZnO and ZnO based nanofibers as sensitive coatings were successfully positioned on the electrode of QCM via electrospinning and subsequent calcination. Their sensing abilities based on the VOCs (benzene, propanol, ethanol, and dichloromethane) adsorption/desorption behaviors were examined using a QCM technique. Independent of the chemistry of metal oxide, the fiber mats respond to all

VOCs employed in this study. However, ZnO fibrous mat exhibited better performance than CeO$_2$/ZnO fibers most probably due to the crystal structure and presence of higher oxygen vacancies. The sensing properties of CeO$_2$/ZnO and ZnO fibers coated QCM were particularly demonstrated for the detection of benzene. The response time was found to be 55 s for ZnO fibers. On the other hand, CeO$_2$/ZnO fibers showed response within 62 s. The sensitivity of the metal oxide surfaces to benzene can be explained by hydrophobic interaction with the surface carbonaceous species. Moreover, ZnO fiber mat seemed to be particulary sensitive to the alcoholic type compounds based on Lewis acid-base pairing. Taking advantage of various fascinating features of the electrospun metal oxide nanofibrous mat, the coated QCM sensors offer easy handling, high sensitivity, as well as good reproducibility. The preparation method of QCM coating is versatile and can also be used to fabricate several active nanofibrous materials. We envisaged that this strategy enables efficient design and development of other QCM coatings toward undesirable volatile organic compounds.

CHAPTER 7

HIERARCHICALLY STRUCTURED METAL OXIDE/SILICA NANOFIBERS BY COLLOID ELECTROSPINNING

7.1. Abstract

We present herein a new concept for the preparation of nanofibrous metal oxides based on the simultaneous electrospinning of metal oxide precursors and silica nanoparticles. Precursor fibers are prepared by electrospinning silica nanoparticles (20 nm in diameter) dispersed in an aqueous solution of poly(acrylic acid) and metal salts. Upon calcination in air, the poly(acrylic acid) matrix is removed, the silica nanoparticles are cemented, and nanocrystalline metal oxide particles of 4–14 nm are nucleated at the surface of the silica nanoparticles. The obtained continuous silica fibers act as a structural framework for metal oxide nanoparticles and show improved mechanical integrity compared to the neat metal oxide fibers. The hierarchically nanostructured materials are promising for catalysis applications, as demonstrated by the successful degradation of a model dye in the presence of the fibers.

7.2. Introduction

Due to their large ratio of surface area to volume and interconnected porosity, metal oxide meshes have been proposed for applications in catalysis, energy storage, and sensors (Choi et al. 2009, Fierro 2006, Kim and Rothschild 2011). Various bottom-up approaches—such as vapor–liquid–solid (VLS) (Valcarcel et al. 1998), and vapor–solid (VS) (Chen et al. 2004) growth—and top-down techniques—such as nanocarving (Yoo et al. 2006) and electrospinning (Li et al. 2003) ⸺have been described. Among these techniques, electrospinning is probably the most versatile, because it allows the fabrication of fibrous mats from a wide variety of both organic and/or inorganic

materials (Huang et al. 2003, Sigmund et al. 2006). Moreover, it allows the control over the diameter, morphology, porosity, alignment, and composition of the resulting fibers (Fridrikh et al. 2003, Theron et al. 2004).

Calcination of electrospun mats obtained from metal oxide precursors is a commonly used approach because of its facility and potential for upscaling. The calcination process is usually applied to mixtures of polymers/metal oxide precursors and it is based on an oxidative conversion of the polymeric component by heat treatment. There are many successful examples in literature for the fabrication of inorganic fibers by calcination of precursor materials prepared by sol–gel (Choi et al. 2003, Hansen et al. 2011, Ma et al. 2011, Panels and Joo 2006, Sakai et al. 2012, Seol et al. 2009), polymer-based sol–gel processes (Ding et al. 2003, Kim et al. 2010, Shao et al. 2002, Shi et al. 2009), or from electrospinning of polymer dispersions in the presence of ex-situ formed colloids (Chen et al. 2009, Friedemann et al. 2012, Kanehata et al. 2007, Lim et al. 2006, Zhang et al. 2011). While the polymeric component undergoes degradation, metal oxide crystals nucleate and grow upon increase of the temperature (Li, Meyer, et al. 2005, Lu et al. 2006).

In the electrospinning of inorganic precursor, one has to take into account that the calcination leads almost automatically to a shrinkage of the fibers since the polymer template is removed. After calcination, the nanofibers are usually more brittle (Horzum et al. 2011) due to their thinner section and the internal stress generated by the shrinkage. Therefore, an additional material that is not mechanically or chemically affected by the calcination process needs to be incorporated in the fibers during the electrospinning.

The recently reviewed electrospinning of colloids (Crespy et al. 2012) has been explored for the fabrication of metal or metalloid oxide fibers. For instance, silica (Friedemann et al. 2012, Lim et al. 2006), and titania (Wesselt et al. 2011) nanoparticles were embedded in polymer fibers by electrospinning a solution of polymer template in the presence of a dispersion of the particles. Recently, the electrospinning of a zinc powder/titanium isopropoxide/poly(vinyl acetate) mixture was reported (Kanjwal et al. 2010). The precursor fibers were calcinated in air and the subsequent hydrothermal treatment of the resulting fibers in bis(hexamethylene)triamine and a zinc nitrate hexahydrate solution yielded continuous TiO_2 fibers decorated with ZnO branches. The ZnO particles in the TiO_2 fibers seeded the growth of ZnO branches perpendicular to the TiO_2 fibers direction. The same procedure was employed to form ZnO-branched

Co$_3$O$_4$ (Kanjwal et al. 2011) and ZnO-branched ZnO (Kanjwal et al. 2012) fibers. Although the synthesis of silica-supported metal oxide nanocomposites has been previously reported (Zhao et al. 2010, Tang et al. 2011, Strunk et al. 2011), their fabrication by colloid-electrospinning to obtain nanofibers is a new strategy. Our concept allows the advantageous combination of interesting properties inherent to both nanoparticles (high surface area) and meshes (porous structure and facile separation from the reaction media). Furthermore, the incorporation of silica nanoparticles in the composite fibers significantly improves the mechanical integrity of the nanofibers. The generality of the concept is demonstrated by taking two different metal oxides, namely CeO$_2$ and LiCoO$_2$ as models for simple and binary oxides, respectively. The catalytic activity of the composite nanofibers was also investigated.

7.3. Experimental Section

7.3.1. Materials

Cerium(III) nitrate hexahydrate (Fluka, $\geq$99.0%), lithium hydroxide (Aldrich, 98%), cobalt(II) hydroxide (Aldrich, 95%), poly(acrylic acid) (PAA, $M_w \approx$ 450,000 g mol^{-1}, Polysciences Inc.), colloidal silica (average diameter: 20 nm, BET surface area: 140 m^2 g^{-1}, 34 wt% suspension in H$_2$O, Sigma-Aldrich), and rhodamine B (Merck) were all used as received without any further purification. Demineralized water was used throughout the study.

7.3.2. Preparation of the Electrospinning Solutions

The metal salt(s), Ce(NO$_3$)$_3$·6H$_2$O (780 mg, 1.8 mmol; and 390 mg, 0.9 mmol) or LiOH (21.5 mg, 0.9 mmol) and Co(OH)$_2$ (83 mg, 0.90 mmol), were added to a 7.5 wt% solution of PAA (0.870 g), and the mixture was stirred for 2 h at room temperature.

For the fabrication of metal oxide/silica fibers, the colloidal silica was dispersed in 4.0 g of the PAA/metal salt solution. The weight ratio of PAA:SiO$_2$ was fixed as 1:1.

Two different $Ce(NO_3)_3 \cdot 6H_2O$ concentrations with respect to the amount of silica (mole ratios Ce:Si) were used: 0.06:1.00 and 0.12:1.00 (mole ratios).

7.3.3. Fabrication of the Nanofibers

The viscous solutions of PAA/metal salt precursor or the dispersions of PAA/metal salt precursor/SiO_2 were loaded in a plastic syringe connected with silicon rubber tubing. The electrospinning experiments were carried out with a commercial platform (ES1a, Electrospinz) covered with a polycarbonate box placed for safety and to avoid disturbances from air convection. The positive electrode was applied to the spinneret and an aluminum foil was used as counter electrode. The flow rate of the polymer solution was adjusted by a syringe pump (Bioblock, Kd Scientific). The optimum electrospinning parameters are presented in Table 7.1. PAA/SiO_2, PAA/SiO_2/$Ce(NO_3)_3$, PAA/$Ce(NO_3)_3$, and PAA/SiO_2/LiOH/$Co(OH)_2$ fibers were calcinated under air in a muffle oven (Nabertherm Controller P330 LT 5/13) at 600 ºC (room temperature to 600 ºC at a rate of 4 ºC min^{-1}; plateau of 2 h at 600 ºC). PAA/LiOH/$Co(OH)_2$ fibers were calcinated at 400 ºC for 5 h with a rate of 4 ºC min^{-1}.

Table 7.1. Optimized electrospinning parameters (tip-to-collector distance fixed at 14 cm)

Metal oxide	Precursor	Electric field [kV cm^{-1}]	Flow rate [mL h^{-1}]
CeO_2	PAA/$Ce(NO_3)_3 \cdot 6H_2O$	0.71	2
CeO_2/SiO_2	PAA/$Ce(NO_3)_3 \cdot 6H_2O$/SiO_2	0.71	2
SiO_2	PAA/SiO_2	0.36	1
$LiCoO_2$	PAA/LiOH/$Co(OH)_2$	1.43	2
$LiCoO_2$/SiO_2	PAA/LiOH/$Co(OH)_2$/SiO_2	0.71	1

7.3.4. Characterization Methods

The fibers were electrospun onto silicon wafers for morphological observations by scanning electron microscopy (SEM) in a LEO 1530 Gemini microscope (Zeiss). To localize the metal oxide nanoparticles on the fibers, high-resolution SEM micrographs were captured using a Hitachi SU8000 microscope. The diameter of fibers and particle size distributions were calculated from SEM micrographs using the Fiji/ImageJ software. X-ray diffraction pattern (XRD) were recorded in a Philips PW 1820 diffractometer using $Cu_{K\alpha}$ radiation ($\lambda = 1.5418$ Å). Thermogravimetric analysis (TGA) was studied by a Mettler Toledo 851 thermobalance. The specific surface area of the calcinated fibers was determined from nitrogen adsorption using a Micromeritics Gemini V instrument. The surface area was calculated according to the Brunauer–Emmett–Teller (BET) methodology (five point, $0.05 < P/P_0 < 0.3$). The samples were degassed at 400 ºC for 6 h in vacuum prior to the measurements.

The photocatalytic degradation of rhodamine B (Merck) in the presence of pure CeO_2, CeO_2/SiO_2, and SiO_2 fibers was carried out in a polystyrene plate (Corning) under UV light irradiation. For the catalysis experiments, the fiber catalyst (2.0 mg) was added to an aqueous solution of rhodamine B (1.5 mL, 5 ppm) and stirred continuously. At certain time intervals, photoluminescence (PL) emission spectra of the dye solution with the fiber mats were registered in top-mode on a Tecan Infinite M100 plate reader using an excitation wavelength of 500 nm.

7.4. Results and Discussion

The preparation of silica-supported metal oxide fibers by colloid electrospinning and subsequent controlled thermal treatment is presented for two systems: CeO_2, as a model for a simple metal oxide, and $LiCoO_2$, as a model for a binary system. Silica nanoparticles were selected as cheap but robust structural framework for the final materials. Initially, poly(acrylic acid) (PAA) and a metal salt (either $Ce(NO_3)_3 \cdot 6H_2O$ or LiOH and $Co(OH)_2$) were dissolved in water, and the homogeneous aqueous polymer solution was electrospun. In a second step, the resulting mats were converted to metal

oxide fibers by thermal treatment in a controlled environment. A schematic diagram for the fabrication of metal oxide and metal oxide/silica fibers is depicted in Figure 7.1. In both systems, PAA was used as polymer template and binder in the fibers. PAA is a commonly used polyelectrolyte, with most of the carboxyl groups being deprotonated at neutral pH (pK_a 4–4.5) (Pradip et al. 1991), which provide the ability to coordinate metal cations.

The thermal decomposition of PAA/SiO_2 fibers measured by thermogravimetric analysis (TGA) showed two consecutive mass losses (Figure 7.2a), attributed to the elimination of adsorbed water, and to the degradation of poly(acrylic acid) (Moharram and Khafagi 2006). The three weight losses observed for the PAA/$Ce(NO_3)_3$ and PAA/$Ce(NO_3)_3$/SiO_2 fibers are consecutive to the elimination of adsorbed water, the dehydration of cerium nitrate and degradation of PAA, and the conversion of unhydrated $Ce(NO_3)_3$ to CeO_2 (at increasing temperature) (Shih et al. 2010). Since the mass of the materials remains unchanged around 600 ºC, the calcination temperature was fixed at this temperature. After calcination, the majority of the remaining residue is expected to be composed of CeO_2 and/or SiO_2. Experimentally measured and theoretical percentages of remaining residues, calculated from the initially introduced precursor assuming complete conversion to CeO_2, are listed in Table 7.2. In the presence of SiO_2 nanoparticles, the remaining material after calcination of PAA/SiO_2 fibers was higher (48%) than that of PAA/$Ce(NO_3)_3$ fibers (23%). The thermal stability of the fibers was slightly increased upon addition of SiO_2 nanoparticles with an onset of degradation temperature shifted to more than 15 ºC in the presence of silica particles.

Similarly, the thermal decomposition of the PAA/LiOH/$Co(OH)_2$ fibers occurs in three stages in the temperature range of 25–720 ºC (Figure 7.2b). The weight losses were ascribed to the removal of adsorbed water (~10%), the polymer degradation and the conversion of $Co(OH)_2$ to Co_3O_4 (56%) (Mahmoud and Al-Agel 2011), and the reaction of Co_3O_4 with the lithium salt to form $LiCoO_2$ (Carewska et al. 1995).

precursor nanofibers

metal oxide nanofibers

Δ

metal oxide / silica nanofibers

Δ

× Polymer
■ Metal salt
● Silica NP
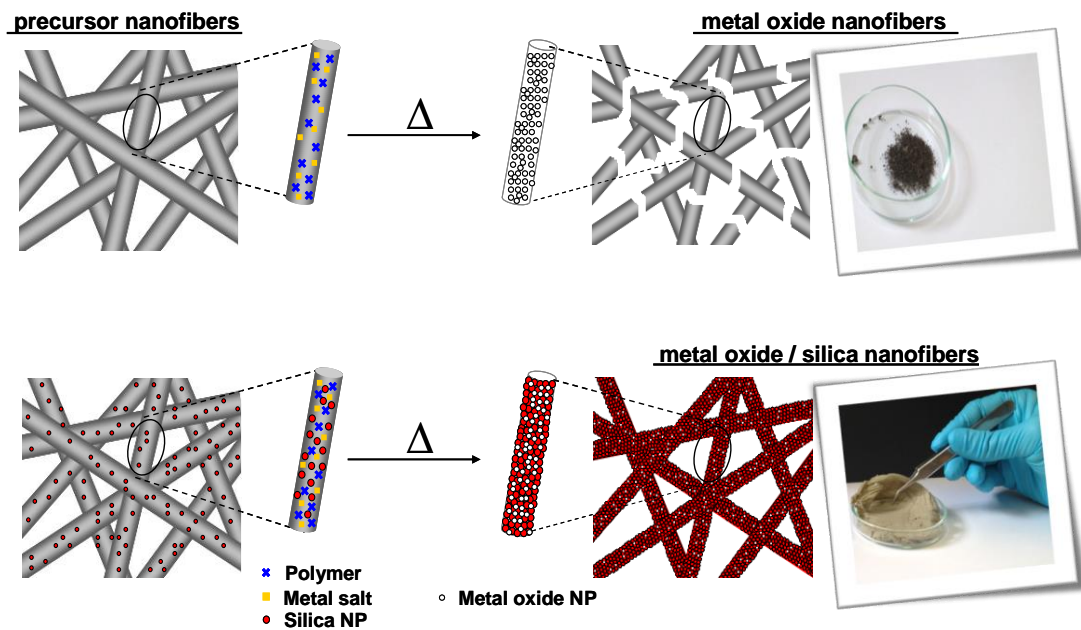
○ Metal oxide NP

Figure 7.1. Scheme of the preparation of metal oxide (top) and metal oxide/silica (bottom) fibers. The metal oxide fiber are brittle and yield a powder material whereas the nanofibrous morphology is conserved by using silica nanoparticles as structural framework
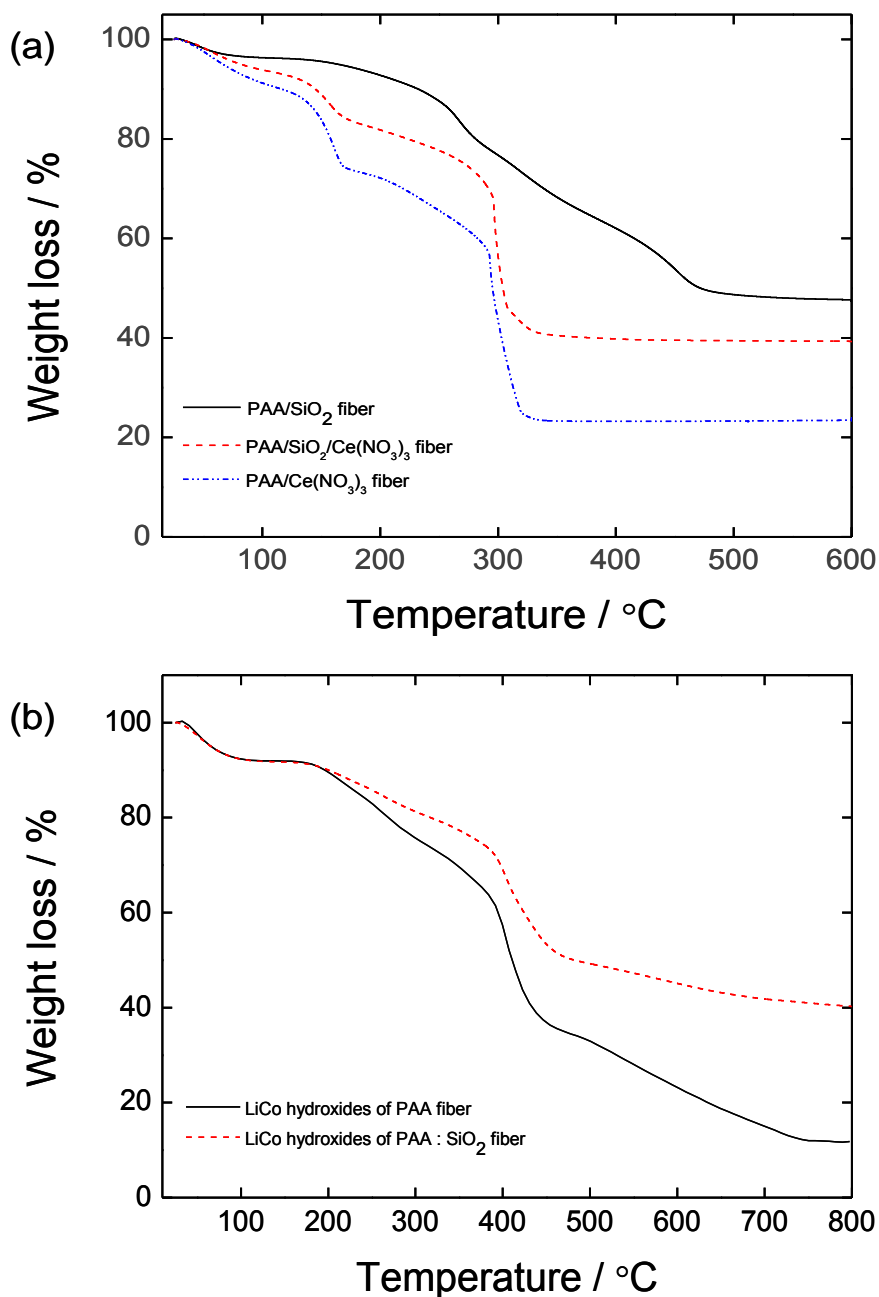
Figure 7.2. TGA thermograms of (a) PAA/SiO$_2$/Ce(NO$_3$)$_3$ and PAA/Ce(NO$_3$)$_3$ fibers, and (b) PAA/LiOH/Co(OH)$_2$, PAA/SiO$_2$/LiOH/Co(OH)$_2$ fibers.

Similar to the aforementioned results obtained for CeO$_2$, the addition of SiO$_2$ nanoparticles shifted the decomposition temperature to higher values. Indeed, the remaining mass at 600 °C for the PAA/LiCo hydroxide fibers was 23% versus 45% in the presence of 6.5 wt % of SiO$_2$. Since the degradation mechanism relies generally on

the diffusion of polymer residues formed upon increase of temperature, the nanoparticles may act as barrier for mass transport, hence improving the thermal properties of the materials. Such phenomenon was already reported by Mizuno et al. (Mizuno et al. 2012), who found that the presence of vapor-grown carbon fiber hindered the decomposition of PVA.

Table 7.2. Diameters of the fibers and percent compositions of the metal oxide/silica fibers

Fiber	d_{fiber} before calcination[a] [nm]	d_{fiber} after calcination[a] [nm]	CeO_2[b] [vol%]	$CeO_2 + SiO_2$[c] [wt%]	$CeO_2 + SiO_2$[d] [wt%]
SiO_2	540 ± 80	510 ± 80	–	48	50
CeO_2/SiO_2 (0.06/1.00)	290 ± 50	180 ± 30	6.3	40	48
CeO_2/SiO_2 (0.12/1.00)	300 ± 40	190 ± 30	12.2	33	47
CeO_2	320 ± 50	240 ± 40	100.0	23	19

Fiber	d_{fiber} before calcination[a] [nm]	d_{fiber} after calcination[a] [nm]	$LiCoO_2$[b] [vol%]	$LiCoO_2 + SiO_2$[c] [wt%]	$LiCoO_2 + SiO_2$[d] [wt%]
$LiCoO_2$	310 ± 60	190 ± 30	100.0	12	18
$LiCoO_2/SiO_2$	350 ± 80	320 ± 100	5.03	41	57

[a] measured with SEM, [b] calculated from Equation (7.2), [c] measured with TGA, [d] theoretical content.

The obtained electrospun materials were observed by SEM before (Figure 7.3a–d) and after calcination (Figure 7.3e–h). Fiber mats prepared from PAA solutions with different Ce/Si mole ratios (0.06 and 0.12) were compared with references prepared from PAA solutions containing only either $Ce(NO_3)_3$ or SiO_2.
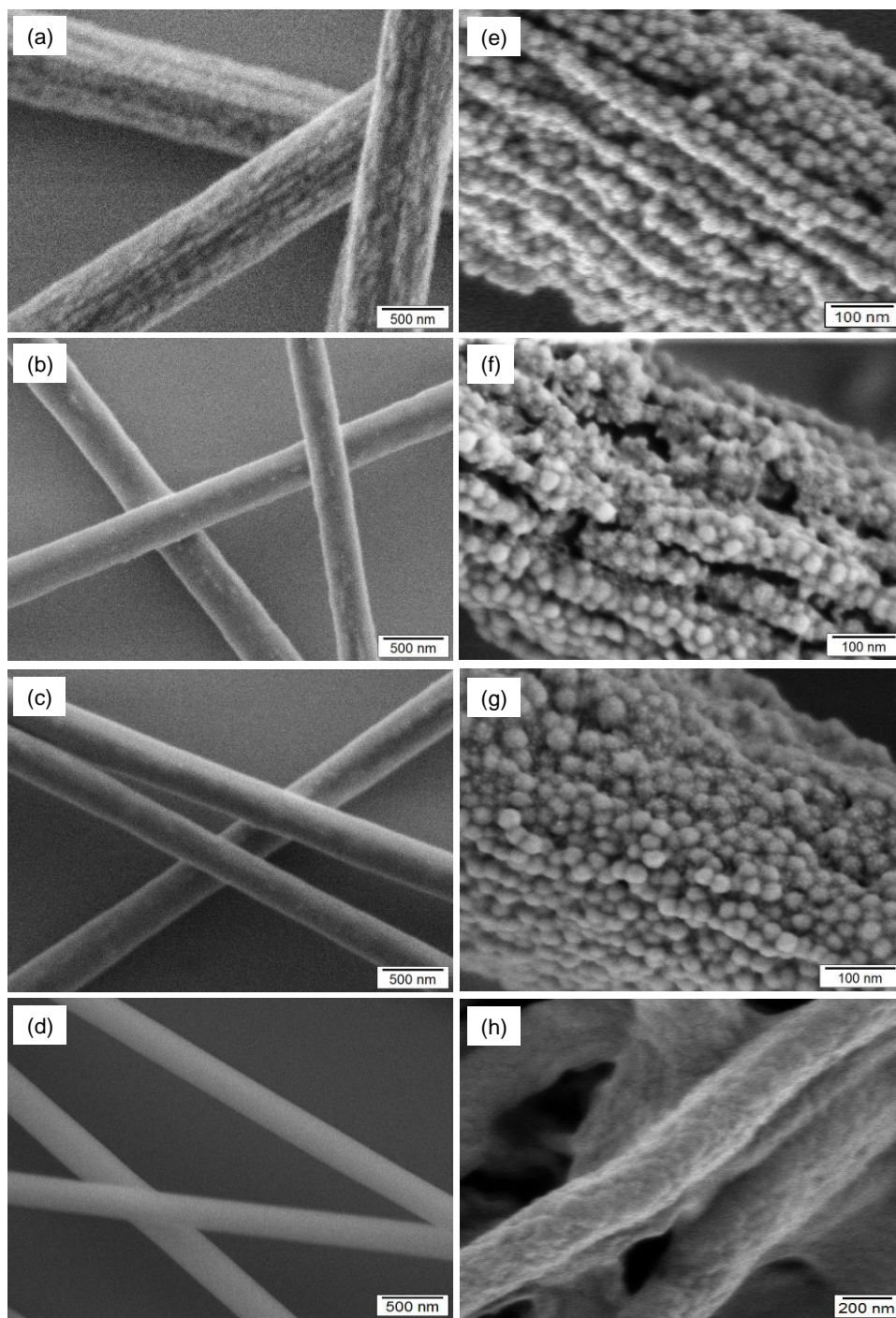
Figure 7.3. SEM micrographs of composite fibers as prepared: (a) PAA/SiO$_2$; (b, c) PAA/Ce(NO$_3$)$_3$/SiO$_2$ with Ce/Si molar ratios of 0.06 and 0.12, respectively, (d) PAA/Ce(NO$_3$)$_3$; and oxide fibers after calcination at 600 ºC: (e) SiO$_2$, (f) CeO$_2$/SiO$_2$ (0.06/1.00), (g) CeO$_2$/SiO$_2$ (0.12/1.00), (h) CeO$_2$

Silica nanoparticles were visible on the fibers, creating a rough surface. The addition of Ce(NO$_3$)$_3$ resulted in reduction of the fiber diameter in comparison to the PAA/SiO$_2$ fiber (Table 7.2), which can be explained by the increase of charge density

upon addition of the metal salt, inducing larger coulombic interactions and, therefore, higher stretching of the electrospinning jet (Zong et al. 2002). After calcination at 600 ºC, the morphology of the fibers was preserved and the diameter of the fibers decreased owing to the removal of the polymer template. The incorporation of silica nanoparticles into the metal oxide fibers increased remarkably the surface area of the electrospun mats. The specific surface area of neat CeO_2 fibers was 38 m^2 g^{-1}, whereas it increased to 161, 155, and 127 m^2 g^{-1} for SiO_2, $CeO_2/SiO_2(0.12/1.00)$, and $CeO_2/SiO_2(0.06/1.00)$, respectively.
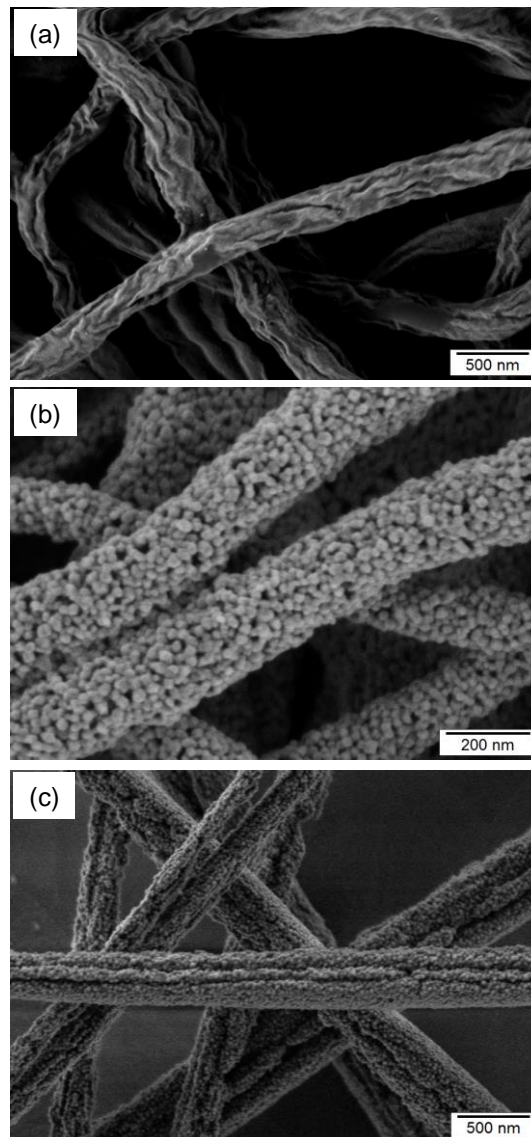
Figure 7.4. SEM micrographs of PAA/LiOH/Co(OH)$_2$ precursor fibers after calcination (a) at 300 ºC, (b) at 400 ºC and (c) PAA/LiOH/Co(OH)$_2$/ SiO$_2$ precursor fibers calcinated at 600 ºC

The hierarchy of size observed in the fibers (metal oxide crystallites < silica nanoparticles < fibers) is reflected in the hierarchy of porosity in the structure. Accordingly, there were two levels of porosity: the porosity created by the space between electrospun fibers, and the porosity of the silica particles, both contributing to the porosity of the resulting metal oxide fibers.

The morphologies of the $LiCoO_2$ and $LiCoO_2/SiO_2$ fibers are shown in Figure 7.4a–c. The $PAA/LiOH/Co(OH)_2$ fibers before calcination were continuous, smooth, and uniform, with a diameter of 310 ± 60 nm. Similar to the CeO_2 fibers, the calcination caused shrinkage of the average fiber diameter of $LiCoO_2$ to 190 ± 30 nm. $LiCoO_2/SiO_2$ fibers were clearly less brittle than neat $LiCoO_2$ fibers. Whereas the $LiCoO_2$ mat was converted to ultrafine pieces and powder (photograph on the top of Figure 7.1), the mat of $LiCoO_2/SiO_2$ (bottom image) remained intact after calcination. The non-woven could be therefore handled as single object, which was not the case for the calcinated metal oxide fibers. We investigated the effect of calcination temperature on the fiber morphology. At 300 ºC, a phase separation was observed on the surface of fibers (Figure 7.4a). The components (i.e., polymer chains, residues, and metal oxide/salt) were separated into distinct domains oriented along the surface of the fibers. This phase separation occurred uniformly on the surface along the long axis of the fiber wherein polymer-lean and polymer-rich phases were formed, indicating a spinodal decomposition. The orientation of the domains is probably a consequence of elongational electrical forces occuring during electrospinning process. When the calcination temperature was increased to 400 ºC, the fibers preserved their continuous structures and the average diameter was reduced by about 40% with narrower distribution (25%). At the same time, the nucleation and growth of $LiCoO_2$ nanoparticles occurred and the $LiCoO_2$ nanoparticles were visible on the fibers surface (Figure 7.4b). The PAA aqueous solution composed of lithium/cobalt hydroxides was basic (pH $\approx$ 9). Under this condition, surface silanols are dissociated into negatively charged oxide ($Si–O^-$) on the surface. Electrostatic repulsion between negatively charged particles resulted in stable and non-aggregated silica dispersions. In the presence of silica nanoparticles of uniform size in the fibers, homogeneously assembled continuous fibers could be formed (Figure 7.4c).

The crystallinity of the samples was studied by X-ray diffraction (XRD). Figure 7.5a shows the XRD patterns of fibers prepared with different CeO_2/SiO_2 ratios (0.06/1 and 0.12/1) after calcination at 600 °C, compared with those of SiO_2 and CeO_2 fibers.
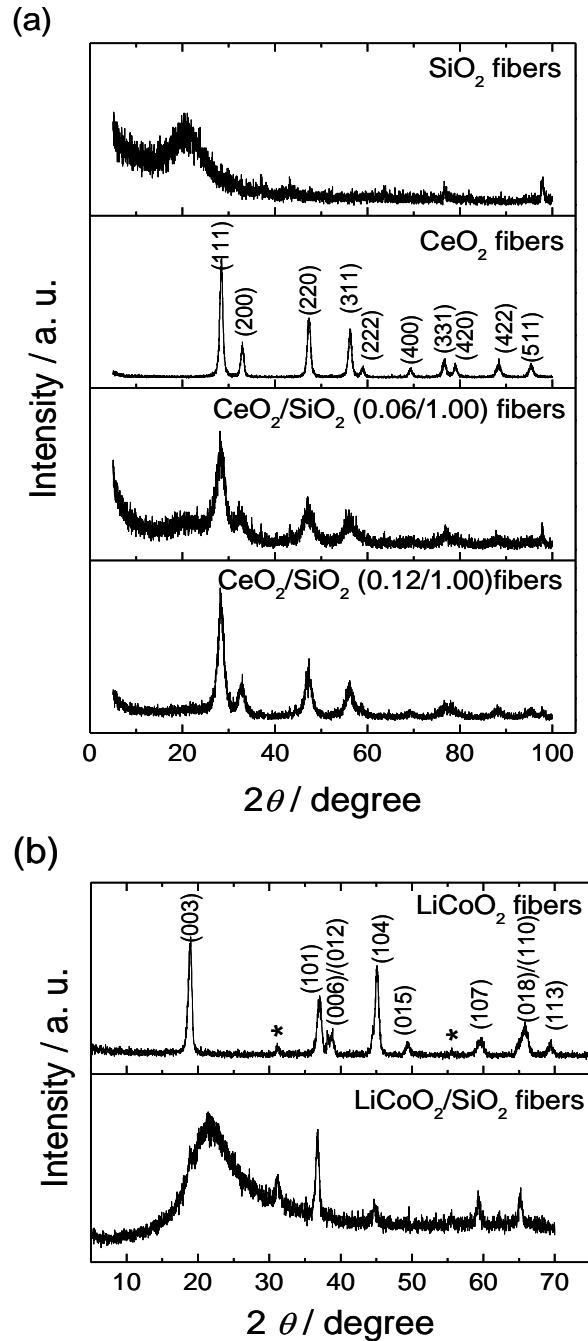
Figure 7.5. (a) XRD patterns of SiO_2 fibers (blank) and CeO_2 fibers prepared in the absence and presence of SiO_2 nanoparticles after calcination at 600 ºC; (b) XRD patterns of lithium cobalt oxide fibers prepared in the absence and presence of SiO_2 nanoparticles after calcination at 400 ºC (the stars indicate reflections of Co_3O_4)

Whereas the silica fibers displayed a typical amorphous halo, the samples containing cerium showed the characteristic reflections for cubic CeO_2 (JCPDS card No. 34-394). The increase of the amount of cerium salt resulted in sharper reflections, which correlates with the size of the crystalline domains. Under the same experimental conditions, CeO_2 fibers prepared without colloid silica showed much narrower reflections. The sizes of the crystallites estimated by the Scherrer equation (Langford and Wilson 1978), from the (111) reflection were 4, 6, and 12 nm for the CeO_2/SiO_2 (0.06/1.00), CeO_2/SiO_2 (0.12/1.00) and CeO_2 fibers, respectively. These results indicate that the size of the ceria crystallites was smaller in the presence of amorphous silica and increased with increasing amount of cerium. The change in the crystallite size can be associated with the interfacial area between the colloid and the ceria salt. Since colloidal silica provides large surface area, there may be higher number of nucleation sites compared to the fibers prepared in the absence of the colloids, so that the resulting crystallites are smaller. When the amount of cerium nitrate increased, while keeping constant the amount of the SiO_2 nanoparticles, there was no change in nucleation sites and the diameter of the particles increased.

Figure 7.5b contains the XRD patterns of the binary metal oxide fibers after calcination of $PAA/LiOH/Co(OH)_2$ in the absence and in the presence of SiO_2. In the absence of SiO_2, the diffractogram confirms the formation of $LiCoO_2$ (JCPDS card no. 44-0145), with a minor coexistence of Co_3O_4 (JCPDS card no. 42-1467). In the fibers formed in the presence of SiO_2 nanoparticles, the Co_3O_4 phase becomes more significant, which may be ascribed to the formation of lithiated Co_3O_4 and/or nonstoichimetric lithium cobalt oxide. The coexistence of Co_3O_4 and the formation of nonstoichiometric lithium cobalt oxides have been often reported in solid-state reaction methods from metal salts (Antolini 1997, 2004, Rossen et al. 1993). A crystallite size of 14 nm was estimated by the Scherrer equation from the most intense (003) reflection for the $LiCoO_2$ obtained without SiO_2. The crystallite size is consistent with the particle size estimated statistically from SEM micrographs (21 ± 5 nm, Figure 7.4b).

The backscattered electrons detection mode of the SEM was used to localize $LiCoO_2$ nanoparticles among the SiO_2 (Figure 7.6), thanks to the atomic number contrast between both type of particles (SiO_2, and $LiCoO_2$). $LiCoO_2$ nanoparticles with a diameter of 12 ± 3 nm could be identified, being uniformly dispersed among the SiO_2 particles in the fiber. The experimental and theoretical volume percents of the particles,
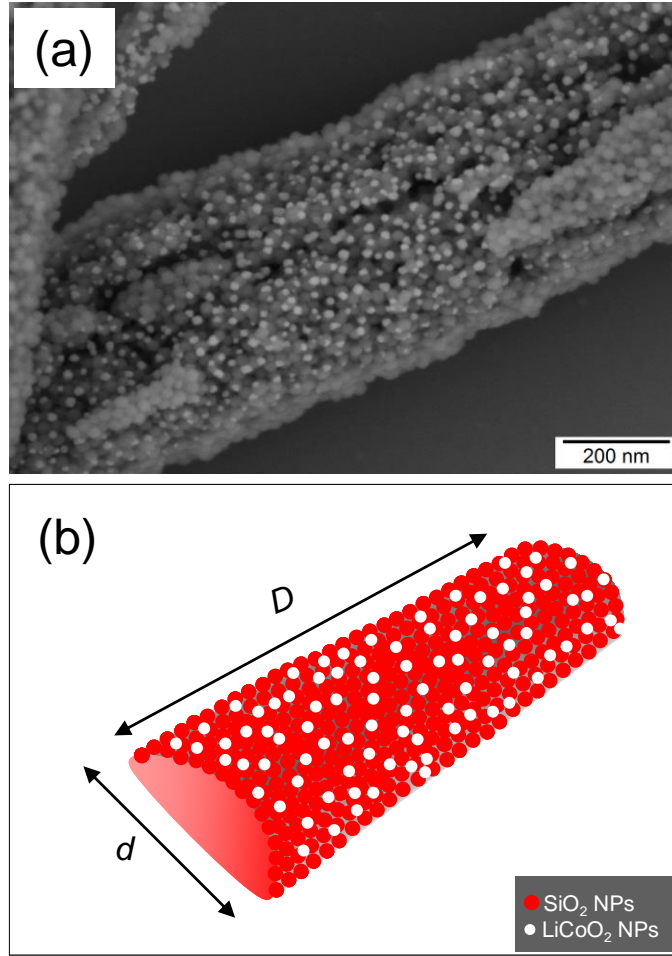
Figure 7.6. (a) SEM micrograph of a LiCoO$_2$/SiO$_2$ fiber obtained by calcination at 600
ºC and (b) schematic representation of the simple geometrical model used to
calculate percent volume of LiCoO$_2$/SiO$_2$ nanoparticles

$V_{MO[exp]}$ and $V_{MO[th]}$, were calculated from statistical measurements of particles sizes in
SEM images using equations 7.1 and 7.2:

$$V_{MO[exp]}\% = \frac{N \cdot V_{P(MO)}}{A \cdot D_{SiO_2}} \times 100 \qquad (7.1)$$

$$V_{MO[th]}\% = \frac{V_{MO}}{V_{MO} + V_{SiO_2}} \times 100 \qquad (7.2)$$

N represents the number of LiCoO$_2$ particles on the surface of a half cylinder
(A), D_{SiO2} the radius of the SiO$_2$ nanoparticles, and V_p is the volume of one spherical
LiCoO$_2$ particle. The experimental volume percent was found to be 5.0%, which was

above the theoretical value of 4.4%. Note that $V_{MO[exp]}$ represents the volume of LiCoO$_2$ that was observed by SEM, that is, located on the surface of the fibers. Therefore, the small difference between $V_{MO[exp]}$ and $V_{MO[th]}$ suggests that the LiCoO$_2$ nanoparticles are preferably situated at the fibers surface. Based on Figure 7.6a, we estimated that 18% of the total amount LiCoO$_2$ nanoparticles were present on the surface of the fibers. The fact that the surface is enriched with the metal oxide is particularly remarkable, because the metal oxide is the functional component, whereas silica plays the role of a structural framework. Such nanocomposites have potential applications as cathodes of lithium-ion batteries, functional membranes for filtration, and supported catalysts.
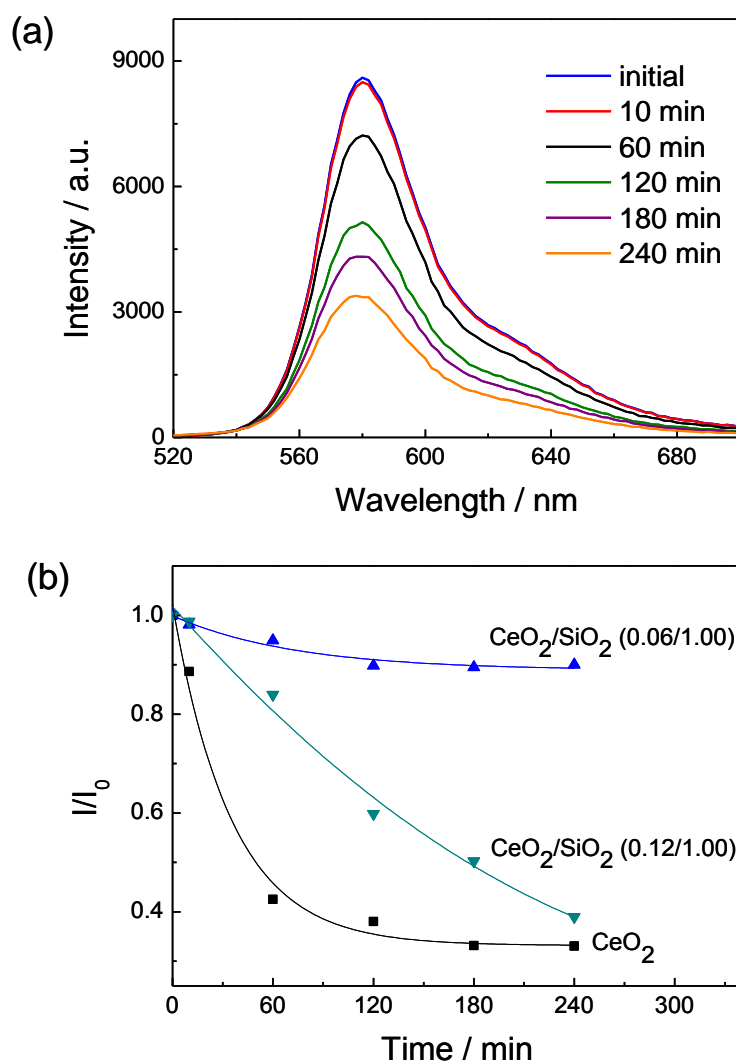
Figure 7.7. (a) PL emission spectra of rhodamine B solutions in the presence of CeO$_2$/SiO$_2$ (0.12/1.00) fibers at different time intervals, and (b) effect of different fiber catalysts on the photocatalytic degradation of rhodamine B

As a representative example, the photocatalytic activity of the CeO_2/SiO_2 fibers for the degradation of rhodamine B was investigated and compared with the SiO_2 fibers and the brittle CeO_2 fibers. The evolution of the reaction was monitored by recording the photoluminescence (PL) emission spectra of the samples at different times (Figure 7.7) The maximum at 580 nm decreased exponentially with respect to the irradiation time (Figure 7b). As expected, the decay of fluorescence intensity at time t over initial intensity (I/I_0) is slower for silica-supported fibers than for the neat fibers. The absolute performance of the fibers for the degradation of the dye, which is proportional to $P(\%)=100-(I/I_0)$, was found to increase from $P = 10\%$ (CeO_2/SiO_2:0.06/1.00) to $P = 61\%$ (CeO_2/SiO_2:0.12/1.00) when the concentration of ceria in the fibers was increased. Although P was found to be higher for the neat CeO_2 fibers (66%), the performance related to the amount of ceria in the fibers P_w are much higher for the CeO_2/SiO_2:0.12/1.00 (60% per mg CeO_2) than for the neat CeO_2 fibers (33% per mg). This comparatively higher activity is explained by the fact that CeO_2 was well-distributed along the fibers surface, being therefore accessible for the molecules to be degraded. This result is important because the efficient use of metal oxide allows the reduction of the production costs, taking into account that SiO_2 is rather inexpensive and largely available as resource.

7.5. Conclusion

The simultaneous electrospinning of ceria and lithium cobalt oxide precursors and silica nanoparticles allows the fabrication of hierarchically structured composite nanofibers. The metal oxide was found to nucleate predominantly at the surface of the fibers during the calcination process, forming nanoparticles that were mainly present among larger silica nanoparticles on the surface of even larger fibers. This hierarchical structural organization enhanced the available surface area of the catalytically active metal oxide component and improved accordingly the efficiency of the system for catalysis, as shown by the successful degradation of a fluorescent dye by ceria fibers. Moreover, the presence of silica nanoparticles as structural framework for the fibers improved both thermal and mechanical stability of the nanocomposites. The conjugation of the latter features with the functionality provided by the metal oxide and the

versatility of the electrospinning technique make our method extendable to a large variety of supported metal oxides.

CHAPTER 8

EVALUATION AND CONCLUDING REMARKS

Electrospinning provides a simple and versatile method for generating ultrathin fibers from a rich variety of materials that include polymers, composites, and ceramics. Since electrospun fibers have high specific surface area, high porosity, and small pore size, the unique fibers have been proposed for wide range of applications. This thesis has illuminated the production and characterization of functional fibrous materials for potential applications; particularly we have thematized the concept of filtration by electrospun fibers.

The removal of undesirable ions by the nanofiber sorbent was demonstrated through three model analyte-sorbent systems. Firstly, chitosan with inherent amino groups were used in fabrication of electrospun nanofibrous membranes. The adsorption efficiency of this chitosan nanofibrous scaffold was checked with a mixture of Cu (II), Fe (III), Ag(I) and Cd (II) ions at pH = 6. The sorption characteristics for chitosan flakes and the as-spun nanofibers were compared and higher extent of sorption was observed for the nanofibers as a result of the increased surface area (more than 20-fold). In addition, it was found that the selective sorption percentage of Cu(II) reached 99 %, depending on the ionic size and charge density.

The functionality of the nanofibrous membrane was further controlled through suitable surface modification to use as a filter. For example, chitosan nanofibrous membrane was decorated with nanozerovalent iron (nZVI) particles for sequestration of inorganic arsenic species at neutral pH values. Some experimental evidence suggested that the arsenic ions seem to be fixed to oxide and oxyhydroxide groups at the outer shells of nZVI surfaces. While As(V) retains its oxidation state upon fixation by nZVI, As(III) undergoes oxidation to As(V). Furthermore, chitosan seems to contribute to arsenite and arsenate complexation mainly via its hydroxyl groups. Yet another surface modification was applied to poly(acrylonitrile) fibers by transforming nitrile groups in the chains to amidoxime groups. The surface functionalized PAN fiber network was used found to be promising in sorption of U(VI) ions by column method. The post-functionalization remarkably enhanced U(VI) sorption capacity of PAN fibers. The

extent of U(VI) sorption on the fibers was found to depend on the pH of the medium and the initial concentration of the salt. The optimum pH for U(VI) sorption by amidoximated-PAN fibers was found to be 4.0, at which UO_2^{2+} ion is the main species. The adsorbed amount of U(VI) ions increased with an increase in initial U(VI) concentration.

We concluded that electrospun nanofibrous mats are promising candidates for filtration, and they possess the additional ability to sequestration of toxic metal ions through sorption. These smart materials have interconnected pore structure, high porosity, and high surface area-to-volume ratio characteristics. The combination of high surface area and tunable surface functionality of the nanofibrous mat can remarkably enhance the sorption capability of target analytes, comparable to that of commercial sorbents.

Not only polymeric but also porous ceramic fibers were fabricated by electrospinning of metal oxide precursors and polymer solutions. ZnO-based fibers synthesized and used to analyze the water vapor adsorption and desorption kinetics by Quartz Crystal Microbalance (QCM) technique. The resistance of the fiber sensor decreases by about four orders of magnitude with increasing relative humidity (RH) from 10 % to 90 % RH. In addition, electrospinning technique was used as coating process for deposition of CeO_2/ZnO and ZnO based nanofibers on the electrode of QCM. Independent of the chemistry of metal oxide, the fiber mats respond to the benzene, propanol, ethanol, and dichloromethane vapors. However, ZnO fibrous mat exhibited better performance than CeO_2/ZnO fibers most probably due to the crystal structure and presence of higher oxygen vacancies. Moreover, ZnO fiber mat seemed to be particulary sensitive to the alcoholic type compounds based on Lewis acid-base pairing.

We highlighted sensing applications associated with the remarkable features of the electrospun metal oxide nanofibrous mat. The preparation method of QCM coating is versatile and can also be used to fabricate several active nanofibrous materials. The electrospun fibers coated QCM sensors offer easy handling, high sensitivity, as well as good reproducibility. We envisaged that this strategy enables efficient design and development of other QCM coatings toward toxic gases and vapors.

A further conclusion is that the incorporation of silica nanoparticles in the composite fibers significantly improves both thermal and mechanical stability of the nanofibers. This is deduced from the study of the preparation of hierarchically

structured metal oxide nanofibers based on the simultaneous electrospinning of of ceria and lithium cobalt oxide precursors and silica nanoparticles. The metal oxide was found to nucleate mainly at the surface of the fibers in the course of calcination process, forming nanoparticles that were predominantly present among larger silica nanoparticles on the surface of even larger fibers. This hierarchical structural organization enhanced the available surface area of the catalytically active metal oxide component and improved accordingly the efficiency of the system for catalysis, as shown by the successful degradation of a fluorescent dye in the presence of the fibers.

REFERENCES

Addai-Mensah, J., J. Li, M. Zbik, and W. R. Wilmarth. 2005. Uranium sorption on solid aluminosilicate phases under caustic conditions. *Separation Science and Technology* 40 (1-3):267-279.

Agarwal, S., J. H. Wendorff, and A. Greiner. 2010. Chemistry on electrospun polymeric nanofibers: Merely routine chemistry or a real challenge? *Macromolecular Rapid Communications* 31 (15):1317-1331.

Ai, Z. H., Y. Cheng, L. Z. Zhang, and J. R. Qiu. 2008. Efficient removal of Cr(VI) from aqueous solution with Fe@Fe2O3 core-shell nanowires. *Environmental Science & Technology* 42 (18):6955-6960.

An, B., T. R. Steinwinder, and D. Y. Zhao. 2005. Selective removal of arsenate from drinking water using a polymeric ligand exchanger. *Water Research* 39 (20):4993-5004.

Antolini, E. 1997. Formation of lithium-cobalt spinel oxide (LixCo3-xO4) by solid-state reaction of a Li2CO3-Co3O4 powder mixture. *Materials Research Bulletin* 32 (1):9-14.

Antolini, E. 2004. LiCoO2: formation, structure, lithium and oxygen nonstoichiometry, electrochemical behaviour and transport properties. *Solid State Ionics* 170 (3-4):159-171.

Arnold, P. L., G. M. Jones, S. O. Odoh, G. Schreckenbach, N. Magnani, and J. B. Love. 2012. Strongly coupled binuclear uranium-oxo complexes from uranyl oxo rearrangement and reductive silylation. *Nature Chemistry* 4 (3):221-227.

Assaad, E., A. Azzouz, D. Nistor, A. V. Ursu, T. Sajin, D. N. Miron, F. Monette, P. Niquette, and R. Hausler. 2007. Metal removal through synergic coagulation-flocculation using an optimized chitosan-montmorillonite system. *Applied Clay Science* 37 (3-4):258-274.

Bailey, S. E., T. J. Olin, R. M. Bricka, and D. D. Adrian. 1999. A review of potentially low-cost sorbents for heavy metals. *Water Research* 33 (11):2469-2479.

Balasubramanian, N., T. Kojima, and C. Srinivasakannan. 2009. Arsenic removal through electrocoagulation: Kinetic and statistical modeling. *Chemical Engineering Journal* 155 (1-2):76-82.

Baleanu, M. C., R. R. Nigmatullin, S. Okur, and K. Ocakoglu. 2011. New approach for consideration of adsorption/desorption data. *Communications in Nonlinear Science and Numerical Simulation* 16 (12):4643-4648.

Bassi, R., S. O. Prasher, and B. K. Simpson. 2000. Removal of selected metal ions from aqueous solutions using chitosan flakes. *Separation Science and Technology* 35 (4):547-560.

Baumgarten, P. . 1971. Electrostatic spinning of acrylic microfibres. *Journal of Colloid and Interface Science* 36 (71-79).

Benguella, B., and H. Benaissa. 2002. Cadmium removal from aqueous solutions by chitin: kinetic and equilibrium studies. *Water Research* 36 (10):2463-2474.

Bevan, M. A. J., C. J. Proctor, J. Bakerrogers, and N. D. Warren. 1991. Exposure to carbon-monoxide, respirable suspended particulates, and volatile organic-compounds while commuting by bicycle. *Environmental Science & Technology* 25 (4):788-791.

Bhatia, S. C., and N. Ravi. 2003. A Mossbauer study of the interaction of chitosan and D-glucosamine with iron and its relevance to other metalloenzymes. *Biomacromolecules* 4 (3):723-727.

Bissen, M., and F. H. Frimmel. 2003. Arsenic - a review. Part II: Oxidation of arsenic and its removal in water treatment. *Acta Hydrochimica Et Hydrobiologica* 31 (2):97-107.

Boddu, V. M., K. Abburi, J. L. Talbott, E. D. Smith, and R. Haasch. 2008. Removal of arsenic(III) and arsenic(V) from aqueous medium using chitosan-coated biosorbent. *Water Research* 42 (3):633-642.

Bose, G.M. 1745. "Recherches sur la cause et sur la veritable theorie del'electricite " In. Wittenberg.

Boyaci, E., A. E. Eroglu, and T. Shahwan. 2010. Sorption of As(V) from waters using chitosan and chitosan-immobilized sodium silicate prior to atomic spectrometric determination. *Talanta* 80 (3):1452-1460.

Carewska, M., A. DiBartolomeo, and S. Scaccia. 1995. Thermoanalytical study of synthesis of mixed lithium cobalt oxides. *Thermochimica Acta* 269:491-506.

Chen, A. H., S. C. Liu, C. Y. Chen, and C. Y. Chen. 2008. Comparative adsorption of Cu(II), Zn(II), and Pb(II) ions in aqueous solution on the crosslinked chitosan with epichlorohydrin. *Journal of Hazardous Materials* 154 (1-3):184-191.

Chen, B. J., X. W. Sun, C. X. Xu, and B. K. Tay. 2004. Growth and characterization of zinc oxide nano/micro-fibers by thermal chemical reactions and vapor transport deposition in air. *Physica E-Low-Dimensional Systems & Nanostructures* 21 (1):103-107.

Chen, C. C., and Y. C. Chung. 2006. Arsenic removal using a biopolymer chitosan sorbent. *Journal of Environmental Science and Health Part a-Toxic/Hazardous Substances & Environmental Engineering* 41 (4):645-658.

Chen, J. P., G. Y. Chang, and J. K. Chen. 2008. Electrospun collagen/chitosan nanofibrous membrane as wound dressing. *Colloids and Surfaces a-Physicochemical and Engineering Aspects* 313:183-188.

Chen, Y. Z., Z. P. Zhang, J. Yu, and Z. X. Guo. 2009. Poly(methyl methacrylate)/silica nanocomposite Fibers by electrospinning. *Journal of Polymer Science Part B-Polymer Physics* 47 (12):1211-1218.

Cho, B. Y. 2005. Iron removal using an aerated granular filter. *Process Biochemistry* 40 (10):3314-3320.

Choi, J., D. W. Park, and S. E. Shim. 2012. Electrospun PEDOT:PSS/carbon nanotubes/PVP nanofibers as chemiresistors for aromatic volatile organic compounds. *Synthetic Metals* 162 (17-18):1513-1518.

Choi, S. S., S. G. Lee, S. S. Im, S. H. Kim, and Y. L. Joo. 2003. Silica nanofibers from electrospinning/sol-gel process. *Journal of Materials Science Letters* 22 (12):891-893.

Choi, S. W., J. Y. Park, and S. S. Kim. 2009. Synthesis of SnO2-ZnO core-shell nanofibers via a novel two-step process and their gas sensing properties. *Nanotechnology* 20 (46).

Choong, T. S. Y., T. G. Chuah, Y. Robiah, F. L. G. Koay, and I. Azni. 2007. Arsenic toxicity, health hazards and removal techniques from water: an overview. *Desalination* 217 (1-3):139-166.

Chutia, P., S. Kato, T. Kojima, and S. Satokawa. 2009. Adsorption of As(V) on surfactant-modified natural zeolites. *Journal of Hazardous Materials* 162 (1):204-211.

Cloupeau, M., and B. Prunetfoch. 1989. Electrostatic Spraying of Liquids in Cone-Jet Mode *Journal of Electrostatics* 22 (2):135-159.

Comarmond, M. J., T. E. Payne, J. J. Harrison, S. Thiruvoth, H. K. Wong, R. D. Aughterson, G. R. Lumpkin, K. Muller, and H. Foerstendorf. 2011. Uranium Sorption on Various Forms of Titanium Dioxide - Influence of Surface Area, Surface Charge, and Impurities. *Environmental Science & Technology* 45 (13):5536-5542.

Cooley, J. F. 1902. Apparatus for electrically dispersing fluids.

Cooley, J. F. 1903. Electrical Method of Dispersing Fluids

Crespy, D., K. Friedemann, and A. M. Popa. 2012. Colloid-Electrospinning: Fabrication of Multicompartment Nanofibers by the Electrospinning of Organic or/and Inorganic Dispersions and Emulsions. *Macromolecular Rapid Communications* 33 (23):1978-1995.

Crini, G. 2005. Recent developments in polysaccharide-based materials used as adsorbents in wastewater treatment. *Progress in Polymer Science* 30 (1):38-70.

Cumbal, L., and A. K. Sengupta. 2005. Arsenic removal using polymer-supported hydrated iron(III) oxide nanoparticles: Role of Donnan membrane effect. *Environmental Science & Technology* 39 (17):6508-6515.

Dai, Y. Q., W. Y. Liu, E. Formo, Y. M. Sun, and Y. N. Xia. 2011. Ceramic nanofibers fabricated by electrospinning and their applications in catalysis, environmental science, and energy technology. *Polymers for Advanced Technologies* 22 (3):326-338.

Dambies, L., E. Guibal, and A. Roze. 2000. Arsenic(V) sorption on molybdate-impregnated chitosan beads. *Colloids and Surfaces a-Physicochemical and Engineering Aspects* 170 (1):19-31.

Daus, B., R. Wennrich, and H. Weiss. 2004. Sorption materials for arsenic removal from water: A comparative study. *Water Research* 38 (12):2948-2954.

DeMarco, M. J., A. K. Sengupta, and J. E. Greenleaf. 2003. Arsenic removal using a polymeric/inorganic hybrid sorbent. *Water Research* 37 (1):164-176.

Demir, M. M., P. Castignolles, U. Akbey, and G. Wegner. 2007. In-situ bulk polymerization of dilute Particle/MMA dispersions. *Macromolecules* 40 (12):4190-4198.

Demir, M. M., M. A. Gulgun, Y. Z. Menceloglu, B. Erman, S. S. Abramchuk, E. E. Makhaeva, A. R. Khokhlov, V. G. Matveeva, and M. G. Sulman. 2004. Palladium nanoparticles by electrospinning from poly(acrylonitrile-co-acrylic acid)-PdCl2 solutions. Relations between preparation conditions, particle size, and catalytic activity. *Macromolecules* 37 (5):1787-1792.

Demir, M. M., K. Koynov, U. Akbey, C. Bubeck, I. Park, I. Lieberwirth, and G. Wegner. 2007. Optical properties of composites of PMMA and surface-modified zincite nanoparticles. *Macromolecules* 40 (4):1089-1100.

Demir, M. M., G. Ugur, M. A. Gulgun, and Y. Z. Menceloglu. 2008. Glycidyl-methacrylate-based electrospun mats and catalytic silver nanoparticles. *Macromolecular Chemistry and Physics* 209 (5):508-515.

Demir, M. M., I. Yilgor, E. Yilgor, and B. Erman. 2002. Electrospinning of polyurethane fibers. *Polymer* 43 (11):3303-3309.

Demir, R., S. Okur, M. Seker, and M. Zor. 2011. Humidity Sensing Properties of CdS Nanoparticles Synthesized by Chemical Bath Deposition Method. *Industrial & Engineering Chemistry Research* 50 (9):5606-5610.

Desai, K., K. Kit, J. J. Li, P. M. Davidson, S. Zivanovic, and H. Meyer. 2009. Nanofibrous chitosan non-wovens for filtration applications. *Polymer* 50 (15):3661-3669.

Desai, K., K. Kit, J. Li, and S. Zivanovic. 2008. Morphological and surface properties of electrospun chitosan nanofibers. *Biomacromolecules* 9 (3):1000-1006.

Deschamps, E., V. S. T. Ciminelli, and W. H. Holl. 2005. Removal of As(III) and As(V) from water using a natural Fe and Mn enriched sample. *Water Research* 39 (20):5212-5220.

Ding, B., H. Kim, C. Kim, M. Khil, and S. Park. 2003. Morphology and crystalline phase study of electrospun TiO2-SiO2 nanofibres. *Nanotechnology* 14 (5):532-537.

Ding, B., M. R. Wang, X. F. Wang, J. Y. Yu, and G. Sun. 2010. Electrospun nanomaterials for ultrasensitive sensors. *Materials Today* 13 (11):16-27.

Ding, B., M. R. Wang, J. Y. Yu, and G. Sun. 2009. Gas sensors based on electrospun nanofibers. *Sensors* 9 (3):1609-1624.

Donat, R., K. Esen, H. Cetisli, and S. Aytas. 2009. Adsorption of uranium(VI) onto Ulva sp.-sepiolite composite. *Journal of Radioanalytical and Nuclear Chemistry* 279 (1):253-261.

Dong, H., E. Fey, A. Gandelman, and W. E. Jones. 2006. Synthesis and assembly of metal nanoparticles on electrospun poly(4-vinylpyridine) fibers and poly(4-vinylpyridine) composite fibers. *Chemistry of Materials* 18 (8):2008-2011.

Doshi, J., and D. H. Reneker. 1995. Electrospinning Process and applications of electrospun fibers *Journal of Electrostatics* 35 (2-3):151-160.

Dousova, B., V. Machovic, D. Kolousek, F. Kovanda, and V. Dornicak. 2003. Sorption of As(V) species from aqueous systems. *Water Air and Soil Pollution* 149 (1-4):251-267.

Drexler, K. E. 1986. "Engines of Creation: The Coming Era of Nanotechnology." In. New York: Anchor Books.

Elostua, C., U. Bariain, J. R. Matias, F. J. Arregui, A. Luquin, and M. Laguna. 2006. Volatile alcoholic compounds fibre optic nanosensor. *Sensors and Actuators B-Chemical* 115 (1):444-449.

EPA. 2000. Chemical Precipitation. edited by U.S. Environmental Protection Agency. Washington, DC.

Erol, A., S. Okur, B. Comba, O. Mermer, and M. C. Arikan. 2010. Humidity sensing properties of ZnO nanoparticles synthesized by sol-gel process. *Sensors and Actuators B-Chemical* 145 (1):174-180.

Fan, H. T., X. J. Xu, X. K. Ma, and T. Zhang. 2011. Preparation of LaFeO3 nanofibers by electrospinning for gas sensors with fast response and recovery. *Nanotechnology* 22 (11).

Fang, D. F., C. Chang, B. S. Hsiao, and B. Chu. 2006. "Development of multiple-jet electrospinning technology." In *Polymeric Nanofibers*, edited by D. H. Reneker and H. Fong, 91-+.

Fang, X., and D. H. Reneker. 1997. DNA fibers by electrospinning. *Journal of Macromolecular Science-Physics* B36 (2):169-173.

Feynmann, R.P. 1959. There's Plenty of Room at the Bottom. http://www.zyvex.com/nanotech/feynman.html.

Fierro, J. L. G. 2006. "Metal Oxides: Chemistry and Applications." In. Boca Raton, FL: Taylor and Francis.

Formhals, A. 1934. Process and Apparatus for Preparing Artificial Threads.

Frey, M. W., A. J. Baeumner, D. Li, and P. Kakad. 2009. Electrospun nanofiber-based biosensor assemblies.

Fridrikh, S. V., J. H. Yu, M. P. Brenner, and G. C. Rutledge. 2003. Controlling the fiber diameter during electrospinning. *Physical Review Letters* 90 (14).

Friedemann, K., T. Corrales, M. Kappl, K. Landfester, and D. Crespy. 2012. Facile and Large-Scale Fabrication of Anisometric Particles from Fibers Synthesized by Colloid-Electrospinning. *Small* 8 (1):144-153.

Gamage, A., and F. Shahidi. 2007. Use of chitosan for the removal of metal ion contaminants and proteins from water. *Food Chemistry* 104 (3):989-996.

Geng, B., Z. H. Jin, T. L. Li, and X. H. Qi. 2009. Preparation of chitosan-stabilized Fe-0 nanoparticles for removal of hexavalent chromium in water. *Science of the Total Environment* 407 (18):4994-5000.

Ghurye, G. L., D. A. Clifford, and A. R. Tripp. 1999. Combined arsenic and nitrate removal by ion exchange. *Journal American Water Works Association* 91 (10):85-96.

Gibson, P., H. Schreuder-Gibson, and D. Rivin. 2001. Transport properties of porous membranes based on electrospun nanofibers. *Colloids and Surfaces a-Physicochemical and Engineering Aspects* 187:469-481.

Gihring, T. M., G. K. Druschel, R. B. McCleskey, R. J. Hamers, and J. F. Banfield. 2001. Rapid arsenite oxidation by Thermus aquaticus and Thermus thermophilus: Field and laboratory investigations. *Environmental Science & Technology* 35 (19):3857-3862.

Gimenez, J., M. Martinez, J. de Pablo, M. Rovira, and L. Duro. 2007. Arsenic sorption onto natural hematite, magnetite, and goethite. *Journal of Hazardous Materials* 141 (3):575-580.

Graham, K., M. Gogins, and H. Schreuder-Gibson. 2004. Incorporation of electrospun nanofibers into functional structures. 13:21-27.

Grate, J. W. 2000. Acoustic wave microsensor arrays for vapor sensing. *Chemical Reviews* 100 (7):2627-2647.

Greathouse, J. A., and R. T. Cygan. 2006. Water structure and aqueous uranyl(VI) adsorption equilibria onto external surfaces of beidellite, montmorillonite, and pyrophyllite: Results from molecular simulations. *Environmental Science & Technology* 40 (12):3865-3871.

Greiner, A., and J. H. Wendorff. 2007. Electrospinning: A fascinating method for the preparation of ultrathin fibres. *Angewandte Chemie-International Edition* 46 (30):5670-5703.

Grosvenor, A. P., B. A. Kobe, M. C. Biesinger, and N. S. McIntyre. 2004. Investigation of multiplet splitting of Fe 2p XPS spectra and bonding in iron compounds. *Surface and Interface Analysis* 36 (12):1564-1574.

Guibal, E. 2004. Interactions of metal ions with chitosan-based sorbents: a review. *Separation and Purification Technology* 38 (1):43-74.

Guibal, E., A. Larkin, T. Vincent, and J. M. Tobin. 1999. Chitosan sorbents for platinum sorption from dilute solutions. *Industrial & Engineering Chemistry Research* 38 (10):4011-4022.

Gupta, A., M. Yunus, and N. Sankararamakrishnan. 2012. Zerovalent iron encapsulated chitosan nanospheres - A novel adsorbent for the removal of total inorganic Arsenic from aqueous systems. *Chemosphere* 86 (2):150-155.

Hagiwaba, K., O. Oji-Machi, and K. Ku. 1929. Process for manufacturing artificial silk and other filaments by applying electric current.

Haider, S., and S. Y. Park. 2009. Preparation of the electrospun chitosan nanofibers and their applications to the adsorption of Cu(II) and Pb(II) ions from an aqueous solution. *Journal of Membrane Science* 328 (1-2):90-96.

Hajra, M. G., K. Mehta, and G. G. Chase. 2003. Effects of humidity, temperature, and nanofibers on drop coalescence in glass fiber media. *Separation and Purification Technology* 30 (1):79-88.

Hakim, M., Y. Y. Broza, O. Barash, N. Peled, M. Phillips, A. Amann, and H. Haick. 2012. Volatile organic compounds of lung cancer and possible biochemical pathways. *Chemical Reviews* 112 (11):5949-5966.

Hansen, N. S., T. E. Ferguson, J. E. Panels, A. H. A. Park, and Y. L. Joo. 2011. Inorganic nanofibers with tailored placement of nanocatalysts for hydrogen production via alkaline hydrolysis of glucose. *Nanotechnology* 22 (32).

Hess, S., M. M. Demir, V. Yakutkin, S. Baluschev, and G. Wegner. 2009. Investigation of oxygen permeation through composites of PMMA and surface-modified ZnO nanoparticles. *Macromolecular Rapid Communications* 30 (4-5):394-401.

Hirotsu, T., S. Katoh, K. Sugasaka, M. Seno, and T. Itagaki. 1986. Adsorption equilibrium of uranium from aqueous UO2(CO3)3 4- Solutions on a polymer

bearing amidoxime groups. *Journal of the Chemical Society-Dalton Transactions* (9):1983-1986.

Hohman, M. M., M. Shin, G. Rutledge, and M. P. Brenner. 2001a. Electrospinning and electrically forced jets. I. Stability theory. *Physics of Fluids* 13 (8):2201-2220.

Hohman, M. M., M. Shin, G. Rutledge, and M. P. Brenner. 2001b. Electrospinning and electrically forced jets. II. Applications. *Physics of Fluids* 13 (8):2221-2236.

Horzum, N., E. Boyaci, A. E. Eroglu, T. Shahwan, and M. M. Demir. 2010. Sorption efficiency of chitosan nanofibers toward metal ions at low concentrations. *Biomacromolecules* 11 (12):3301-3308.

Horzum, N., R. Munoz-Espi, G. Glasser, M. M. Demir, K. Landfester, and D. Crespy. 2012. Hierarchically structured metal oxide/silica nanofibers by colloid electrospinning. *Acs Applied Materials & Interfaces* 4 (11):6338-6345.

Horzum, N., D. Tascioglu, S. Okur, and M. M. Demir. 2011. Humidity sensing properties of ZnO-based fibers by electrospinning. *Talanta* 85 (2):1105-1111.

Hu, J. Y., X. Y. Liu, Y. Q. Fan, S. H. Xie, Y. Pei, M. H. Qiao, K. N. Fan, X. X. Zhang, and B. N. Zong. 2013. Physically mixed ZnO and skeletal NiMo for one-pot reforming-hydrogenolysis of glycerol to 1,2-propanediol. *Chinese Journal of Catalysis* 34 (5):1020-1026.

Hu, X. L., J. M. Gong, L. Z. Zhang, and J. C. Yu. 2008. Continuous size tuning of monodisperse ZnO colloidal nanocrystal clusters by a microwave-polyol process and their application for humidity sensing. *Advanced Materials* 20 (24):4845-+.

Huang, Z. M., Y. Z. Zhang, M. Kotaki, and S. Ramakrishna. 2003. A review on polymer nanofibers by electrospinning and their applications in nanocomposites. *Composites Science and Technology* 63 (15):2223-2253.

Hudson, E. A., L. J. Terminello, B. E. Viani, M. Denecke, T. Reich, P. G. Allen, J. J. Bucher, D. K. Shuh, and N. M. Edelstein. 1999. The structure of U6+ sorption complexes on vermiculite and hydrobiotite. *Clays and Clay Minerals* 47 (4):439-457.

Iqbal, J., H. J. Kim, J. S. Yang, K. Baek, and J. W. Yang. 2007. Removal of arsenic from groundwater by micellar-enhanced ultrafiltration (MEUF). *Chemosphere* 66 (5):970-976.

Islam, Akms, Z. Ismail, M. N. Ahmad, B. Saad, A. R. Othman, A. Y. M. Shakaff, A. Daud, and Z. Ishak. 2005. Transient parameters of a coated quartz-crystal microbalance sensor for the detection of volatile organic compounds (VOCs). *Sensors and Actuators B-Chemical* 109 (2):238-243.

Jagadish, Chennupati, and Stephen J. Pearton. 2006. *Zinc oxide bulk, thin films and nanostructures: Processing, properties, and applications*. Hong Kong: Elsevier.

Jia, H. F., G. Y. Zhu, B. Vugrinovich, W. Kataphinan, D. H. Reneker, and P. Wang. 2002. Enzyme-carrying polymeric nanofibers prepared via electrospinning for use as unique biocatalysts. *Biotechnology Progress* 18 (5):1027-1032.

Jiang, H. L., D. F. Fang, B. S. Hsiao, B. Chu, and W. L. Chen. 2004. Optimization and characterization of dextran membranes prepared by electrospinning. *Biomacromolecules* 5 (2):326-333.

Jones, A. P. 1999. Indoor air quality and health. *Atmospheric Environment* 33 (28):4535-4564.

Juang, R. S., and R. C. Shiau. 2000. Metal removal from aqueous solutions using chitosan-enhanced membrane filtration. *Journal of Membrane Science* 165 (2):159-167.

Justi, K. C., V. T. Favere, M. C. M. Laranjeira, A. Neves, and R. A. Peralta. 2005. Kinetics and equilibrium adsorption of Cu(II), Cd(II), and Ni(II) ions by chitosan functionalized with 2 -bis-(pyridylmethyl)aminomethyl -4-methyl-6-formylphenol. *Journal of Colloid and Interface Science* 291 (2):369-374.

Kalin, M., W. N. Wheeler, and G. Meinrath. 2005. The removal of uranium from mining waste water using algal/microbial biomass. *Journal of Environmental Radioactivity* 78 (2):151-177.

Kameoka, J., R. Orth, Y. N. Yang, D. Czaplewski, R. Mathers, G. W. Coates, and H. G. Craighead. 2003. A scanning tip electrospinning source for deposition of oriented nanofibres. *Nanotechnology* 14 (10):1124-1129.

Kampa, M., and E. Castanas. 2008. Human health effects of air pollution. *Environmental Pollution* 151 (2):362-367.

Kanehata, M., B. Ding, and S. Shiratori. 2007. Nanoporous ultra-high specific surface inorganic fibres. *Nanotechnology* 18 (31).

Kanel, S. R., J. M. Greneche, and H. Choi. 2006. Arsenic(V) removal kom groundwater using nano scale zero-valent iron as a colloidal reactive barrier material. *Environmental Science & Technology* 40 (6):2045-2050.

Kanel, S. R., B. Manning, L. Charlet, and H. Choi. 2005. Removal of arsenic(III) from groundwater by nanoscale zero-valent iron. *Environmental Science & Technology* 39 (5):1291-1298.

Kanjwal, M. A., N. A. M. Barakat, F. A. Sheikh, S. J. Park, and H. Y. Kim. 2010. Photocatalytic activity of ZnO-TiO2 hierarchical nanostructure prepared by combined electrospinning and hydrothermal techniques. *Macromolecular Research* 18 (3):233-240.

Kanjwal, M. A., F. A. Sheikh, N. A. M. Barakat, I. S. Chronakis, and H. Y. Kim. 2011. Co3O4-ZnO hierarchical nanostructures by electrospinning and hydrothermal methods. *Applied Surface Science* 257 (18):7975-7981.

Kanjwal, M. A., F. A. Sheikh, N. A. M. Barakat, X. Q. Li, H. Y. Kim, and I. S. Chronakis. 2012. Zinc oxide's hierarchical nanostructure and its photocatalytic properties. *Applied Surface Science* 258 (8):3695-3702.

Karabelli, D., S. Unal, T. Shahwan, and A. E. Eroglu. 2011. Preparation and characterization of alumina-supported iron nanoparticles and its application for the removal of aqueous Cu2+ ions. *Chemical Engineering Journal* 168 (2):979-984.

Karatapanis, A. E., D. E. Petrakis, and C. D. Stalikas. 2012. A layered magnetic iron/iron oxide nanoscavenger for the analytical enrichment of ng-L-1 concentration levels of heavy metals from water. *Analytica Chimica Acta* 726:22-27.

Kasaai, M. R. 2007. Calculation of Mark-Houwink-Sakurada (MHS) equation viscometric constants for chitosan in any solvent-temperature system using experimental reported viscometric constants data. *Carbohydrate Polymers* 68 (3):477-488.

Kasaai, M. R., J. Arul, and C. Charlet. 2000. Intrinsic viscosity-molecular weight relationship for chitosan. *Journal of Polymer Science Part B-Polymer Physics* 38 (19):2591-2598.

Khani, M. H. 2011. Statistical analysis and isotherm study of uranium biosorption by Padina sp algae biomass. *Environmental Science and Pollution Research* 18 (5):790-799.

Kilincarslan, A., and S. Akyil. 2005. Uranium adsorption characteristic and thermodynamic behavior of clinoptilolite zeolite. *Journal of Radioanalytical and Nuclear Chemistry* 264 (3):541-548.

Kim, I. D., and A. Rothschild. 2011. Nanostructured metal oxide gas sensors prepared by electrospinning. *Polymers for Advanced Technologies* 22 (3):318-325.

Kim, J., and M. M. Benjamin. 2004. Modeling a novel ion exchange process for arsenic and nitrate removal. *Water Research* 38 (8):2053-2062.

Kim, J. S., and D. H. Reneker. 1999. Polybenzimidazole nanofiber produced by electrospinning. *Polymer Engineering and Science* 39 (5):849-854.

Kim, Y. J., C. H. Ahn, and M. O. Choi. 2010. Effect of thermal treatment on the characteristics of electrospun PVDF-silica composite nanofibrous membrane. *European Polymer Journal* 46 (10):1957-1965.

Klimov, E., V. Raman, R. Venkatesh, W. Heckmann, and R. Stark. 2010. Designing Nanofibers via Electrospinning from Aqueous Colloidal Dispersions: Effect of Cross-Linking and Template Polymer. *Macromolecules* 43 (14):6152-6155.

Klug, H. P., and L. E. Alexander. 1974a. "X-Ray Diffraction procedures for polycrystalline and amorphous materials." In. New York: John Wiley.

Klug, Harold P. , and Leroy E. Alexander. 1974b. *X-Ray Diffraction procedures: For polycrystalline and amorphous materials*. 2nd Edition ed. New York: John Wiley.

Koikov, L. N., N. V. Alexeeva, E. A. Lisitza, E. S. Krichevsky, N. B. Grigoryev, A. V. Danilov, I. S. Severina, N. V. Pyatakova, and V. G. Granik. 1998. Oximes, amidoximes and hydroxamic acids as nitric oxide donors. *Mendeleev Communications* (4):165-168.

Kowal-Fouchard, A., R. Drot, E. Simoni, and J. J. Ehrhardt. 2004. Use of spectroscopic techniques for uranium (VI)/montmorillonite interaction modeling. *Environmental Science & Technology* 38 (5):1399-1407.

Lacasa, E., P. Canizares, C. Saez, F. J. Fernandez, and M. A. Rodrigo. 2011. Removal of arsenic by iron and aluminium electrochemically assisted coagulation. *Separation and Purification Technology* 79 (1):15-19.

Lakshmanan, D., D. A. Clifford, and G. Samanta. 2010. Comparative study of arsenic removal by iron using electrocoagulation and chemical coagulation. *Water Research* 44 (19):5641-5652.

Lakshmanan, D., D. Clifford, and G. Samanta. 2008. Arsenic removal by coagulation - With aluminum, iron, titanium, and zirconium. *Journal American Water Works Association* 100 (2):76-+.

Lange, Norbert Adolph. 1979. "Lange's Handbook of Chemistry." In, ed John A. Dean: McGraw-Hill Inc.,US.

Langford, J. I., and A. J. C. Wilson. 1978. Scherrer after 60 years - Survey and some new results in determination of crystallite size. *Journal of Applied Crystallography* 11 (APR):102-113.

Larrondo, L., and R. S. J. Manley. 1981. Electrostatic fiber spinning from polymer melts. 1. Experimental observations on fiber formation and properties. *Journal of Polymer Science Part B-Polymer Physics* 19 (6):909-920.

Lee, D., M. Yoo, H. Seo, Y. Tak, W. G. Kim, K. Yong, S. W. Rhee, and S. Jeon. 2009. Enhanced mass sensitivity of ZnO nanorod-grown quartz crystal microbalances. *Sensors and Actuators B-Chemical* 135 (2):444-448.

Lee, M. Y., K. J. Hong, T. Kajiuchi, and J. W. Yang. 2005. Synthesis of chitosan-based polymeric surfactants and their adsorption properties for heavy metals and fatty acids. *International Journal of Biological Macromolecules* 36 (3):152-158.

Lee, S. T., F. L. Mi, Y. J. Shen, and S. S. Shyu. 2001. Equilibrium and kinetic studies of copper(II) ion uptake by chitosan-tripolyphosphate chelating resin. *Polymer* 42 (5):1879-1892.

Lenoble, V., O. Bouras, V. Deluchat, B. Serpaud, and J. C. Bollinger. 2002. Arsenic adsorption onto pillared clays and iron oxides. *Journal of Colloid and Interface Science* 255 (1):52-58.

Leupin, O. X., and S. J. Hug. 2005. Oxidation and removal of arsenic (III) from aerated groundwater by filtration through sand and zero-valent iron. *Water Research* 39 (9):1729-1740.

Li, D., Y. L. Wang, and Y. N. Xia. 2003. Electrospinning of polymeric and ceramic nanofibers as uniaxially aligned arrays. *Nano Letters* 3 (8):1167-1171.

Li, D., and Y. N. Xia. 2004. Electrospinning of nanofibers: Reinventing the wheel? *Advanced Materials* 16 (14):1151-1170.

Li, J. S., X. Y. Miao, Y. X. Hao, J. Y. Zhao, X. Y. Sun, and L. J. Wang. 2008. Synthesis, amino-functionalization of mesoporous silica and its adsorption of Cr(VI). *Journal of Colloid and Interface Science* 318 (2):309-314.

Li, L., W. H. Meyer, G. Wegner, and M. Wohlfahrt-Mehrens. 2005. Synthesis of submicrometer-sized electrochemically active lithium cobalt oxide via a polymer precursor. *Advanced Materials* 17 (8):984-+.

Li, N., and R. B. Bai. 2005. Copper adsorption on chitosan-cellulose hydrogel beads: behaviors and mechanisms. *Separation and Purification Technology* 42 (3):237-247.

Li, N., R. B. Bai, and C. K. Liu. 2005. Enhanced and selective adsorption of mercury ions on chitosan beads grafted with polyacrylamide via surface-initiated atom transfer radical polymerization. *Langmuir* 21 (25):11780-11787.

Li, X. Q., D. W. Elliott, and W. X. Zhang. 2006. Zero-valent iron nanoparticles for abatement of environmental pollutants: Materials and engineering aspects. *Critical Reviews in Solid State and Materials Sciences* 31 (4):111-122.

Lim, J. M., J. H. Moon, G. R. Yi, C. J. Heo, and S. M. Yang. 2006. Fabrication of one-dimensional colloidal assemblies from electrospun nanofibers. *Langmuir* 22 (8):3445-3449.

Lin, W. P., Y. Lu, and H. M. Zeng. 1993. Studies of the preparation, structure, and properties of an acrylic chelating fiber containing amidoxime groups. *Journal of Applied Polymer Science* 47 (1):45-52.

Lindner, J. P., C. Roben, A. Studer, M. Stasiak, R. Ronge, A. Greiner, and H. J. Wendorff. 2009. Reusable catalysts based on dendrimers trapped in poly(p-xylylene) nanotubes. *Angewandte Chemie-International Edition* 48 (47):8874-8877.

Liu, B., and H. C. Zeng. 2003. Hydrothermal synthesis of ZnO nanorods in the diameter regime of 50 nm. *Journal of the American Chemical Society* 125 (15):4430-4431.

Liu, F. T., S. F. Gao, S. K. Pei, S. C. Tseng, and C. H. J. Liu. 2009. ZnO nanorod gas sensor for NO2 detection. *Journal of the Taiwan Institute of Chemical Engineers* 40 (5):528-532.

Liu, H. Q., J. Kameoka, D. A. Czaplewski, and H. G. Craighead. 2004. Polymeric nanowire chemical sensor. *Nano Letters* 4 (4):671-675.

Liu, L., Y. Zhang, G. G. Wang, S. C. Li, L. Y. Wang, Y. Han, X. X. Jiang, and A. G. Wei. 2011. High toluene sensing properties of NiO-SnO2 composite nanofiber sensors operating at 330 degrees C. *Sensors and Actuators B-Chemical* 160 (1):448-454.

Liu, T. Y., L. Zhao, and Z. L. Wang. 2012. Removal of hexavalent chromium from wastewater by Fe-0-nanoparticles-chitosan composite beads: characterization, kinetics and thermodynamics. *Water Science and Technology* 66 (5):1044-1051.

Lu, G. Q., I. Lieberwirth, and G. Wegner. 2006. A general polymer-based process to prepare mixed metal oxides: The case of Zn1-xMgxO nanoparticles. *Journal of the American Chemical Society* 128 (48):15445-15450.

Ma, H., Y. P. Huang, M. W. Shen, R. Guo, X. Y. Cao, and X. Y. Shi. 2012. Enhanced dechlorination of trichloroethylene using electrospun polymer nanofibrous mats immobilized with iron/palladium bimetallic nanoparticles. *Journal of Hazardous Materials* 211:349-356.

Ma, H. Y., C. Burger, B. S. Hsiao, and B. Chu. 2012. Nanofibrous microfiltration membrane based on cellulose nanowhiskers. *Biomacromolecules* 13 (1):180-186.

Ma, H. Y., B. S. Hsiao, and B. Chu. 2013. Electrospun nanofibrous membrane for heavy metal ion adsorption. *Current Organic Chemistry* 17 (13):1361-1370.

Ma, Z. J., H. J. Ji, Y. Teng, G. P. Dong, J. J. Zhou, D. Z. Tan, and J. R. Qiu. 2011. Engineering and optimization of nano- and mesoporous silica fibers using sol-gel and electrospinning techniques for sorption of heavy metal ions. *Journal of Colloid and Interface Science* 358 (2):547-553.

Mahmoud, W. E., and F. A. Al-Agel. 2011. A novel strategy to synthesize cobalt hydroxide and Co3O4 nanowires. *Journal of Physics and Chemistry of Solids* 72 (7):904-907.

Mandal, B. K., and K. T. Suzuki. 2002. Arsenic round the world: a review. *Talanta* 58 (1):201-235.

Mayer, E., and J. Warren. 1998. Evaluating filtration media: A comparison of polymeric membranes and nonwovens. *Filtration & Separation* 35 (10):912-914.

McKinley, J. P., J. M. Zachara, S. C. Smith, and G. D. Turner. 1995. The influence of uranyl hydrolysis and multiple site-binding reactions on adsorption of U(VI) to montmorillonite. *Clays and Clay Minerals* 43 (5):586-598.

Milot, C., J. McBrien, S. Allen, and E. Guibal. 1998. Influence of physicochemical and structural characteristics of chitosan flakes on molybdate sorption. *Journal of Applied Polymer Science* 68 (4):571-580.

Miretzky, P., and A. F. Cirelli. 2009. Hg(II) removal from water by chitosan and chitosan derivatives: A review. *Journal of Hazardous Materials* 167 (1-3):10-23.

Mizuno, Y., E. Hosono, T. Saito, M. Okubo, D. Nishio-Hamane, K. Oh-ishi, T. Kudo, and H. S. Zhou. 2012. Electrospinning synthesis of wire-structured LiCoO2 for electrode materials of high-power Li-Ion batteries. *Journal of Physical Chemistry C* 116 (19):10774-10780.

Mohan, D., and C. U. Pittman. 2007. Arsenic removal from water/wastewater using adsorbents - A critical review. *Journal of Hazardous Materials* 142 (1-2):1-53.

Moharram, M. A., and M. G. Khafagi. 2006. Thermal behavior of poly(acrylic acid)-poly(vinyl pyrrolidone) and poly(acrylic acid)-metal-poly(vinyl pyrrolidone) complexes. *Journal of Applied Polymer Science* 102 (4):4049-4057.

Mokkelbost, T., I. Kaus, T. Grande, and M. A. Einarsrud. 2004. Combustion synthesis and characterization of nanocrystalline CeO2-based powders. *Chemistry of Materials* 16 (25):5489-5494.

Mondal, B. C., and A. K. Das. 2003. Use of 6-mercapto purinylazo resin in chromium speciation. *Bulletin of the Chemical Society of Japan* 76 (1):111-114.

Monteiro, O. A. C., and C. Airoldi. 1999. Some thermodynamic data on copper-chitin and copper-chitosan biopolymer interactions. *Journal of Colloid and Interface Science* 212 (2):212-219.

Mori, M., H. Nishimura, Y. Itagaki, Y. Sadaoka, and E. Traversa. 2009. Detection of sub-ppm level of VOCs based on a Pt/YSZ/Pt potentiometric oxygen sensor with reference air. *Sensors and Actuators B-Chemical* 143 (1):56-61.

Morton, W. J. 1902. Method of Dispersing Fluids.

Mun, G. A., Z. S. Nurkeeva, G. S. Irmukhametova, and O. Guven. 2007. Synthesis, characterization and adsorption study of the uranyl ions by hydrogels based on polyethylene glycol and methacrylic acid copolymers. *Nuclear Instruments & Methods in Physics Research Section B-Beam Interactions with Materials and Atoms* 265 (1):379-384.

Nagao, M. 1971a. *The Journal of Physical Chemistry* 76:3822–3828.

Nagao, M. 1971b. Physisorption of water on zinc oxide surface *Journal of Physical Chemistry* 75 (25):3822-&.

Nakajima, A., T. Horikoshi, and T. Sakaguchi. 1982. Studies on the accumulation of heavy-metal elements in biological-systems .21. Recovery of uranium by

immobilized microorganisms. *European Journal of Applied Microbiology and Biotechnology* 16 (2-3):88-91.

Nam, Y. S., W. H. Park, D. Ihm, and S. M. Hudson. 2010. Effect of the degree of deacetylation on the thermal decomposition of chitin and chitosan nanofibers. *Carbohydrate Polymers* 80 (1):291-295.

Ng, J. C. Y., W. H. Cheung, and G. McKay. 2002. Equilibrium studies of the sorption of Cu(II) ions onto chitosan. *Journal of Colloid and Interface Science* 255 (1):64-74.

Ngah, W. S. W., S. Ab Ghani, and A. Kamari. 2005. Adsorption behaviour of Fe(II) and Fe(III) ions in aqueous solution on chitosan and cross-linked chitosan beads. *Bioresource Technology* 96 (4):443-450.

Ngah, W. S. W., C. S. Endud, and R. Mayanar. 2002. Removal of copper(II) ions from aqueous solution onto chitosan and cross-linked chitosan beads. *Reactive & Functional Polymers* 50 (2):181-190.

Ngah, W. S. W., and S. Fatinathan. 2008. Adsorption of Cu(II) ions in aqueous solution using chitosan beads, chitosan-GLA beads and chitosan-alginate beads. *Chemical Engineering Journal* 143 (1-3):62-72.

Ngah, W. S. W., and S. Fatinathan. 2010. Pb(II) biosorption using chitosan and chitosan derivatives beads: Equilibrium, ion exchange and mechanism studies. *Journal of Environmental Sciences-China* 22 (3):338-346.

Nilchi, A., A. A. Babalou, R. Raflee, and H. S. Kalal. 2008. Adsorption properties of amidoxime resins for separation of metal ions from aqueous systems. *Reactive & Functional Polymers* 68 (12):1665-1670.

Ning, R. Y. 2002. Arsenic removal by reverse osmosis. *Desalination* 143 (3):237-241.

Ohkawa, K., D. I. Cha, H. Kim, A. Nishida, and H. Yamamoto. 2004. Electrospinning of chitosan. *Macromolecular Rapid Communications* 25 (18):1600-1605.

Okamoto, H., S. Nishida, H. Todo, Y. Sakakura, K. Iida, and K. Danjo. 2003. Pulmonary gene delivery by chitosan-pDNA complex powder prepared by a supercritical carbon dioxide process. *Journal of Pharmaceutical Sciences* 92 (2):371-380.

Oku, M., and K. Hirokawa. 1979. XPS observation of Fe1-XO at temperatures between 25 and 800-degrees-C. *Journal of Applied Physics* 50 (10):6303-6308.

Okur, S., C. Ceylan, and E. Culcular. 2012. Humidity adsorption kinetics of a trypsin gel film. *Journal of Colloid and Interface Science* 368:470-473.

Okur, S., M. Kus, F. Ozel, V. Aybek, and M. Yilmaz. 2010. Humidity adsorption kinetics of calix 4 arene derivatives measured using QCM technique. *Talanta* 81 (1-2):248-251.

Okur, S., N. Uzar, N. Tekguzel, A. Erol, and M. C. Arikan. 2012. Synthesis and humidity sensing analysis of ZnS nanowires. *Physica E-Low-Dimensional Systems & Nanostructures* 44 (6):1103-1107.

Ozgur, U., Y. I. Alivov, C. Liu, A. Teke, M. A. Reshchikov, S. Dogan, V. Avrutin, S. J. Cho, and H. Morkoc. 2005. A comprehensive review of ZnO materials and devices. *Journal of Applied Physics* 98 (4).

Pagana, A. E., S. D. Sklari, E. S. Kikkinides, and V. T. Zaspalis. 2008. Microporous ceramic membrane technology for the removal of arsenic and chromium ions from contaminated water. *Microporous and Mesoporous Materials* 110 (1):150-156.

Panels, J. E., and Y. L. Joo. 2006. Incorporation of vanadium oxide in silica nanofiber mats via electrospinning and sol-gel synthesis. *Journal of Nanomaterials*.

Park, J. A., J. Moon, S. J. Lee, S. H. Kim, H. Y. Chu, and T. Zyung. 2010. SnO2-ZnO hybrid nanofibers-based highly sensitive nitrogen dioxides sensor. *Sensors and Actuators B-Chemical* 145 (1):592-595.

Park, J. A., J. Moon, S. J. Lee, S. C. Lim, and T. Zyung. 2009. Fabrication and characterization of ZnO nanofibers by electrospinning. *Current Applied Physics* 9:S210-S212.

Paulsen, F. G., S. S. Shojaie, and W. B. Krantz. 1994. Effect of evaporation step on macrovoid formation in wet-cast polymeric membranes *Journal of Membrane Science* 91 (3):265-282.

Pekel, N., and O. Guven. 2003. Separation of uranyl ions with amidoximated poly(acrylonitrile/N-vinylimidazole) complexing sorbents. *Colloids and Surfaces a-Physicochemical and Engineering Aspects* 212 (2-3):155-161.

Pekel, N., N. Sahiner, and O. Guven. 2000. Development of new chelating hydrogels based on N-vinyl imidazole and acrylonitrile. *Radiation Physics and Chemistry* 59 (5-6):485-491.

Pekel, N., N. Sahiner, and O. Guven. 2004. Thermodynamics of adsorption of uranyl ions onto amidoximated poly(acrylonitrile)/poly(N-vinyl 2-pyrrolidone) interpenetrating polymer networks. *Journal of Polymer Science Part B-Polymer Physics* 42 (6):986-993.

Pelino, M. , C. Cantalini, and M. Faccio. 1994. Principles and applications of ceramic Humidity Sensors. *Active and Passive Electronic Components* 16 (2):69-87.

Piron, E., and A. Domard. 1998. Interaction between chitosan and uranyl ions. Part 2. Mechanism of interaction. *International Journal of Biological Macromolecules* 22 (1):33-40.

Planas, M. R. 2002. Ph.D. Thesis, Universitat Polytecnica de Catalunya.

Pontoni, L., and M. Fabbricino. 2012. Use of chitosan and chitosan-derivatives to remove arsenic from aqueous solutions-a mini review. *Carbohydrate Research* 356:86-92.

Pradip, C. Maltesh, P. Somasundaran, R. A. Kulkarni, and S. Gundiah. 1991. Polymer-polymer complexation in dilute aqueous-solutions - poly(acrylic acid)-poly(ethylene oxide) and poly(acrylic acid)-poly(vinylpyrrolidone). *Langmuir* 7 (10):2108-2111.

Puziy, A. M., O. I. Poddubnaya, V. N. Zaitsev, and O. P. Konoplitska. 2004. Modeling of heavy metal ion binding by phosphoric acid activated carbon. *Applied Surface Science* 221 (1-4):421-429.

Qi, Q., T. Zhang, S. J. Wang, and X. J. Zheng. 2009. Humidity sensing properties of KCl-doped ZnO nanofibers with super-rapid response and recovery. *Sensors and Actuators B-Chemical* 137 (2):649-655.

Qi, Q., T. Zhang, Q. J. Yu, R. Wang, Y. Zeng, L. Liu, and H. B. Yang. 2008. Properties of humidity sensing ZnO nanorods-base sensor fabricated by screen-printing. *Sensors and Actuators B-Chemical* 133 (2):638-643.

Qiu, S. J., L. X. Sun, H. L. Chu, Y. J. Zou, F. Xu, and N. Matsuda. 2009. Study of adsorption behaviors of meso-tetrakis (4-N-Methylpyridyl) porphine p-Toluenesulfonate at indium-tin-oxide electrode/solution interface by in-situ internal reflection spectroscopy and cyclic voltammetry. *Thin Solid Films* 517 (9):2905-2911.

Qiu, Y. F., and S. H. Yang. 2007. ZnO nanotetrapods: Controlled vapor-phase synthesis and application for humidity sensing. *Advanced Functional Materials* 17 (8):1345-1352.

Ramaseshan, R., S. Sundarrajan, R. Jose, and S. Ramakrishna. 2007. Nanostructured ceramics by electrospinning. *Journal of Applied Physics* 102 (11).

Ramos, M. A. V., W. Yan, X. Q. Li, B. E. Koel, and W. X. Zhang. 2009. Simultaneous oxidation and reduction of arsenic by zero-valent iron nanoparticles: Understanding the significance of the core-shell structure. *Journal of Physical Chemistry C* 113 (33):14591-14594.

Public domain software to be downloaded from National Institute of Health ImageJ 1.44p.

Rayleigh, L. . 1882. On the equilibrium of liquid conducting masses charged with electricity. *Philosophical Magazine*, 184-186.

Ren, T., Y. Si, J. M. Yang, B. Ding, X. X. Yang, F. Hong, and J. Y. Yu. 2012. Polyacrylonitrile/polybenzoxazine-based Fe3O4@carbon nanofibers: hierarchical porous structure and magnetic adsorption property. *Journal of Materials Chemistry* 22 (31):15919-15927.

Reneker, D. H., and I. Chun. 1996. Nanometre diameter fibres of polymer, produced by electrospinning. *Nanotechnology* 7 (3):216-223.

Reneker, D. H., and A. L. Yarin. 2008. Electrospinning jets and polymer nanofibers. *Polymer* 49 (10):2387-2425.

Reneker, D. H., A. L. Yarin, H. Fong, and S. Koombhongse. 2000. Bending instability of electrically charged liquid jets of polymer solutions in electrospinning. *Journal of Applied Physics* 87 (9):4531-4547.

Rhazi, M., J. Desbrieres, A. Tolaimate, M. Rinaudo, P. Vottero, A. Alagui, and M. El Meray. 2002. Influence of the nature of the metal ions on the complexation with chitosan. Application to the treatment of liquid waste. *European Polymer Journal* 38 (8):1523-1530.

Ricco, A. J., R. M. Crooks, and G. C. Osbourn. 1998. Surface acoustic wave chemical sensor arrays: New chemically sensitive interfaces combined with novel cluster analysis to detect volatile organic compounds and mixtures. *Accounts of Chemical Research* 31 (5):289-296.

Rivas, B. L., and A. Maureira. 2008. Water-soluble polyelectrolytes contaning sulfonic acid groups with metal ion binding ability by using the liquid phase polymer based retention technique. *Macromolecular Symposia* 270:143-152.

Rodrigues, A. E. . 1986. Ion Exchange Science and Technology. Leiden, Netherlands: Martinus Nijhoff Publishers.

Rossen, E., J. N. Reimers, and J. R. Dahn. 1993. Synthesis and electrochemistry of spinel Lt-LiCOO2. *Solid State Ionics* 62 (1-2):53-60.

Sadeghi, S., H. Azhdari, H. Arabi, and A. Z. Moghaddam. 2012. Surface modified magnetic Fe3O4 nanoparticles as a selective sorbent for solid phase extraction of uranyl ions from water samples. *Journal of Hazardous Materials* 215:208-216.

Saeed, K., S. Haider, T. J. Oh, and S. Y. Park. 2008. Preparation of amidoxime-modified polyacrylonitrile (PAN-oxime) nanofibers and their applications to metal ions adsorption. *Journal of Membrane Science* 322 (2):400-405.

Saha, J. C., A. K. Dikshit, M. Bandyopadhyay, and K. C. Saha. 1999. A review of arsenic poisoning and its effects on human health. *Critical Reviews in Environmental Science and Technology* 29 (3):281-313.

Sahiner, N., N. Pekel, and O. Guven. 1999. Radiation synthesis, characterization and amidoximation of N-vinyl-2-pyrrolidone/acrylonitrile interpenetrating polymer networks. *Reactive & Functional Polymers* 39 (2):139-146.

Sakai, S., T. Yamaguchi, R. A. Putra, R. Watanabe, M. Kawabe, M. Taya, and K. Kawakami. 2012. Controlling apatite microparticles formation by calcining electrospun sol-gel derived ultrafine silica fibers. *Journal of Sol-Gel Science and Technology* 61 (2):374-380.

Sang, Y. M., F. S. Li, Q. B. Gu, C. Z. Liang, and J. Q. Chen. 2008. Heavy metal-contaminated groundwater treatment by a novel nanofiber membrane. *Desalination* 223 (1-3):349-360.

Sangsanoh, P., and P. Supaphol. 2006. Stability improvement of electrospun chitosan nanofibrous membranes in neutral or weak basic aqueous solutions. *Biomacromolecules* 7 (10):2710-2714.

Sauerbrey, G. 1959. Verwendung von Schwingquarzen zur Wägung dünner Schichten und zur Mikrowägung. *Zeitschrift für Physik A Hadrons and Nuclei* 155:206-222.

Schaub, R., P. Thostrup, N. Lopez, E. Laegsgaard, I. Stensgaard, J. K. Norskov, and F. Besenbacher. 2001. Oxygen vacancies as active sites for water dissociation on rutile TiO2(110). *Physical Review Letters* 87 (26).

Schiffman, J. D., L. A. Stulga, and C. L. Schauer. 2009. Chitin and chitosan: Transformations due to the electrospinning process. *Polymer Engineering and Science* 49 (10):1918-1928.

Schreuder-Gibson, H., P. Gibson, K. Senecal, M. Sennett, J. Walker, W. Yeomans, D. Ziegler, and P. P. Tsai. 2002. Protective textile materials based on electrospun nanofibers. *Journal of Advanced Materials* 34 (3):44-55.

Seferis, J.C. . 1999. *Polymer Handbook*. New York: Wiley & Sons.

Seol, Y. J., K. H. Kim, Y. M. Kang, I. A. Kim, and S. H. Rhee. 2009. Bioactivity, pre-osteoblastic cell responses, and osteoconductivity evaluations of the electrospun non-woven SiO(2)-CaO gel fabrics. *Journal of Biomedical Materials Research Part B-Applied Biomaterials* 90B (2):679-687.

Shahwan, T., H. N. Erten, and S. Unugur. 2006. A characterization study of some aspects of the adsorption of aqueous Co2+ ions on a natural bentonite clay. *Journal of Colloid and Interface Science* 300 (2):447-452.

Shahwan, T., C. Uzum, A. E. Eroglu, and I. Lieberwirth. 2010. Synthesis and characterization of bentonite/iron nanoparticles and their application as adsorbent of cobalt ions. *Applied Clay Science* 47 (3-4):257-262.

Shao, C. L., H. Kim, J. Gong, and D. Lee. 2002. A novel method for making silica nanofibres by using electrospun fibres of polyvinylalcohol/silica composite as precursor. *Nanotechnology* 13 (5):635-637.

Sharma, Y. C., V. Srivastava, V. K. Singh, S. N. Kaul, and C. H. Weng. 2009. Nano-adsorbents for the removal of metallic pollutants from water and wastewater. *Environmental Technology* 30 (6):583-609.

Shi, L. N., X. Zhang, and Z. L. Chen. 2011. Removal of Chromium (VI) from wastewater using bentonite-supported nanoscale zero-valent iron. *Water Research* 45 (2):886-892.

Shi, W., W. S. Lu, and L. Jiang. 2009. The fabrication of photosensitive self-assembly Au nanoparticles embedded in silica nanofibers by electrospinning. *Journal of Colloid and Interface Science* 340 (2):291-297.

Shih, M. C. 2005. An overview of arsenic removal by pressure-driven membrane processes. *Desalination* 172 (1):85-97.

Shih, S. J., K. B. Borisenko, L. J. Liu, and C. Y. Chen. 2010. Multiporous ceria nanoparticles prepared by spray pyrolysis. *Journal of Nanoparticle Research* 12 (5):1553-1559.

Si, P., J. Mortensen, A. Kornolov, J. Denborg, and P. J. Moller. 2007. Polymer coated quartz crystal microbalance sensors for detection of volatile organic compounds in gas mixtures. *Analytica Chimica Acta* 597 (2):223-230.

Si, Y., T. Ren, B. Ding, J. Y. Yu, and G. Sun. 2012. Synthesis of mesoporous magnetic Fe3O4@carbon nanofibers utilizing in situ polymerized polybenzoxazine for water purification. *Journal of Materials Chemistry* 22 (11):4619-4622.

Sigmund, W., J. Yuh, H. Park, V. Maneeratana, G. Pyrgiotakis, A. Daga, J. Taylor, and J. C. Nino. 2006. Processing and structure relationships in electrospinning of ceramic fiber systems. *Journal of the American Ceramic Society* 89 (2):395-407.

Simm, W. , K. Gosling, R. Bonart, and B. von Falkai. 1972.

Smorada, R. 1996. Nonwoven fabrics, spunbonded. In *Kirk-Othmer Encyclopedia of Chemical Technology*. New York: Wiley.

Song, S., A. Lopez-Valdivieso, D. J. Hernandez-Campos, C. Peng, M. G. Monroy-Fernandez, and I. Razo-Soto. 2006. Arsenic removal from high-arsenic water by enhanced coagulation with ferric ions and coarse calcite. *Water Research* 40 (2):364-372.

Srinivasan, G., and D. H. Reneker. 1995. Structure and Morphology of Small-Diameter Electrospun Aramid Fibers *Polymer International* 36 (2):195-201.

Stasiak, M., A. Studer, A. Greiner, and J. H. Wendorff. 2007. Polymer fibers as carriers for homogeneous catalysts. *Chemistry-a European Journal* 13 (21):6150-6156.

Strunk, J., W. C. Vining, and A. T. Bell. 2011. Synthesis of different CeO2 structures on mesoporous silica and characterization of their reduction properties. *Journal of Physical Chemistry C* 115 (10):4114-4126.

Sun, L. H., R. P. Liu, S. J. Xia, Y. L. Yang, and G. B. Li. 2009. Enhanced As(III) removal with permanganate oxidation, ferric chloride precipitation and sand filtration as pretreatment of ultrafiltration. *Desalination* 243 (1-3):122-131.

Sun, L., L. D. Zhang, C. H. Liang, Z. G. Yuan, Y. Zhang, W. Xu, J. X. Zhang, and Y. Z. Chen. 2011. Chitosan modified Fe-0 nanowires in porous anodic alumina and their application for the removal of hexavalent chromium from water. *Journal of Materials Chemistry* 21 (16):5877-5880.

Sureshkumar, M. K., D. Das, M. B. Mallia, and P. C. Gupta. 2010. Adsorption of uranium from aqueous solution using chitosan-tripolyphosphate (CTPP) beads. *Journal of Hazardous Materials* 184 (1-3):65-72.

Sylwester, E. R., E. A. Hudson, and P. G. Allen. 2000. The structure of uranium (VI) sorption complexes on silica, alumina, and montmorillonite. *Geochimica Et Cosmochimica Acta* 64 (14):2431-2438.

Taghizadeh, S. M., and G. Davari. 2006. Preparation, characterization, and swelling behavior of N-acetylated and deacetylated chitosans. *Carbohydrate Polymers* 64 (1):9-15.

Takeda, T., K. Saito, K. Uezu, S. Furusaki, T. Sugo, and J. Okamoto. 1991. Adsorption and elution in hollow-fiber-packed bed for recovery of uranium from seawater. *Industrial & Engineering Chemistry Research* 30 (1):185-190.

Tang, C. J., H. L. Zhang, C. Z. Sun, J. C. Li, L. Qi, Y. J. Quan, F. Gao, and L. Dong. 2011. An efficient strategy for highly loaded, well dispersed and thermally stable metal oxide catalysts. *Catalysis Communications* 12 (12):1075-1078.

Taniguchi, N. 1974. On the basic concept of 'Nano-Technology'. Paper read at The International Conference on Production Engineering, at Tokyo.

Tao, S. Y., G. T. Li, and J. X. Yin. 2007. Fluorescent nanofibrous membranes for trace detection of TNT vapor. *Journal of Materials Chemistry* 17 (26):2730-2736.

Taylor, G. 1969. Electrically driven jets. *Proceedings of the Royal Society A: Mathematical, Physical and Engineering Sciences* 313 (1515):453-475.

Taylor, G. . 1966. The force exerted by an electric field on a long cylindrical conductor. *Proceedings of the Royal Society A: Mathematical, Physical and Engineering Sciences* 291 (1425):145-158.

Theron, S. A., E. Zussman, and A. L. Yarin. 2004. Experimental investigation of the governing parameters in the electrospinning of polymer solutions. *Polymer* 45 (6):2017-2030.

Tolaimate, A., J. Desbrieres, M. Rhazi, A. Alagui, M. Vincendon, and P. Vottero. 2000. On the influence of deacetylation process on the physicochemical characteristics of chitosan from squid chitin. *Polymer* 41 (7):2463-2469.

Tucker, N., J. J. Stanger, M. P. Staiger, H. Razzaq, and K. Hofman. 2012. The history of the science and technology of electrospinning from 1600 to 1995. *Journal of Engineered Fibers and Fabrics*:63-73.

Twu, Y. K., H. I. Huang, S. Y. Chang, and S. L. Wang. 2003. Preparation and sorption activity of chitosan/cellulose blend beads. *Carbohydrate Polymers* 54 (4):425-430.

Uzum, C., T. Shahwan, A. E. Eroglu, K. R. Hallam, T. B. Scott, and I. Lieberwirth. 2009. Synthesis and characterization of kaolinite-supported zero-valent iron nanoparticles and their application for the removal of aqueous $Cu2+$ and $Co2+$ ions. *Applied Clay Science* 43 (2):172-181.

Valcarcel, V., A. Souto, and F. Guitian. 1998. Development of single-crystal alpha-Al2O3 fibers by vapor-liquid-solid deposition (VLS) from aluminum and powdered silica. *Advanced Materials* 10 (2):138-+.

Valentin, R., K. Molvinger, F. Quignard, and D. Brunel. 2003. Supercritical CO2 dried chitosan: an efficient intrinsic heterogeneous catalyst in fine chemistry. *New Journal of Chemistry* 27 (12):1690-1692.

Varma, A. J., S. V. Deshpande, and J. F. Kennedy. 2004. Metal complexation by chitosan and its derivatives: a review. *Carbohydrate Polymers* 55 (1):77-93.

Venugopal, J., and S. Ramakrishna. 2005. Applications of polymer nanofibers in biomedicine and biotechnology. *Applied Biochemistry and Biotechnology* 125 (3):147-157.

Vieira, R. S., and M. M. Beppu. 2006a. Dynamic and static adsorption and desorption of Hg(II) ions on chitosan membranes and spheres. *Water Research* 40 (8):1726-1734.

Vieira, R. S., and M. M. Beppu. 2006b. Interaction of natural and crosslinked chitosan membranes with Hg(II) ions. *Colloids and Surfaces a-Physicochemical and Engineering Aspects* 279 (1-3):196-207.

Wagner, C.D., W.M. Riggs, L.E. Davis, J.F. Moulder, and G.E. Muilenberg. 1979. Handbook of X-ray photoelectron spectroscopy, Physical Electronics Division. Eden Prairie, Minnesota: Perkin-Elmer Corporation.

Wang, R., Y. Liu, B. Li, B. S. Hsiao, and B. Chu. 2012. Electrospun nanofibrous membranes for high flux microfiltration. *Journal of Membrane Science* 392:167-174.

Wang, W., H. M. Huang, Z. Y. Li, H. N. Zhang, Y. Wang, W. Zheng, and C. Wang. 2008. Zinc oxide nanofiber gas sensors via electrospinning. *Journal of the American Ceramic Society* 91 (11):3817-3819.

Wang, W., Z. Y. Li, L. Liu, H. N. Zhang, W. Zheng, Y. Wang, H. M. Huang, Z. J. Wang, and C. Wang. 2009. Humidity sensor based on LiCl-doped ZnO electrospun nanofibers. *Sensors and Actuators B-Chemical* 141 (2):404-409.

Wang, X. F., F. H. Cui, J. Y. Lin, B. Ding, J. Y. Yu, and S. S. Al-Deyab. 2012. Functionalized nanoporous TiO2 fibers on quartz crystal microbalance platform for formaldehyde sensor. *Sensors and Actuators B-Chemical* 171:658-665.

Wang, X. F., B. Ding, M. Sun, J. Y. Yu, and G. Sun. 2010. Nanofibrous polyethyleneimine membranes as sensitive coatings for quartz crystal microbalance-based formaldehyde sensors. *Sensors and Actuators B-Chemical* 144 (1):11-17.

Wang, X. F., B. Ding, J. Y. Yu, Y. Si, S. B. Yang, and G. Sun. 2011. Electro-netting: Fabrication of two-dimensional nano-nets for highly sensitive trimethylamine sensing. *Nanoscale* 3 (3):911-915.

Wang, X. H., J. Zhang, and Z. Q. Zhu. 2006. Ammonia sensing characteristics of ZnO nanowires studied by quartz crystal microbalance. *Applied Surface Science* 252 (6):2404-2411.

Wang, X. Y., C. Drew, S. H. Lee, K. J. Senecal, J. Kumar, and L. A. Sarnuelson. 2002. Electrospun nanofibrous membranes for highly sensitive optical sensors. *Nano Letters* 2 (11):1273-1275.

Wang, Z. G., L. S. Wan, Z. M. Liu, X. J. Huang, and Z. K. Xu. 2009. Enzyme immobilization on electrospun polymer nanofibers: An overview. *Journal of Molecular Catalysis B-Enzymatic* 56 (4):189-195.

Wesselt, C., R. Ostermann, R. Dersch, and B. M. Smarsly. 2011. Formation of inorganic nanofibers from preformed TiO2 nanoparticles via electrospinning. *Journal of Physical Chemistry C* 115 (2):362-372.

WHO. 2004. Guidelines for drinking-water quality, Recommendations. Geneva: World Health Organization.

Wickramasinghe, S. R., B. B. Han, J. Zimbron, Z. Shen, and M. N. Karim. 2004. Arsenic removal by coagulation and filtration: comparison of groundwaters from the United States and Bangladesh. *Desalination* 169 (3):231-244.

Wong, K. K., C. K. Lee, K. S. Low, and M. J. Haron. 2003. Removal of Cu and Pb by tartaric acid modified rice husk from aqueous solutions. *Chemosphere* 50 (1):23-28.

Wrasidlo, W. J. , and K. J. Mysels. 1984. The structure and some properties of graded highly asymmetrical porous membranes. *Journal of Parenteral Science and Technology* 38:24-31.

Wu, F. C., R. L. Tseng, and R. S. Juang. 2010. A review and experimental verification of using chitosan and its derivatives as adsorbents for selected heavy metals. *Journal of Environmental Management* 91 (4):798-806.

Wu, H., D. Lin, R. Zhang, and W. Pan. 2008. ZnO nanofiber field-effect transistor assembled by electrospinning. *Journal of the American Ceramic Society* 91 (2):656-659.

Wu, J. J., and S. C. Liu. 2002. Low-temperature growth of well-aligned ZnO nanorods by chemical vapor deposition. *Advanced Materials* 14 (3):215-+.

Xia, H. J., Y. Wang, F. H. Kong, S. R. Wang, B. L. Zhu, X. Z. Guo, J. Zhang, Y. M. Wang, and S. H. Wu. 2008. Au-doped WO3-based sensor for NO2 detection at low operating temperature. *Sensors and Actuators B-Chemical* 134 (1):133-139.

Xiao, S. L., H. Ma, M. W. Shen, S. Y. Wang, Q. G. Huang, and X. Y. Shi. 2011. Excellent copper(II) removal using zero-valent iron nanoparticle-immobilized hybrid electrospun polymer nanofibrous mats. *Colloids and Surfaces a-Physicochemical and Engineering Aspects* 381 (1-3):48-54.

Xiao, S. L., M. W. Shen, R. Guo, Q. G. Huang, S. Y. Wang, and X. Y. Shi. 2010. Fabrication of multiwalled carbon nanotube-reinforced electrospun polymer nanofibers containing zero-valent iron nanoparticles for environmental applications. *Journal of Materials Chemistry* 20 (27):5700-5708.

Xiao, S. L., M. W. Shen, R. Guo, S. Y. Wang, and X. Y. Shi. 2009. Immobilization of zerovalent iron nanoparticles into electrospun polymer nanofibers: Synthesis, characterization, and potential environmental applications. *Journal of Physical Chemistry C* 113 (42):18062-18068.

Xu, X. M., C. Z. Li, K. M. Pei, K. Zhao, Z. B. K. Zhao, and H. Y. Li. 2008. Ionic liquids used as QCM coating materials for the detection of alcohols. *Sensors and Actuators B-Chemical* 134 (1):258-265.

Yadav, B. C., R. Srivastava, C. D. Dwivedi, and P. Pramanik. 2008. Moisture sensor based on ZnO nanomaterial synthesized through oxalate route. *Sensors and Actuators B-Chemical* 131 (1):216-222.

Yadav, B. C., R. Srivastava, C. D. Dwivedi, and P. Pramanik. 2009. Synthesis of nano-sized ZnO using drop wise method and its performance as moisture sensor. *Sensors and Actuators a-Physical* 153 (2):137-141.

Yan, W. L., M. A. V. Ramos, B. E. Koel, and W. X. Zhang. 2010. Multi-tiered distributions of arsenic in iron nanoparticles: Observation of dual redox functionality enabled by a core-shell structure. *Chemical Communications* 46 (37):6995-6997.

Yan, W., R. Vasic, A. I. Frenkel, and B. E. Koel. 2012. Intraparticle reduction of arsenite (As(III)) by nanoscale zerovalent iron (nZVI) investigated with in situ X-ray absorption spectroscopy. *Environmental Science & Technology* 46 (13):7018-7026.

Yang, T., and R. R. Zall. 1984. Chitosan membranes for reverse-osmosis application. *Journal of Food Science* 49 (1):91-93.

Yang, X. H., C. L. Shao, H. Y. Guan, X. L. Li, and H. Gong. 2004. Preparation and characterization of ZnO nanofibers by using electrospun PVA/zinc acetate composite fiber as precursor. *Inorganic Chemistry Communications* 7 (2):176-178.

Yarin, A. L., S. Koombhongse, and D. H. Reneker. 2001. Bending instability in electrospinning of nanofibers. *Journal of Applied Physics* 89 (5):3018-3026.

Yarin, A. L., and E. Zussman. 2004a. Upward needleless electrospinning of multiple nanofibers. *Polymer* 45 (9):2977-2980.

Yarin, A. L., and E. Zussman. 2004b. Complex and smart fluids. Paper read at XXI International Congress of Theoretical and Applied Mechanics, at Warsaw, Poland.

Yoo, S., S. A. Dregia, and S. A. Akbar. 2006. Kinetic mechanism of TiO2 nanocarving via reaction with hydrogen gas. *Journal of Materials Research* 21 (7):1822-1829.

Zeleny, J. 1917. Instability of electrified liquid surfaces. *Physical Review Letters* 10 (1):1-6.

Zeman, L. J., and Zydney A.L. 1996. "Microfiltration and ultrafiltration: Principles and Applications." In. New York: Marcel Dekker, Inc.

Zhan, S. H., D. R. Chen, X. L. Jiao, and Y. Song. 2007. Mesoporous TiO2/SiO2 composite nanofibers with selective photocatalytic properties. *Chemical Communications* (20):2043-2045.

Zhang, H. N., Z. Y. Li, W. Wang, C. Wang, and L. Liu. 2010. Na+-doped zinc oxide nanofiber membrane for high speed humidity sensor. *Journal of the American Ceramic Society* 93 (1):142-146.

Zhang, X. C., Y. Z. Chen, J. Yu, and Z. X. Guo. 2011. Thermoplastic polyurethane/silica nanocomposite fibers by electrospinning. *Journal of Polymer Science Part B-Polymer Physics* 49 (23):1683-1689.

Zhang, X. J., and G. J. Qiao. 2012. High performance ethanol sensing films fabricated from ZnO and In2O3 nanofibers with a double-layer structure. *Applied Surface Science* 258 (17):6643-6647.

Zhang, Y. S., K. Yu, D. S. Jiang, Z. Q. Zhu, H. R. Geng, and L. Q. Luo. 2005. Zinc oxide nanorod and nanowire for humidity sensor. *Applied Surface Science* 242 (1-2):212-217.

Zhao, X. B., R. W. Long, Y. Chen, and Z. G. Chen. 2010. Synthesis, characterization of CeO(2)@SiO(2) nanoparticles and their oxide CMP behavior. *Microelectronic Engineering* 87 (9):1716-1720.

Zhou, L. M., J. H. Liu, and Z. R. Liu. 2009. Adsorption of platinum(IV) and palladium(II) from aqueous solution by thiourea-modified chitosan microspheres. *Journal of Hazardous Materials* 172 (1):439-446.

Zhou, Y. S., D. Z. Yang, X. M. Chen, Q. Xu, F. M. Lu, and J. Nie. 2008. Electrospun water-soluble carboxyethyl chitosan/poly(vinyl alcohol) nanofibrous membrane as potential wound dressing for skin regeneration. *Biomacromolecules* 9 (1):349-354.

Zong, X. H., K. Kim, D. F. Fang, S. F. Ran, B. S. Hsiao, and B. Chu. 2002. Structure and process relationship of electrospun bioabsorbable nanofiber membranes. *Polymer* 43 (16):4403-4412.

Zou, W. H., H. J. Bai, L. Zhao, K. Li, and R. P. Han. 2011. Characterization and properties of zeolite as adsorbent for removal of uranium(VI) from solution in fixed bed column. *Journal of Radioanalytical and Nuclear Chemistry* 288 (3):779-788.

Zou, W. H., L. Zhao, and R. P. Han. 2009. Removal of uranium (VI) by fixed bed ion-exchange column using natural zeolite coated with manganese oxide. *Chinese Journal of Chemical Engineering* 17 (4):585-593.

Zou, W. H., L. Zhao, and R. P. Han. 2011. Adsorption characteristics of uranyl ions by manganese oxide coated sand in batch mode. *Journal of Radioanalytical and Nuclear Chemistry* 288 (1):239-249.

VITA

PERSONAL INFORMATION

Surname, Name: HORZUM POLAT NESRİN
Nationality: Turkish (TC)
Date and Place of Birth: 17.01.1983, Ödemiş/İZMİR
Marital Status: Married
Phone: +90 (542) 761 67 75
E-mail: n.horzum@gmail.com

EDUCATION

Degree Institution Year of Graduation
MSc İzmir Institute of Technology 2008
BSc Pamukkale University 2004

WORK EXPERIENCE

Year Place Enrollment
2006-2013 İzmir Institute of Technology, Research Assistant
2011-2012 Max-Planck Institute for Polymer Research, Research Scholar
2003 İzmir Refik Saydam National Public Health Agency, Trainee

PUBLICATIONS

Horzum, N., Mari, M., Crespy, D., Wagner, M., Demir, M. M., Landfester, K., Muñoz-Espí, R. 2013. *In Progress.*

Horzum. N., Tascioglu, D., Özbek, C., Okur, S. Demir, M. M. 2013 *Submitted to Sensors and Actuators B: Chemical.*

Boyaci, E., Horzum, N., Cagir, A., Demir, M. M., Eroglu, A. E. 2013. *Submitted to RSC Advances.*

Demir M. M., Horzum N., Ozen B., Ozcelik S. 2013. *Accepted in The Journal of Physical Chemistry B.*

Horzum, N., Demir, M. M., Nairat, M., Shahwan, T. 2013. *RSC Advances,* 3, 7828-7837.

Horzum, N., Shahwan, T., Parlak, O., Demir, M. M. 2012. *Chemical Engineering Journal,* 213, 41-49.

Horzum, N., Muñoz-Espí, R., Glasser, G., Demir, M.M., Landfester, K., Crespy, D. 2012. *ACS Applied Materials & Interfaces* 4(11) 6338-6345.

Horzum, N., Tascioglu, D., Demir, M. M., Okur, S. 2011. *Talanta* 85(2) 1105-1111.

Horzum, N. Boyaci, E., Eroglu, A. E., Shahwan, T., Demir, M. M. 2010. *Biomacromolecules* 11(12) 3301-3308.

Divrikli, U., Horzum, N., Soylak, M., Elci, Latif. 2006. *Journal of Food Science and Technology* 41(6) 712-716.